Statistical methods to understand and visualise the complex behaviour of clouds in the climate system

Rachel W. N. Sansom

Submitted in accordance with the requirements for the degree of
Doctor of Philosophy

The University of Leeds
School of Earth and Environment

June 2023

The candidate confirms that the work submitted is their own and that appropriate credit has been given where reference has been made to the work of others.

The contents of Chapters 3 and 4 included in this thesis are both from jointly authored publications which have yet to be submitted to journal. Co-authors Ken Carslaw, Lindsay Lee, Jill Johnson and Leighton Regayre provided guidance during ensemble design, model output analysis, and the application of statistical techniques. All authors were involved in discussion of results and reviewing of the manuscripts. The candidate carried out the model simulations, analysis and drafting of the manuscripts.

An adapted version of Chapter 3 has been published as a single authored publication entitled "Demystifying the complex nature of stratocumulus clouds with machine learning" (Sansom, 2021).

Acknowledgements

I am very grateful to the EPSRC DTP for granting me the funding to complete this thesis and to NERC for granting me significant resources on ARCHER2. The technical help received from the staff at ARCHER2, JASMIN, ARC4 and CEMAC was crucial to the success of this project. I also owe a huge thanks to Chris Dearden, Adrian Lock, Adrian Hill, Steef Boing, Leif Denby and Craig Poku for walking me through all the quirks of MONC.

Thank you to my supervisor team: Ken Carslaw, Lindsay Lee, Jill Johnson and Leighton Regayre. I have hugely appreciated your patient guidance and thoughtful discussions and have learned a great deal from you. Each of you saw the different ways that I struggled with this, and I can barely express my gratitude that you stuck with me through it.

Thank you to everyone in office 10.126 for being friendly, welcoming and showing me what third year PGRs look like. Chris, Sarah, Tom, Laura and Felicity, you showed me it was possible and that PhD experiences come in all shapes and sizes. And provided long coffee breaks to ease me in.

I have to thank my enormous, amazing family for providing so much love and support throughout the last four and a bit years. Everything I have and will ever achieve is through the tools that each of you has equipped me with. And thanks for telling me I had a big head, I guess I had to prove it was useful for something.

I would have given up at many points were it not for the loyal support of friends, now scattered across the World. Lauren, you've been my rock. I am so thankful that you always believed I could do it. Sam, Georgina, Grace and Stu, thanks for letting me into St. Anne's Road and immediately providing colourful friendships. Suzie, Sarah, Will, Joe, Heather and Ruth, it has been an absolute pleasure to do this with you, see you at 5:01! Sarah S, those lockdown coffees were a true weekly highlight. Sarah B, the last months together were... a rollercoaster to say the least. I'm so glad we had each other, and the memes, to the end. Freya, you arrived in my life at the perfect time and added many beautiful moments in the hard bits. Max, I will be forever grateful for the security and all the laughter you provided me with.

A special thank you goes to my gal, Ruth. You picked me up from my worst points and gave me tool after tool to battle imposter syndrome. You were the perfect companion to have by my side and in the next bedroom through this all. Girls **got** it done.

Leam, thank you for the biggest adventure, and reminding me to have fun.

Finally, thank you to Jonathan Leach for giving me that leg up many years ago and for telling me that the cloud project "sounds pretty cool".

Here lies everything I know about clouds.
But, as Joni Mitchell said, I really don't know clouds at all.

Abstract

Uncertainty surrounding cloud responses to changes in their environments contributes majorly to uncertainty in the radiative effects of aerosol and predictions of future climates. Stratocumulus clouds exert a strong net cooling effect due to their high albedo and large horizontal extent, yet their behaviour in the climate system is particularly uncertain due to their high sensitivity to surroundings. High-resolution modelling is crucial for studying stratocumulus behaviours, which are made up of many complex interacting processes, on many scales from large-scale dynamics to the microphysical responses to aerosol. However, many studies perturb cloud-controlling factors one at a time, which makes it challenging to identify interactions with other factors and how they jointly affect cloud properties. To understand the complex behaviour of marine stratocumulus clouds, this thesis uses two statistical methods: perturbed parameter ensembles and Gaussian process emulation. Perturbed parameter ensembles perturb multiple factors simultaneously so that their joint effects can be analysed. Furthermore, these ensembles can be used as training data for Gaussian process emulation, which is used to create statistical representations of the relationships between multiple cloud-controlling factors and cloud properties of interest. The emulators are used to generate the values of cloud properties for many new combinations of factor values, which allows the joint effects of parameters to be analysed and parameter contributions to the variances in the cloud properties to be quantified.

Firstly, two properties of the free troposphere are perturbed from simulations of a homogeneous, nocturnal stratocumulus cloud to analyse cloud behaviour around the break-up threshold for cloud-top entrainment instability. Dense sampling using emulators of liquid water path and cloud fraction showed that there were non-linear interactions between the two perturbed factors and two behavioural regimes. Additionally, a method for approximating the natural variability of the cloud and accounting for it in the emulator build was demonstrated. Secondly, the stratocumulus-to-cumulus transition was simulated to study the roles of aerosol and drizzle in the context of other cloud-controlling factors. From the base simulation, one model parameter and five cloud-controlling factors were perturbed across reasonable ranges. Analysis of the perturbed parameter ensemble showed that the fastest transitions occurred in low-aerosol

environments combined with deep boundary layers, high autoconversion rates and dry temperature inversions. When the ensemble was split into high- and low-drizzle environments, the inversion strength was found to have a strong control on transition time, via entrainment, in low-drizzle environments. Thirdly, the ensemble of stratocumulus-to-cumulus transitions was used as training data for Gaussian process emulation, which allowed the joint effects of parameters in transition properties to be fully visualised and quantified. Emulation revealed that there was a low-aerosol regime, where aerosol concentration strongly controlled the transition time, but outside that regime, the transition time was largely dependent on the inversion strength. The transition time was found to be a complex process that was influenced by multiple interacting parameters, whereas the rain water path is controlled by individual parameters.

Contents

List of Figures

Nomenclature

Acronyms

BL Boundary layer

CASIM Cloud AeroSol Interacting Microphysics

CGILS CFMIP-GASS Intercomparison of LES and SCM models

CSET Cloud System Evolution in the Trades

Cu Cumulus

DYCOMS-II Second Dynamics and Chemistry of Marine Stratocumulus field study

IPCC Intergovernmental Panel on Climate Change

LEM Large-eddy model

LES Large-eddy simulation

MMR Mass mixing ratio

MONC UK Met Office/Natural Environment Research Council (NERC) Cloud model

PPE Perturbed parameter ensemble

Sc Stratocumulus

SOCRATES Suite of Radiation Transfer Codes based on Edwards and Slingo

SST Sea surface temperature

Symbols

$\Delta\theta$ Inversion jump in potential temperature or inversion strength

Δq_v Inversion jump in vapour mass mixing ratio (specific humidity)

f_c Cloud fraction

b_{aut} Autoconversion rate "b" parameter

BL N_a BL aerosol concentration

BL q_v BL vapour mass mixing ratio (specific humidity)

BL z BL depth

L or LWP Liquid water path

Chapter 1

Introduction

1.1 Clouds in the climate system

Covering approximately two thirds of the planet, primarily in convergence zones and areas of frequent storm tracks, clouds act in the radiation budget to reflect incident solar radiation (shortwave energy) and retain outgoing thermal radiation (longwave energy) (Stubenrauch et al., 2013; Boucher et al., 2014). Of the incoming 340 W m^{-2} of shortwave energy, clouds and the surrounding atmosphere reflect 75 W m^{-2}. For longwave energy, clouds approximately behave as a blackbody (a perfect absorber and emitter of radiation) because water droplets strongly absorb thermal radiation, so longwave is re-emitted to space at the temperature of the cloud's upper surfaces (Pincus and Baker, 1994). Of the 398 W m^{-2} of upwelling longwave radiating from the surface, only 28 W m^{-2} is retained by clouds, which is known as the cloud greenhouse effect. With the removal of clouds from the climate system there would be 47 W m^{-2} less shortwave and 28 W m^{-2} more longwave transmitted to space, giving a net difference due to clouds (net cloud radiative effect) of -19 W m^{-2} (Wild et al., 2019). This means that clouds have a global net cooling effect (Stephens et al., 2012).

The net cloud radiative effect varies regionally depending on location, altitude, cloud properties and the albedo of the surface below the clouds. Polar clouds exert a net warming effect for most of the year due to the high albedo of land and sea ice beneath them and the lack of shortwave radiation during the polar night (Curry, Schramm, and Ebert, 1993). Low, shallow clouds over marine environments have a net cooling effect because the ocean surface has a lower albedo and they are low in the atmosphere so longwave radiation is re-emitted from the cloud top at approximately the same temperature as the surface (Klein and Hartmann, 1993).

Human activity since the pre-industrial period has rapidly increased the concentrations of greenhouse gases in the atmosphere, preventing longwave radiation from

leaving the Earth system and causing an imbalance in the radiation budget that leads to planetary warming (Forster et al., 2021). Changes to the radiation budget at the top of the atmosphere by anthropogenic agents (e.g., the burning of fossil fuels) are quantified as "radiative forcings". Radiative forcing is defined as the change in net downward radiative flux at the tropopause after stratospheric temperatures have readjusted to radiative equilibrium, while other temperatures and state variables are held fixed at unperturbed values (Myhre et al., 2013). The total radiative forcing is the effective radiative forcing, which can be split into the immediate response and the subsequent adjustments, excluding responses to changes in temperature. There is huge interest in quantifying the effective radiative forcing induced by human activity since 1750 (the "pre-industrial period") to aid the accurate prediction of future climate changes (Hansen, Sato, and Ruedy, 1997; Hansen et al., 2005; Myhre et al., 2013; Forster et al., 2016; Bellouin et al., 2020; Smith et al., 2020).

The emission of aerosols since the pre-industrial period has caused a net increase in the outgoing radiation at the top of the atmosphere (a negative radiative forcing) through direct interactions with radiation and through interactions with clouds, which then affect the radiation (Bellouin et al., 2020). Aerosols are solid, liquid or gas particles suspended in the air and they provide a surface for water to condense onto to form cloud droplets, so cloud properties are sensitive to changes in aerosol concentration. The most recent Intergovernmental Panel on Climate Change (IPCC) report, Forster et al. (2021), has estimated the total effective radiative forcing from aerosol as –1.3 [–2.0 to –0.6] W m^{-2} for the period between 1750 and 2014. This number can be broken down into the forcing from aerosol-radiation interactions of -0.3 ± 0.3 W m^{-2} and that from aerosol-cloud interactions as -1.0 ± 0.7 W m^{-2}. This radiative forcing is a significant energy reduction in the Earth system. It partially offsets the effective radiative forcing from carbon dioxide of 2.16 [1.90 to 2.41] W m^{-2} and other forcing agents, resulting in a total anthropogenic forcing of 2.72 [1.96 to 3.48] W m^{-2}. The largest portion of the uncertainty associated with the total forcing comes from the uncertainty in the aerosol forcing and reducing this uncertainty is crucial to more accurately quantify the total effective radiative forcing (Carslaw et al., 2013; Reddington et al., 2017; Regayre et al., 2018; Mülmenstädt and Feingold, 2018; Douglas and L'Ecuyer, 2020; Watson-Parris et al., 2020).

The responses to the temperature increase caused by radiative forcing are called "climate feedbacks" and they either amplify (positive feedback) or reduce (negative feedback) the warming (Forster et al., 2021). The known feedbacks can be divided into four terms relating to: increased emission of longwave radiation; increased atmospheric water vapour and change in lapse rate; changes in albedo, primarily due to loss of land and sea ice; and cloud feedback from changes to cloud amounts, altitude and radiative properties. The longwave feedback (known as the Planck response) is strongly negative

and compensates for the warming, whilst the other three feedbacks are positive and amplify the warming. The signs of each of these feedbacks have been determined with high certainty, however, the magnitude of the cloud feedback is largely uncertain in comparison to the others and this uncertainty propagates through to the magnitude of the net negative feedback (Soden and Held, 2006; Ringer et al., 2006; Vial, Dufresne, and Bony, 2013).

Cloud feedbacks can be positive or negative depending on the balance between changes to the longwave and shortwave effects (Ceppi et al., 2017; Forster et al., 2021). Negative feedbacks come from a reduction in the extent of tropical anvil clouds (more longwave radiated to space) and the replacement of ice crystals with liquid droplets in extratropical clouds which increases the albedo of the clouds (more shortwave reflected to space). The positive feedbacks come from an increase in cloud-top height which enhances the cloud greenhouse effect; an increase in Arctic low-cloud amount (from increased exposure to open water) and consequently their net warming effect; and reductions in cloud amount, primarily over land in the mid-latitudes, and in marine low clouds in the subtropics (reduction in the net-negative cloud radiative effect).

Estimates of radiative forcing and climate feedback are primarily derived from general circulation model simulations, often of future climate scenarios such as a doubling (or quadrupling) of CO_2 emissions or a 2 K increase in sea surface temperature (Cess et al., 1990; Ringer et al., 2006; Zhang et al., 2012; Zelinka et al., 2020). Since many cloud processes operate on small temporal and spatial scales, approximations called "parameterisations" have to be made to represent them on larger scales to make the simulations feasible. However there are usually several possible ways to represent a process and they often contain uncertain parameters, which results in a large spread of predictions between models.

1.2 Stratocumulus clouds

The focus of this thesis is on low, shallow clouds called "stratocumulus", which are often only a few hundred metres thick and typically reside within the lower 2 km of the atmosphere in the region, known as the boundary layer. Stratocumulus clouds are generally characterised as sheets of cumulus cloud cells surrounded by cloud-free rings, each cell on the order of 2 to 10 km, that can stretch homogeneously for many hundreds of kilometres. Table 1.1 gives typical values for marine stratocumulus.

With 80% of stratocumulus occurring over the ocean, they exert a strong net cooling effect on the climate system (Stephens and Greenwald, 1991; Hartmann, Ockert-Bell, and Michelsen, 1992; Wood, 2012). According to Randall et al. (1984), a 4% increase in low-level stratus clouds would offset a 2-3 K rise in global temperature. Much research focuses on marine stratocumulus since small changes in their behaviour can have large

Table 1.1: Typical properties for marine stratocumulus, adapted from Lohmann, Lüönd, and Mahrt (2016), Wood (2012), and Wood (2015).

Parameter	*Typical value*	*Typical range*
Cloud droplet number concentration (cm^{-3})	75	10 to 300
Cloud droplet radius (μm)	7	2 to 12.5
Liquid water path (g m^{-2})	70	40 to 150
Vertical velocity (m s^{-1})	-	0.1 to 1
Vertical extent (km)	0.5	0.2 to 0.7

impacts on the radiation budget, but there are large uncertainties surrounding how stratocumulus respond to climate changes. These uncertainties persist because stratocumulus clouds are particularly sensitive to microphysical processes (order of µm) and eddies (up to around 1 km) that cannot be resolved in general circulation models, which have a typical horizontal grid box of tens of km. Thus, parameterisations of stratocumulus processes, including the response to aerosol, contribute largely to the overall uncertainty in radiative forcing and climate feedback estimates (Bony and Dufresne, 2005; Teixeira et al., 2011; Vial, Dufresne, and Bony, 2013).

Clouds are primarily formed when air parcels rise through the atmosphere, adiabatically cool and become saturated such that the water vapour in them condenses (Carslaw, 2022). In the presence of aerosols, droplets form at a relative humidity of very close to 100%, but without aerosols a relative humidity of around 300% would be required (Quaas and Gryspeerdt, 2022). Air parcels may rise due to convection from surface heating, ascent over orography, weather fronts where warm air is pushed up over cold air, or turbulence from wind and air circulations. Marine stratocumulus form where warm air overlies cold ocean surfaces, creating a stable boundary layer capped by a temperature inversion, where the temperature can increase by up to 20 K within tens metres (Wood, 2012). Much of the marine stratocumulus occurs in the subtropics where inversions are caused by subsiding air from large vertical circulations that are driven by deep convection from tropical ocean temperatures. At the inversion, the overlying warm air begins to cool at the boundary allowing cloud droplets to form.

Stratocumulus clouds follow a diurnal cycle where incident solar radiation may cause them to break up in the afternoon, however they can persist for several days if radiative cooling allows sufficient recovery through the night. Unlike cumulus clouds where turbulence is predominantly driven by surface fluxes (latent and sensible heating), which create updrafts, stratocumulus are largely driven by longwave radiative cooling at the top of the cloud (Lilly, 1968). Water droplets absorb and emit longwave radiation very efficiently and the majority of longwave radiation is absorbed rather than scattered (Nicholls, 1984; Moeng et al., 1996; Wood, 2012). Due to their low altitude, stratocumulus absorb and re-emit longwave radiation at temperatures close to the surface temperature, and therefore have only a small effect on outgoing longwave radiation.

However, the downwelling longwave at cloud top is much smaller than the upwelling, especially since these clouds often lie below a dry free troposphere (Nicholls, 1984). This subjects the top few metres of the cloud to a cooling effect, whilst further into the cloud the downwelling longwave balances with the upwelling longwave from absorption, scattering and emission (Wood, 2012). As well as strengthening the temperature inversion above the cloud creating large horizontal expansion (Siems, Lenschow, and Bretherton, 1993), this cloud-top cooling creates a thermal instability that cools air parcels into downdrafts and drives convective overturning of the air in the cloud.

The longevity of a cloud requires mixing of air to continually bring in water vapour and aerosol as cloud droplets are evaporated and mixed away or fall out of the cloud. Air is entrained into stratocumulus clouds at their tops, mixing cloudy air with clear air. The rate of entrainment depends on thermodynamic processes, like longwave cooling and evaporation of droplets, as well as dynamical processes like wind shear (Duynkerke, 1993; Mellado, 2017). Entrainment of unsaturated air into the top of the cloud cools and moistens it due to droplet evaporation, which reduces its buoyant energy and the overall buoyancy in the cloud-top region (Lilly, 1968; Randall, 1980). Thus, entrainment generates more turbulence, which sustains the cloud by providing new aerosol and moisture, whilst also increasing droplet evaporation from mixing in dry air. Buoyancy reversal occurs when evaporative cooling is large enough to create negatively buoyant air parcels, which in turn can feed back to increase entrainment (evaporation-entrainment feedback) (Deardorff, 1980; Randall, 1980). This was thought to cause a runaway feedback (called cloud-top entrainment instability) that could dissipate the cloud in tens of minutes. However, it has since been found that such an instability does not exist without other factors counteracting it (Siems et al., 1990; Mellado, 2017). The factors that affect cloud-top entrainment instability are explored in Chapter 3.

In many cases, a marine stratocumulus-topped boundary layer is a "well-mixed" layer, which means the length of the vertical mixing is large enough that the largest eddies reach from the surface to the cloud top, and profiles of potential temperature and total water mixing ratio are constant (Nicholls, 1984). In these cases, the stratocumulus is sustained by longwave cooling driving the convection, with access to the moist surface layer (the ocean) as a source of water vapour that is mixed throughout the layer (Wood, 2012). If the boundary layer becomes too deep, longwave cooling is no longer sufficient to drive such large eddies and the boundary layer becomes "decoupled" from the surface (Nicholls, 1984; Klein, Hartmann, and Norris, 1995; Bretherton and Wyant, 1997; Wyant et al., 1997; Wood, 2012). This results in a well-mixed cloud layer that is separated from the subcloud layer by a shallow stable layer, which the mixing does not cross. The subcloud layer is still coupled to the ocean as a moisture source and, without mixing driven by cloud-top longwave cooling, it becomes driven by surface latent and sensible heat fluxes, which may produce cumulus clouds. Although the

cumulus clouds may provide enhanced updrafts and temporarily provide moisture to the upper cloud layer, eventually the upper cloud layer will dissipate due to mixing with free-tropospheric air. Decoupling often varies diurnally, with the stratocumulus cloud recovering during the night when longwave cooling increases due to the lack of incident solar energy.

Low-level stratocumulus are warm clouds in that their precipitation is all liquid phase. A drizzle droplet has a radius on the order of 0.1 mm, whilst a rain droplet has a radius around 1 mm (a cloud droplet is around 7 µm, see Table 1.1) (Lohmann, Lüönd, and Mahrt, 2016). When drizzle droplets reach a large enough radius to overcome the updraft velocity they fall through the cloud removing moisture and aerosol from the cloud layer. Stratocumulus clouds generally produce light drizzle, if any, rather than very heavy precipitation because they have weak updrafts, around 0.01 m s^{-1}, compared with deeper, surface-driven cumulus clouds of up to 10 m s^{-1} (Lohmann, Lüönd, and Mahrt, 2016). Below cloud base, drizzle droplets encounter a relative humidity of less than 100% so they begin to evaporate causing cooling and moistening in the sub-cloud layer, which stabilises the boundary layer and inhibits deep mixing (Stevens et al., 1998). Cloud droplets also experience gravitational settling (sedimentation). The removal of moisture from the cloud top region, by sedimentation or precipitation, reduces the moisture available for evaporative cooling and thus the kinetic energy available for entrainment (Nicholls, 1984; Ackerman et al., 2004). Precipitation generally leads to thinning of stratocumulus clouds, sometimes resulting in cloud breakup, through reductions in liquid water content and mixing. Sedimentation without below-cloud precipitation can lead to increased liquid water content since entrainment is reduced but the water remains in the cloud (Ackerman et al., 2004; Bretherton, Blossey, and Uchida, 2007).

Stratocumulus clouds are sensitive to their surroundings because they are thin so they are easily diminished or dissipated by processes that promote evaporation of cloud droplets. Additionally, albedo sensitivity to changes in droplet concentration is largest for the range of liquid water paths (vertically integrated liquid water content) between 50 to 200 g m^{-2}, which includes most stratocumulus (Wood, 2012). This means that small changes in the environment can have a large effect on the local cloud radiative effect. For example, depletion of moisture from the cloud layer by drizzle and the resulting convection can generate pockets of open cells, where cells of cloud-free air are lined by cloud, rather than the closed cells previously described (Stevens et al., 2005b). Of particular interest in this thesis is the transition from stratocumulus to cumulus clouds, which can more than halve the fraction of the surface covered by cloud and consequently the albedo of the area (Albrecht et al., 1995; Sandu, Stevens, and Pincus, 2010; Zhou, Kollias, and Lewis, 2015; Albrecht et al., 2019). Many kilometres of stratocumulus decks break up in this way as cloudy air is advected over warmer

sea surface temperatures towards the equator, yet there are still questions about what changes these transitions are sensitive to. This transition is explored in Chapters 4 and 5.

The responses of marine low-cloud amount to global warming result from the combined effects of increasing sea surface temperature, large-scale circulation changes, and changes in the free troposphere (Zhang et al., 2013; Bretherton and Blossey, 2014; Bretherton, 2015; Nuijens and Siebesma, 2019; Zelinka et al., 2020). There is a predicted weakening in large atmospheric circulations, which would decrease subsidence and hence the strength of temperature inversions. Weakened subsidence results in increased cloud-top entrainment, the raising of cloud tops and the thickening of stratocumulus clouds (negative feedback). Additionally, with the change in lapse rate (Forster et al., 2021), the free troposphere warms faster than the ocean surface, which increases the inversion strength thereby lowering both cloud top and base, and also thickening the cloud (negative feedback). However, the net positive response is determined by two compensating positive feedbacks from reductions in cloud amount. First, a "thermodynamic" mechanism follows the increase in sea surface temperature, which increases surface fluxes, convection and hence entrainment at cloud top. Second, a "radiative" effect from the increased water vapour in the atmosphere increases the downwelling longwave radiative. This reduces cloud-top cooling and subsequently, entrainment which lowers the cloud top.

1.3 Aerosol-cloud interactions

Sources of aerosols can be natural, such as volcanic ash and salt particles from sea spray (Carslaw et al., 2010), or anthropogenic, such as black carbon and other particulate matter from vehicle and agriculture emissions (Klimont et al., 2017). Aerosols directly affect the radiative budget through absorption and scattering of shortwave radiation, with the sign and magnitude of the local forcing depending on the aerosol composition and the albedo of the surface which it overlays. Scattering aerosols increase local albedo but will have a much larger effect overlying dark parts of the planet rather than bright areas that already have a high albedo (Bellouin et al., 2020). Absorbing aerosols appear dark and so they have the opposite effect. These albedo effects are termed the "instantaneous" radiative forcing, but the effective aerosol-radiation interactions also include adjustments to the instantaneous forcing. In low, shallow clouds absorbing aerosol lying below the cloud heats the boundary layer which may increase decoupling and decrease cloud amount. Conversely, absorbing aerosol lying above the cloud heats the free troposphere and strengthens the capping inversion which may increase cloud amount (Johnson, Shine, and Forster, 2004; Hill and Dobbie, 2008; Yamaguchi et al., 2015; Carslaw, 2022). Diamond et al. (2022) discussed how the specifics of the aerosol-radiative effect and the following adjustments are still rather uncertain.

Most of the aerosol forcing comes from aerosol-cloud interactions through the role of aerosol as nuclei for cloud droplets (Carslaw, 2022). As air parcels rise and approach saturation, water vapour condenses and moistens a subset of aerosol particles that act as cloud condensation nuclei. As the humidity continues to increase, these nuclei grow in size through further condensation until the air becomes supersaturated and they reach a critical diameter, at which they are "activated" as cloud droplets. Beyond this point, the droplets continue to grow despite supersaturation beginning to decrease. If the available liquid water content in a cloud is constant, increasing the concentration of aerosol particles provides more cloud condensation nuclei and so the liquid water gets distributed between more droplets. The increase in droplet number concentration increases the droplet surface area and consequently the cloud's optical depth and albedo. This instantaneous effect is known as the Twomey effect (Twomey, 1974).

Following an increase in droplet number concentration and reduction in droplet radii, several cloud adjustments can occur. Processes that increase turbulent mixing and bring moisture into the cloud (or prevent it leaving) act to increase the liquid water path and cloud lifetime:

1. The formation of drizzle or rain droplets is strongly dependent on the size of the cloud droplets so a reduction in droplet radii may suppress precipitation and retain moisture and aerosol in the cloud layer (Albrecht, 1989).

2. Increasing the droplet surface area can cause an increase in condensation rate and latent heating, which drives vertical expansion of the cloud, in what is known as cloud invigoration (Pincus and Baker, 1994; Christensen and Stephens, 2011; Douglas and L'Ecuyer, 2021).

Conversely, processes that increase evaporation and entrainment tend to dry the cloud layer leading to a decrease in liquid water path and possibly cloud thinning:

1. With smaller cloud droplets there is less gravitational settling within the cloud, so moisture remains near the cloud top and has more evaporation potential, which increases turbulent mixing and entrainment (Ackerman et al., 2004).

2. Smaller droplets are evaporated more efficiently so this also increases entrainment, and can create an evaporation-entrainment feedback (Ackerman et al., 2004).

3. In Arctic stratocumulus, Williams and Igel (2021) have recently found that the increase in entrainment with the addition of aerosol is actually from an increase in longwave cooling which also drives entrainment.

Generally it is found that in precipitating clouds, the suppression of precipitation acts to increase the liquid water path, whereas in non-precipitating clouds the increased entrainment rates decrease the liquid water path (Gryspeerdt et al., 2019).

1.4 Cloud-controlling factors in low, shallow clouds

Cloud properties depend on the environment in which they exist so changes in the environment can lead to changes in cloud properties. The environment is made up of all the cloud-controlling factors including surface properties (orography, temperature, convection, moisture sources), meteorological factors (pressure, temperature, humidity, winds), large-scale dynamics (subsidence), radiation, and aerosol concentrations.

Some of the key effects of environmental changes are as follows. For marine stratocumulus, the ocean is a moisture and aerosol source. So surface temperatures affect convection and turbulence, through sensible and latent heating, but also determine how much evaporation occurs. Additionally, wind whips up sea spray adding sea salt particles, which are aerosols, to the air. The relative humidity, which controls droplet formation, is determined by pressure, temperature and available water vapour. Cloud dissipation by entrainment depends largely on the temperature and humidity of the above-cloud air (van der Dussen, de Roode, and Siebesma, 2014). Subsidence, the rate of air descending through the troposphere, affects the depth of the boundary layer and entrainment rate. The diurnal cycle creates a cycle in the strength of longwave cooling. Aerosol effects have already been discussed, but the outcome of adding aerosol can largely depend on the rest of the environment. For example, the effect on precipitation of adding aerosols into a cloud can depend on the initial cloud droplet number concentration (Ackerman et al., 2004).

It can be difficult to untangle aerosol-cloud interactions in observations because factors interact with each other and a change can initiate several different processes that may counteract each other (Stevens and Feingold, 2009). For example, low relative humidity in the free troposphere enhances longwave cooling, which generally increases cloud amount, but it also increases drying through entrainment, which can reduce cloud amount. Possner et al. (2020) found that the longwave effect had a larger impact on liquid water path and the cloud was thickened. Another example is the cloud lifetime effect discussed above. Wood (2007) discusses how cloud thickening depends on the balance between moistening and cooling from precipitation suppression and drying and warming from increased entrainment. The entrainment is increased through additional turbulence since the suppression of precipitation also suppresses the stabilising effect of precipitation evaporation in the boundary layer (Pincus and Baker, 1994).

1.4.1 Satellite analysis

Satellite observations used in conjunction with reanalysis data along cloudy trajectories have provided insight into the meteorological factors controlling cloud transitions into new cloud states. This technique was first established by Pincus, Baker, and Bretherton (1997), partly motivated by the fact that stratocumulus are not only impacted by

their current environmental conditions, but also by previous conditions. For example, Mauger and Norris (2010) found that subtropical cloud cover responds most strongly to surface divergence on timescales of 12 hours or less and beyond that it becomes more sensitive to lower-tropospheric stability and sea surface temperatures. Sandu, Stevens, and Pincus (2010) characterised the stratocumulus-to-cumulus transition in ocean basins across the world by compositing thousands of trajectories into climatology cases, one climatological case will be simulated in Chapter 4. More recently, Eastman, McCoy, and Wood (2022) found that closed-cell stratocumulus appears to break up into open-cell stratocumulus following strong winds and large moisture fluxes, whereas following increases in sea surface temperature and excess entrainment it breaks up into a disorganised (cumulus-like) regime.

Aerosol relationships with cloud properties can also be assessed from retrievals of droplet number and aerosol optical depth. Also shiptracks cam be used as a "natural laboratory" to understand how aerosol plumes alter cloud properties with a natural control in the neighbouring unaffected cloud. Christensen and Stephens (2011) observed cloud top heights to increase in the presence of shiptracks, but found much larger changes in regions of open cell stratocumulus (generally more moist and unstable) than closed cell stratocumulus (generally more dry and stable). Gryspeerdt et al. (2019) showed the nonlinear relationship between droplet number concentration (N_d) and liquid water path. At low N_d where precipitation is expected, increasing N_d increases liquid water path through precipitation suppression, but at high N_d, liquid water path decreases, most likely due to the decreased sedimentation, increased evaporation and entrainment of smaller droplets. Possner et al. (2020) found the same positive relationship in precipitating clouds, but also split their data into boundary layer depth regimes and found cloud adjustments to N_d were greater in deeper boundary layers.

1.4.2 High-resolution modelling

The availability of satellite data in such vast quantities (and the computing power to process them) is a rather recent development, whereas high-resolution cloud models have been a key tool for many decades and have provided much of the current understanding of stratocumulus clouds. The use of three-dimensional fluid dynamics models, called large-eddy simulation (LES) models, in boundary layer studies began with work by Deardorff (1974) and Moeng (1984). LES models have been widely used since those initial simulations, which began to explore the sensitivity of turbulence structure to entrainment and were just 40 grid points along a 5 km horizontal domain for a single day. Since then computational power has improved greatly. Yamaguchi, Feingold, and Kazil (2017) simulated a 3-day cloud transition with 480 grid points along a 24 km horizontal domain. Furthermore, in the last few years groups have suggested embedding LES models within global climate models to more accurately simulate turbulence for

low-level clouds (Schneider et al., 2017).

LES models have been used to study the effect of different environmental conditions on stratocumulus-topped boundary layers. Unlike satellite observations, specific cloud-controlling factors can be isolated and studied using idealised LES. Xu and Xue (2015) found that cooler and moister air above the boundary layer gradually cools and moistens the boundary layer too, creating lower cloud bases and higher cloud tops. Bellon and Geoffroy (2016) found that low sea surface temperatures could produce very different boundary layer states depending on the initial conditions, with initially deep boundary layers producing a stratocumulus regime and initially shallow boundary layers producing a clear sky regime. van der Dussen, de Roode, and Siebesma (2016) found that a weakening of subsidence caused a higher liquid water path and extended the cloud lifetime (similar to Sandu and Stevens, 2011). Zheng, Zhang, and Li (2021) found that the increase in surface latent heat flux plays a crucial role in sustaining decoupling during the transition from stratocumulus to cumulus clouds, but the decoupling is initiated by entrainment of warm air from above.

LES have also been used increasingly to assess aerosol-cloud interactions, either through cloud droplet number or an aerosol representation in the microphysics scheme. Zhou, Heus, and Kollias (2017) found that precipitation has a nonlinear relationship with cloud amount but below a threshold of $N_d = 15$ cm^{-3}, precipitation causes a sudden decrease in cloudiness. Yamaguchi, Feingold, and Kazil (2017) found a particularly fast cloud break up at low aerosol when drizzle from cumulus below stratocumulus was uplifted to the stratocumulus layer and initiated heavy depletion of aerosol and moisture. Goren et al. (2019) showed that adding aerosol delays cloud break up, but the nature of the delay is determined by how the wider meteorology affects the liquid water path. Wyant et al. (2022) found that small aerosol particles (known as the Aitken mode) can increase cloud droplet numbers when the largest of them are activated, which can increase cloud lifetime in regions of low aerosol concentrations.

Yet even within LES models, the subgrid, microphysical and radiation processes need to be parameterised, and model intercomparison projects have been used to understand the differences between models caused by different approaches. Following observational campaigns, researchers challenged LES models to recreate observed conditions and compared the model results (Moeng et al., 1996; de Roode and Duynkerke, 1996; Stevens et al., 1998; Bretherton et al., 1999b; Bretherton et al., 1999a; Stevens et al., 2003; Stevens et al., 2005a). Bretherton et al. (1999a) found that the vertical resolution at cloud top needs to be around 5 m to get reliable entrainment rates. van der Dussen et al. (2013) found large discrepancies between liquid water paths in the stratocumulus-to-cumulus transition due to the precipitation parameterisations. The launch of the CGILS (CFMIP-GASS Intercomparison of LES and SCM models) project produced many studies using the same technique but for various climate forcings, such

as a 2 K sea surface temperature increase and, more recently, a quadrupling of CO_2 (Teixeira et al., 2011; Zhang et al., 2012; Zhang et al., 2013; Blossey et al., 2013; Blossey et al., 2016). These studies focused on three cases of low, shallow clouds across the stratocumulus-to-cumulus transition. They found strong agreement in the models on the thermodynamic and dynamic responses, but the degree of each effect, and therefore the net effect, depended on the individual model.

With many of these studies, it is difficult to build a complete picture of the main causes of uncertainty because the problems are only sparsely sampled. Whether it is assessing the differences between models, trying to understand the main drivers in a process, or the different end states produced by different environmental conditions. Each problem has some number of variable inputs to it and usually only a few values for each factor are considered. The reality is that each factor present in the process, or parameterisation, has a range of values it could take and many (very different) combinations of factors are feasible, which is a property known as "equifinality". In the case of the most recent CGILS project, the perturbations are simulated on 6 models. There are numerous differences in the parameterisations between the models creating a high-dimensional parameter uncertainty space, but each model is only one point in that space. In many process-level studies, one-at-a-time perturbations are made for only a couple of values per factor.

1.5 Statistical methods to understand cloud behaviour

The dependency of cloud responses on different cloud-controlling factors could be thoroughly explored using Gaussian process emulation via "perturbed parameter ensembles" (O'Hagan, 2006). Perturbed parameter ensembles (PPEs) are created by perturbing multiple parameters simultaneously, rather than the usual one-at-a-time method. In a 2-parameter ensemble, every simulation would have different values of each parameter and the ranges they are perturbed over form the dimensions of a "parameter space" (left in Figure 1.1). PPEs can inform us about the joint effects between parameters and they can be used as training data for Gaussian process emulation. Knowledge about the joint effects of parameters is particularly useful for the nonlinear and chaotic nature of clouds.

Gaussian process emulation is a machine learning technique that approximates the function between a set of inputs (the parameters) and an output of interest to create a surrogate model, which can be densely sampled for a fraction of the computational cost of running the actual model. The dense sampling is crucial to extend our knowledge of the parameter space, which has only been sparsely sampled by the PPE due to the computational expense of running the actual model. This sampling allows quantification of the output sensitivity to each parameter and visualisation of the relationships,

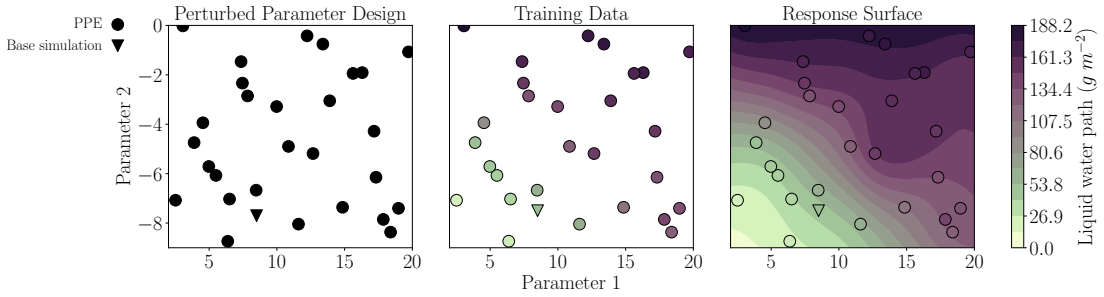

Figure 1.1: Creating a response surface from a PPE. Left shows the distribution of parameter values in a 2-dimensional parameter space; middle shows the model values at those points; and right shows the emulator predictions filling parameter space as a response surface. The triangle shows the values of the base simulation, from which the parameters have been perturbed (circles).

which can give insight into the joint effects of parameters. Figure 1.1 shows how the relationship between two parameters and the liquid water path can be visualised, first using the PPE data alone and then by sampling parameter space with the emulator and creating a "response surface" (discussed in Chapter 3).

These methods are often used to quantify and reduce uncertainty in the model, where the perturbed "parameters" are uncertain coefficients in model parameterisations. But they can also be used to further process-level understanding where the "parameters" are initial or boundary conditions, such as the cloud-controlling factors we consider here. In these cases, the emulator is an approximation of the relationship between a set of cloud-controlling factors and some cloud property that we are interested in. The emulator can be used to visualise this relationship and sensitivity analysis can be used to identify the major drivers behind processes.

Gaussian process emulation was pioneered in aerosol model studies through sensitivity analysis of cloud condensation nuclei to uncertain parameters in a global aerosol model (Saltelli, Chan, and Scott, 2000; Johnson et al., 2015; Regayre et al., 2014; Regayre et al., 2015; Regayre et al., 2018; Lee et al., 2011; Lee et al., 2013). With this method, the output variance can be decomposed into the effect from each uncertain parameter and also the joint effect of that parameter and its interactions with other uncertain parameters. Lee et al. (2011) perturbed eight model parameters and found that in polluted environments the uncertainty in sulphur emissions is responsible for the majority of output uncertainty, but in remote regions, parameter interaction effects become more important than any individual parameter. This work was extended to 28 parameters in Lee et al. (2013).

From the dense sampling of emulators, response surfaces can be produced which enable visualisation of the combined effects of the uncertain parameters and the output of interest (Figure 1.1, right). For up to 3 parameters, it is possible to visualise the

whole response surface as done in Marshall et al. (2019) and Marshall et al. (2021) for volcano eruptions. Glassmeier et al. (2019) perturbed a 6-dimensional parameter space but emulated and visualised it by transforming it to a 2-dimensional state space, showing how liquid water path and droplet number affect the cloud radiative effect. One-dimensional relationships between each parameter and the output of interest can also be viewed clearly and this highlights the parameters which cause the most variance (Lee et al., 2011).

The uncertain parameter ranges can be constrained using observations of the output of interest or linked quantities (Johnson et al., 2018; Regayre et al., 2018; Regayre et al., 2020). Implausible regions of the parameter space can be ruled out by assessing the output values produced across the parameter space by the emulator and comparing them against observations. This removes some model variants (realisations of the model produced by different combinations of parameters) and can reduce the uncertainty ranges elicited for each parameter, which moves the possible parameter values to a more appropriate range. For multiple model outputs that have common causes of uncertainty, observations of one model output can constrain another, harder-to-observe output.

The PPE and emulator techniques have been successfully extended to understand cloud processes, initially by Johnson et al., 2015 in convective clouds, but later through several studies on marine stratocumulus (Glassmeier et al., 2019), deep convection and hail (Wellmann et al., 2018; Wellmann et al., 2020), and sea breeze extent and aerosol distribution, which affect the formation of clouds (Igel, van den Heever, and Johnson, 2018; Park et al., 2020). These studies perturbed initial meteorological conditions and cloud-controlling factors to learn about their joint effects on different cloud and aerosol properties. Additionally, Johnson et al. (2015) identified distinct cloud behaviours (or regimes) in the precipitation response to perturbing aerosol concentrations: at low concentrations the accumulated precipitation was stable, but at high concentrations, the precipitation decreased sharply with increasing aerosol. Sensitivity analysis revealed that the main factors affecting the cloud properties differed considerably between the four regimes. The identification of such regimes would not have been feasible without emulation.

In Gaussian process emulation, there is a fundamental assumption that the model output is a smooth, continuous function of its inputs (O'Hagan, 2006). But the complex behaviour of clouds in atmospheric modelling does not guarantee a smooth dependence of cloud properties on cloud-controlling factors, and often erratic behaviour is observed. The rapid development of pockets of open cells in stratocumulus clouds under a certain set of environmental conditions is a good example of sharp changes in cloud properties (Stevens et al., 2005b). Generating a statistical representation of non-stationary output is an active area of research (Gramacy and Lee, 2008; Montagna and Tokdar, 2013; Volodina and Williamson, 2018; Mohammadi et al., 2019; Pope et al., 2021). Pope

et al. (2021) used data from Johnson et al. (2015) on convective clouds that were found to display discontinuous behaviour between cloud regimes. They partitioned the parameter space into Voronoi tessellations (Green and Sibson, 1978) and applied the Gaussian process to each partition. They also allowed the joining of regions to create more complex shapes around discontinuities. In both of our case studies, we attempt to identify sharp changes in parameter space between regimes.

Gaussian process emulation creates a surrogate model of the complex model. The surrogate is "naive" in that it is not trained with any physical knowledge of the system in the real world, rather it only statistically approximates the relationship between the input values and the outputs of interest. As such, the surrogate's interpretation of the training data is subject to any structural errors from the complex model, limited to the perturbed parameter ranges, and cannot produce more realistic results than the complex model itself. The method does allow parameter spaces to be densely sampled in a way that is unfeasible with the complex model itself, which allows a broad analysis of the complex model's behaviour and identification of relationships that may otherwise go unnoticed.

1.6 Research approach

The largest causes of uncertainty in estimates of radiative forcing and climate feedbacks relate to aerosol-cloud interactions and cloud-climate feedbacks. A significant portion of these uncertainties are due to difficulties in simulating low, shallow clouds and their responses to changes in environmental conditions, including aerosols. These clouds have a large cooling effect on the planet so a small change in their extent or physical properties can offset or amplify a significant amount of CO_2-induced warming, which is why we are concerned with reducing this uncertainty to more accurately understand our past and predict our future climate.

Three challenges shape the approach taken in this thesis. 1) High-resolution simulations of clouds are required to fully understand cloud responses to changes in their environment and identify mechanisms that cause large changes in cloud cover and thickness. 2) Cloud mechanisms are complex and driven by many interacting cloud-controlling factors. It can be hard to distinguish between different drivers in observations and in simulations that only perturb one factor at a time. 3) Parameterisations in global climate models are unable to resolve the small-scale processes that these clouds are very sensitive to, so are unable to accurately capture cloud behaviours producing large uncertainties in climate predictions. Exploring these aspects thoroughly requires advanced statistical techniques to efficiently use high-resolution model output to further process-level understanding of clouds.

This project uses PPEs and statistical emulation to improve our understanding of

stratocumulus cloud responses to changes in cloud-controlling factors. In Chapter 3, the free-tropospheric specific humidity and temperature are perturbed relative to a simulation of homogeneous and temporally stable stratocumulus. That chapter aims to demonstrate the application of PPEs and the interpretation of response surfaces. It also explores how natural variability can be incorporated into the emulator technique to create response surfaces that represent deterministic cloud behaviour rather than the quasistochastic nature of the model. Chapter 4 simulates a stratocumulus-to-cumulus transition and explores the effects of 6 parameters: 5 cloud-controlling factors and 1 model parameter. This ensemble is analysed to assess whether low-aerosol environments cause faster transitions through a drizzle-depletion effect. Chapter 5 uses the same PPE as training data for Gaussian process emulators of the transition properties which are densely sampled thousands of times. These dense samplings are used to understand the joint effects and quantify the sensitivity of the transition properties to each factor.

The questions to be answered are as follows.
Chapter 3:

1. Is there a cloud-breakup threshold separating two cloud regimes?
2. How well can we characterise the spatial change in cloud behaviour across parameter space using statistical emulation? Is there a discontinuity or a shallow gradient between the regimes?
3. How can we account for the cloud's natural variability in the emulators so that the response surfaces represent deterministic cloud behaviour rather than stochastic realisations of the model?

Chapter 4:

1. Do the fastest transitions from stratocumulus to cumulus occur in the regions of low aerosol concentration?
2. What other cloud-controlling factors determine the time taken to transition? How important is one of the autoconversion rate parameters compared to the cloud-controlling factors?
3. Under what conditions does drizzle play an important role in the transition?

Chapter 5:

1. Using Gaussian process emulation, which factors is the time taken to transition most sensitive to?
2. To understand the drivers of drizzle, which factors is the rain water path most sensitive to?

3. What additional information do we gain from using emulator predictions for thousands of new parameter values that we did not have from the PPE analysis in Chapter 4

Chapter 2

Models and methods

2.1 Models

2.1.1 Large-eddy simulation

This work uses a large-eddy simulation (LES) model called the UK Met Office/Natural Environment Research Council (NERC) Cloud (MONC) model (Gray et al., 2001; Brown et al., 2020). MONC uses the same underlying science as the UK Met Office's original large-eddy model (the LEM), which was developed in the late 1980s, but it was written as a new model throughout the 2010s to make it suitable for use on modern high-performance computers. For example, the LEM could only be run on up to 512 cores, whereas ARCHER2 (the UK's national supercomputing service, which came into use in 2021) has over 700,000 cores available. The LEM was a primary tool in developing parameterisations for the Unified Model and contributed simulations to many LES model intercomparisons that tested model abilities for reproducing observations of shallow, low clouds (Moeng et al., 1996; Bretherton et al., 1999a; Pier Siebesma et al., 2003; Stevens et al., 2005a; van der Dussen et al., 2013) and the CGILS cloud-climate feedback intercomparisons (Teixeira et al., 2011; Zhang et al., 2013; Dal Gesso et al., 2015; Blossey et al., 2016).

The MONC model solves a Boussinesq-style approximation of the Navier-Stokes equations of motion, assuming that differences in density are negligible (Gray et al., 2001). It solves equations for momentum conservation, mass continuity and thermodynamics using a reference state defined by density, temperature and pressure from which perturbations are assumed to be small. It can be used for an incompressible system, where the reference state is constant with height, or for an anelastic system, where the reference state is a function of height. The incompressible assumption is suitable for most shallow cloud applications, but the anelastic case is appropriate for deeper simulations. In MONC, the user sets the reference potential temperature and then the

reference density and pressure are calculated from the ideal gas law and the hydrostatic equation, given the surface pressure as a boundary condition.

"Large-eddy" simulations are so called because they explicitly resolve large-scale turbulent eddies, which contain the majority of the energy of motion and filter small-scale turbulence into a subgrid turbulence approximation, which also deals with unresolved diffusion and viscosity. In the MONC model, the subgrid calculations are based on the Smagorinsky (1963) model for eddy viscosity and diffusivity, with the addition of the effect of buoyancy on energy production from Lilly (1962). The size of the horizontal grid boxes is constant but the size of the vertical layers can vary through the domain. MONC is capable of resolving down to just a few meters. We used horizontal grid box sizes between 30 to 50 m and vertical layers between 5 to 20 m in the boundary layer stretching up to 100 m near the top of the vertical domain. The first domain used here was 7.5 by 7.5 by 1.5 km^3 and the second domain was 12.75 by 12.72 by 3.1 km^3

The boundary conditions in the MONC model are periodic in the horizontal for all prognostic variables. The top and bottom are rigid lids with the vertical velocity being zero at each surface. The bottom surface can interact with variables through frictional stresses and surface sensible and latent heat fluxes. Having the top surface as a rigid lid can lead to gravity waves being reflected, which is generally not realistic, so a damping layer of a specified size is added at the domain top above which the prognostic variables are relaxed to their horizontal mean values.

The architecture of the MONC model uses a "plug and play" approach to the various components around the model core. This approach allows easy switching between different schemes, for example between a "simple cloud" microphysics approximation and a bulk two-moment microphysics scheme. There is also a choice of two advection schemes, either Piacsek and Williams (1970) or the total variance diminishing scheme from Leonard, MacVean, and Lock (1993). To maintain numerical stability, an adjustable timestep is used based on the "CFL" number of Courant, Friedrichs, and Lewy (1928). This calculates the CFL number and ensures the timestep remains below the set criteria.

The MONC model can be coupled to a microphysics model and a radiation model. Although some of the processes within these models are now very well understood, such as aerosol activation, they are still very complex to fully resolve and so these models use parameterisations and look-up tables.

2.1.2 Microphysics scheme

The microphysics scheme used is the Cloud AeroSol Interacting Microphysics (CASIM) model, which was developed to be used in both the UK Met Office Unified Model and in the LEM (Shipway and Hill, 2012; Grosvenor et al., 2017). It has been used in the

MONC model for several warm-cloud studies including assessing warm-rain parameterisation (Hill, Shipway, and Boutle, 2015), droplet sedimentation in clouds over West Africa (Dearden et al., 2018), and aerosol activation in fog simulations (Poku et al., 2021). Field et al. (2023) details CASIM parameterisations and implementations in the Unified Model and includes details on its implementation in the MONC model.

CASIM can simulate up to five hydrometeor species when ice processes are included. However, this work is only concerned with warm-cloud processes. Here, the cloud prognostic variables are cloud liquid and rain droplets. The particle size distributions are represented using gamma distributions,

$$N(r) = N_0 r^{\mu} e^{-\gamma r}, \tag{2.1}$$

where r is a measure of size, N_0 is the distribution intercept parameter, μ is the shape parameter and γ is the slope parameter (Shipway and Hill, 2012). The k^{th} moment is then defined by,

$$M_k = \int r^k N(r) dr. \tag{2.2}$$

CASIM can use up to three moments to define prognostics and here we use two: number concentration and mass mixing ratio. The number concentration is the zeroth moment, $M_0 = N_0$, and the mass mixing ratio is the third moment, e.g., for a log-normal distribution $M_3 = \frac{4}{3}\pi r^3 N_0 exp(\frac{9}{2} ln^2 \sigma)$.

CASIM can be used without aerosol, where the user defines a fixed cloud droplet number concentration, or with aerosol and with varying degrees of in-cloud processing. When aerosol is included, it is also represented by number concentration and mass mixing ratio prognostics, and these are configured as initial profiles of Aitken, accumulation and coarse modes. Insoluble aerosol can be included, but here we have only used soluble aerosol. At saturation, the number of aerosol particles activated into cloud droplets is calculated using the scheme of Abdul-Razzak and Ghan (2000), which integrates over distributions of aerosol number and updraft velocity, and these activated aerosol are represented using a separate in-cloud mass mixing ratio prognostic.

Condensation and evaporation are calculated by a saturation adjustment scheme, where at saturation any surplus water vapour in the grid box condenses onto the number of cloud droplets and any deficit evaporates droplets and returns aerosol to interstitial aerosol modes (Field et al., 2023). This scheme keeps the relative humidity within the cloud at 100%, i.e., supersaturation does not occur, and each grid box has either a cloud fraction of 1 or 0 depending on whether it is saturated or not. Condensation of water vapour onto rain cannot occur because supersaturation is not possible. Rain

evaporates in the cloud-free (sub-saturated) grid boxes, but aerosol is not returned to the size modes through this process. Sedimentation advects cloud and rain droplets downwards through the boundary layer according to their fall velocities. Mixing of new air from above the cloud into the cloud layer is homogeneous, which means new air is mixed in with the cloudy air before the evaporation calculation takes place so all droplets are evaporated equally until saturation is reached. This means that there is a reduction in cloud droplet radius, but cloud droplet number is not affected.

The microphysical collection processes follow the Khairoutdinov and Kogan (2000) parameterisation, though MONC can now use the parameter values from Kogan (2013) (more suited to cumulus) (Field et al., 2023). "Autoconversion" is the self-collection of cloud droplets to form rain droplets and its rate is defined by,

$$P_{raut} = 1350 q_w^{2.47} \left(\frac{n_w \rho}{10^6} \right)^{1.79}, \tag{2.3}$$

where q_w is cloud water mass mixing ratio, n_w is cloud water number concentration and ρ is the air density. Autoconversion results in a decrease in cloud droplet number and mass and an increase in rain droplet number and mass. "Accretion" is the collection of cloud water by rain and its rate is defined by,

$$P_{racw} = 67 (q_w q_r)^{1.15}, \tag{2.4}$$

where q_r is the rain water mass mixing ratio. Accretion results in a decrease in cloud droplet number and mass, and an increase in rain mass but not droplet number.

The aerosol can be processed to different degrees: aerosol activation only; activation plus transferal to the in-cloud activated prognostic; or activation, transferal and mechanical growth of particles. The growth occurs with the aggregation of droplets, which increases the aerosol mass per particle and decreases the number. On evaporation, one aerosol particle per hydrometeor is returned to the appropriate interstitial aerosol mode according to their radius (Miltenberger et al., 2018).

2.1.3 Radiation

Where a diurnal cycle is not required, the MONC model can be used with only a parameterisation for longwave cooling and warming rates at cloud top and base. The cooling rates are calculated from liquid water content using an exponential decay function, which is based on the calculation for radiatively active smoke used in Bretherton et al. (1999a).

The radiation model used for diurnal simulations is the Suite of Community RAdiative Transfer codes based on Edwards and Slingo (1996) (SOCRATES) and it was

also designed to be used in the Unified Model (Manners et al., 2015) and was adapted for coupling to the MONC model. It uses a two-stream approximation, where radiation is considered to propagate along two discrete directions, upwards and downwards, in the longwave and shortwave regions of the spectrum. The scheme reads in files that break down atmospheric radiation into spectral bands, which can then be considered to have uniform radiative properties. These files also contain information such as the physical nature of atmospheric gases and aerosols, the fraction of the solar spectrum in each band, the list of gaseous absorbers in each band, and absorption coefficients.

2.2 Perturbed parameter ensembles and statistical emulation

A perturbed parameter ensemble (PPE) is a set of simulations in which multiple parameters have been changed simultaneously. The parameters in this work are mostly cloud-controlling factors, though one uncertain model parameter from the autoconversion parameterisation is added in Chapter 4. Each parameter is assigned a range of likely values to be perturbed across. For the cloud-controlling factors, we have used ranges that are typical values that might be found for stratocumulus clouds in the region. For the uncertain autoconversion parameter, the range is chosen to give a realistic set of autoconversion rates.

The specific values that are used within each parameter's range are chosen using a space-filling design so that it samples the multi-dimensional parameter space as effectively as possible. Since some parameters will be more influential than others in a high-dimensional parameter space, regular grid designs are avoided such that replication of design points does not occur on projection to lower dimensions. The effect of this can be seen in Figure 2.1. If Parameter 1 alters the output only a small amount compared to Parameter 2 (i.e., the dimension of Parameter 1 "collapses"), then the four perturbations across the range of Parameter 1 are just repeating information from other simulations.

The "maximin" Latin hypercube design by McKay, Beckman, and Conover (1979) uses a simulated annealing approach to finding a design that maximises the minimum distance between the design points. Jones and Johnson (2009) found this algorithm to give the best results for Gaussian process emulation, with the recommended number of design points being 10 times the number of perturbed parameters, d (Loeppky, Sacks, and Welch, 2009). The algorithm works by splitting each parameter's range into $10 \times d$ segments and selecting a random value from within each segment. Each parameter's values are randomly matched with the other parameter's values without overlapping segments. Figure 2.1 shows that if one dimension collapses each simulation point is still giving information about the remaining dimensions.

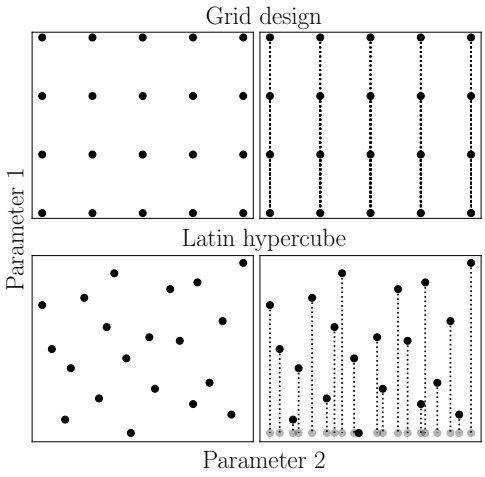

Figure 2.1: Examples of two space-filling designs and how they collapse down into lower dimensions. The grid design appears to fill the 2-dimensional space well, but when the second input becomes much less important than the first, design points are replicated. With the Latin hypercube design, all the design points are valuable and give new information, even if it collapses to one dimension.

The statistical emulation method used in this work is Gaussian process emulation. It is a Bayesian statistical approach that generates a mapping between a multi-dimensional input space (the parameter values) and an output of interest (O'Hagan, 2006). It requires a set of training data consisting of the perturbed parameter values and the corresponding output data. The approach is initiated with a prior Gaussian specification for the mapping, which is updated using information from the training data to produce a posterior specification. This is the emulator and it is a surrogate model which approximates the function between the perturbed parameters and the output of interest. The emulator is a continuous function that can be used to predict the model's output for any new combination of parameter values at a considerably reduced computational cost over running the cloud model itself.

Mathematically, from Johnson et al. (2015), for d uncertain input parameters $X = X_1, X_2, ..., X_d$ is the set of input parameters that make up a d-dimensional parameter uncertainty space. Then for a model output of interest Y, there is some relationship in the model, $g(\cdot)$, for which $Y = g(X)$. Gaussian process emulation is used to construct an approximation of the function $g(\cdot)$ so that Y can be predicted. The Gaussian process is made up of a mean function and a covariance structure. Letting $x = x_1, x_2, ..., x_d$ be a given realisation of X, the prior representation of the model behaviour is given by,

$$g(x) \sim GP[m(x), V(x, x')], \tag{2.5}$$

where $m(x)$ is the mean function and $V(x, x')$ is the covariance structure. These are

chosen to incorporate any prior knowledge of the model. Here, we have used a linear mean function and the Matérn covariance structure. The Matérn covariance structure has been found to work well for cloud models where the outputs may be nonlinear. The covariance structure provides an approximation of the uncertainty surrounding each mean output value, assuming a Gaussian error structure. All emulation processes were calculated using the "km" function of the DiceKriging package (Roustant, Ginsbourger, and Deville, 2012) in R (R Core Team, 2018).

In the first case study in Chapter 3, we create a 2-dimensional PPE made up of 20 simulations. We also generate a separate set of 8 simulations to use as validation data, to check the emulator's predictions against the actual model values. In the second case study in Chapter 4, we create a 6-dimensional PPE initially made up of 84 simulations (60 for training and 24 for validation), however, this is augmented with a further 12 simulations.

2.2.1 Sensitivity analysis

The Gaussian process emulators are used for variance-based sensitivity analysis to apportion the variation in the output of interest to the different perturbed parameters (Saltelli, Tarantola, and Chan, 1999). This analysis quantifies the contributions from each parameter in terms of the percentage of the output's variance.

The variance-based sensitivity analysis (Saltelli, Chan, and Scott, 2000) used here is the Fourier Amplitude Sensitivity Test (FAST) from the R package "sensitivity" (fast99 method) (Saltelli, Tarantola, and Chan, 1999; Iooss, Janon, and Pujol, 2023). This method assumes that the expected value of the model output can be represented as a linear combination of sine and cosine functions of varying frequencies. Using the properties of Fourier series, an approximation of the variance in the model output can then be estimated using a set of Fourier coefficients. A transformation function is evaluated at many different phases and frequencies (which relate to parameter values, we use 1000 combinations) to understand sensitivity to the parameters across phase space and compute the Fourier coefficients for each parameter.

The Fourier coefficients can be used to calculate sensitivity indices that quantify the contributions from each parameter, or from combinations of parameters, to the variance in model output (Saltelli, Chan, and Scott, 2000). The first-order index is calculated from a specific frequency and its higher harmonics and this defines the "main effect", which is the variance due to the individual effect of a parameter. The higher-order indices are calculated from a different set of frequencies which contain information about the residual variance that is not accounted for in the first-order indices, this defines the "total effect", which is the variance due to each parameter plus interactions with other parameters. In Chapter 3, the sensitivity analysis was robust to different

emulator builds. However, in Chapter 5 the values of each contribution were slightly variable depending on the exact emulator build. We created 100 emulator builds for each transition property and did the sensitivity analysis on each build to average the results. Replicating the analysis in this way gives us much greater confidence in the results presented.

Chapter 3

Visualisation of the deterministic response of stratocumulus cloud properties to free-tropospheric controls using statistical emulation

3.1 Abstract

Large uncertainties persist in modelling shallow, low clouds because there are many interacting nonlinear processes and multiple cloud-controlling environmental factors. In addition, under some conditions, a sharp change in behaviour can occur. Model studies that follow a traditional approach of exploring one factor at a time are unable to fully capture the relationships between the interacting factors and the simulated cloud properties. Here, we simulate a stratocumulus cloud based on the observations of the Second Dynamics and Chemistry of Marine Stratocumulus field study using a large-eddy simulation model coupled with a two-moment cloud microphysics scheme. Gaussian process emulation is used to visualise and assess the relationships between two cloud-controlling factors and the simulated cloud properties. Only 29 model simulations were required to build the emulators, which then enabled predictions of mean cloud properties to be made at thousands of combinations of the two factors within the ranges sampled by the simulations. The emulator predictions form a response surface that can be used to visually inspect the relationship between the cloud-controlling factors and any mean model output. Response surfaces of cloud liquid water path and cloud fraction show two cloud behavioural regimes of thin and patchy yet steady stratocumulus and

thick, growing stratocumulus with cloud fraction near 1. A particular focus of this study is to explore how to incorporate natural cloud variability (initial condition uncertainty) into the emulators, and how it affects interpretation of the cloud response surfaces. Failure to account for the variability creates unrealistic "bumpy" response surfaces. We show that it is possible to characterise the variability by measuring the scatter of a small number of initial-condition ensemble simulations around the emulated surface, thereby allowing a smoother, deterministic response surface to be constructed. Accounting for variability leads to the firm conclusion that there is a smooth but steep change in cloud behaviour between cloud regimes, but not a sharp transition.

3.2 Introduction

Shallow, low clouds cover a larger area of the Earth than any other cloud type, with stratocumulus clouds alone covering one-fifth of the surface. They increase Earth's albedo in most regions because they reflect more solar radiation than the underlying surfaces (Wood, 2012), while having only a small effect on emission of terrestrial radiation. Therefore, globally, they have a net cooling effect (Hartmann, Ockert-Bell, and Michelsen, 1992). These clouds are important for the global radiation budget and how it changes over time in response to warming (cloud feedback: Ceppi et al., 2017; Schneider, Kaul, and Pressel, 2019; Bretherton, 2015; Shen et al., 2022) and changes in aerosols (radiative forcing: Bellouin et al., 2020; Smith et al., 2020; Douglas and L'Ecuyer, 2020; Malavelle et al., 2017). However, the responses of shallow, low clouds to changes in aerosols and the thermodynamic environment (cloud-controlling factors) are very uncertain (Myhre et al., 2013). Consequently, the behaviour of shallow, low clouds in a warming climate and the corresponding feedbacks are not well understood (Bony and Dufresne, 2005; Zhang et al., 2013; Blossey et al., 2016; Nuijens and Siebesma, 2019), and this significantly contributes to the uncertainties that persist in climate change projections (Dufresne and Bony, 2008). It is crucial that we efficiently use the modelling tools available to narrow this uncertainty in the outcomes of perturbations and climate feedbacks.

Much of the uncertainty in simulating clouds comes from the large number of interacting cloud-controlling factors. Key factors that affect the state and evolution of shallow clouds are local meteorology, large-scale forcings, radiative feedbacks and aerosols. Some of these factors, such as thermodynamic properties, can change on short timescales (hours) and these shallow clouds respond quickly because internal changes in cloud microphysics and precipitation work on similar timescales. Such cloud-controlling factors can have a dramatic effect on cloud properties, such as the rapid change from closed- to open-cell cloud structures (Stechmann and Hottovy, 2016). Other factors, such as large-scale divergence, work on longer timescales and it can take 2 to 5 days for the cloud to adjust (Bellon and Stevens, 2013). Many of these factors covary and

have joint effects on cloud processes, some of which may counteract others creating a "buffered system" (Stevens and Feingold, 2009). In such a complex, interacting system, changing one factor at a time in the traditional testing of cloud responses to various drivers cannot capture the joint effects and interactions of the processes that make up these systems.

Extensive simulations of cloudy boundary layers with high-resolution cloud models (Stevens et al., 1998; Stevens, 2000; Stevens et al., 2001; Ackerman et al., 2004; Feingold, Jiang, and Harrington, 2005; Bretherton, Blossey, and Uchida, 2007; Hill, Feingold, and Jiang, 2009; Jones, Bretherton, and Blossey, 2014; Yamaguchi and Feingold, 2015; Kazil, Yamaguchi, and Feingold, 2017; Wyant et al., 2022) and model intercomparison projects (Moeng et al., 1996; Bretherton et al., 1999a; Pier Siebesma et al., 2003; Stevens et al., 2005a; Ackerman et al., 2009; Teixeira et al., 2011) have greatly advanced our understanding of cloud processes and highlighted areas of uncertain knowledge. Much of this valuable work was carried out under the Global Energy and Water Experiment Cloud System Study (GCSS) to assess and improve the realism of parameterisations in large-scale models (GEWEX Cloud System Science Team, 1993). By simulating the same case study with different models, it is possible to identify consistent deviations from observations and to explore why particular models capture observed cloud properties better than others. Here we take a different approach and explore the combined effect of cloud-controlling factors in one model.

Our study has a similar focus to Dal Gesso et al. (2015), a model intercomparison that explored how stratocumulus cloud properties depend on two cloud-controlling factors (henceforth, used interchangeable with "parameters"): the temperature and humidity differences between the surface and the free troposphere. The initial profiles of these factors were perturbed over a range of values at discrete Cartesian grid points across the 2-dimensional parameter space to study the effect on model outputs such as cloud cover and liquid water content. This array of discrete model outputs across the parameter space allowed the model response to be gauged. However, generally this grid-point method restricts the information available due to computational limitations, and the number of simulations required to explore n factors also rises with the power of n. Additionally, as shown in Feingold et al. (2016), such a design of simulations may misrepresent the joint effects of factors. Crucially, here we perturb both factors simultaneously because these factors may interact with each other and this could be missed in one-at-a-time perturbations.

To overcome the limitations of one-at-a-time sensitivity testing and to understand the joint effects of factors, we can use Gaussian process emulation to generate "response surfaces" that describe how cloud properties respond to multiple cloud-controlling factors. Gaussian process emulation is a method of machine learning that approximates the relationship between a set of model input parameters and a model output (O'Hagan,

2006). Unlike many other machine learning methods, this requires only a relatively small number of well-designed model simulations as training data. The emulator function (the approximated relationship) can then be sampled effectively millions of times at a fraction of the computational cost of running the simulations. From this dense sampling, we can produce a response surface with an associated uncertainty at any point in the parameter space. The power of emulation is in the ability to study the joint parameter effects on the output of interest and also to visualise all combinations of parameters within their realistic ranges at comparatively low computational cost. In previous emulation work, the parameters were often related to uncertain processes in the model, but here the parameters are cloud-controlling factors.

Gaussian emulation has been widely applied in aerosol and aerosol-cloud science. Firstly, response surfaces are an effective tool for visualising the joint effects of the uncertain input parameters and an output of interest, such as in Marshall et al. (2019) and Marshall et al. (2021) for volcanic eruptions. Transformations from parameter space to state space (Glassmeier et al., 2019; Hoffmann et al., 2020) or selection of two or three key parameters at a time allow higher dimensions to be visualised (Lee et al., 2011). Secondly, variance-based sensitivity analysis is used to understand which parameters contribute most to the variance in the output of interest (Saltelli, Chan, and Scott, 2000; Johnson et al., 2015; Regayre et al., 2014; Regayre et al., 2015; Regayre et al., 2018; Lee et al., 2011; Lee et al., 2013). Thirdly, the uncertain parameter ranges can be constrained using observations of the model outputs (Johnson et al., 2018; Regayre et al., 2018; Regayre et al., 2020; Marshall et al., 2021), which can lead to constraint of additional outputs.

The first cloud emulation study was Johnson et al. (2015), where they perturbed initial aerosol concentrations and nine microphysical model parameters in a deep convective cloud. Sensitivity analysis showed that all the cloud properties considered were most sensitive to aerosol concentrations and the collection efficiency of droplets by graupel. This demonstrated the insight that can be gained from emulating cloud models, where buffering in clouds can obscure relationships between input parameters and cloud responses. Perturbing multiple input parameters together reveals how they jointly affect an output and under what conditions certain parameters have a larger effect. Following this work, emulation has been used for sensitivity analyses to initial meteorological conditions in deep convective clouds and hail (Wellmann et al., 2018; Wellmann et al., 2020) and in sea breeze convection (Igel, van den Heever, and Johnson, 2018; Park et al., 2020). Additionally, Glassmeier et al. (2019) and Hoffmann et al. (2020) have used emulation of state variables to explore cloud-process understanding in stratocumulus. Here we consider the joint effects of initial meteorological conditions in stratocumulus for the first time and we identify regimes of cloud behaviour in parameter space, as in Johnson et al. (2015) and Park et al. (2020).

Shallow clouds may have sharp changes in behaviour (a steep gradient in the output) between regimes, which can make emulation challenging. Feingold et al. (2016) found a steep gradient in a study of nocturnal marine stratocumulus clouds in which six parameters were perturbed. This dataset was used in Pope et al. (2021) for non-stationary emulation, where Voronoi tessellations were used to define regions of the 6-dimensional parameter space where they could apply separate, stationary emulators, with an assumption of smoothness. The aerosol concentration was found to be the main parameter controlling the discontinuity, but the high dimensionality of the parameter space made visualising the discontinuity difficult. Here, we have visualised a steep gradient in two dimensions and used adaptive sampling to explore it, but we found that it emulates reasonably so non-stationary methods were not necessary here.

Another challenge in visualising cloud behaviour as a response surface is that cloud models exhibit a high degree of natural variability, which may obscure the deterministic behaviour that an emulator is designed to represent. In a purely deterministic model, the emulator function can interpolate exactly through all the training data. However, because clouds are quasi-stochastic, the simulated cloud properties at each point in parameter space also depend on the initial conditions. Such variability (or noise) is normally averaged out by running initial-condition ensembles and then using the ensemble mean as the training data at each point in parameter space (Johnson, Gosling, and Kennedy, 2011; Oyebamiji et al., 2017; Henderson et al., 2009). For global climate models, which are resource intensive, this variability is usually estimated using maximum likelihood methods (Williamson and Blaker, 2014; Pope et al., 2021), although in reality the variability is often chosen to be very small to have minimal effect on the predicted function. Here, we show the natural variability of our cloud model can be approximated based on a small number of initial-condition ensembles.

In this study, we assess the ability of statistical emulation to capture the transition between two regimes of shallow cloud behaviour as initial profiles of 2 parameters are varied. We also explore a method to quantify natural variability and account for it during construction of the emulator. We start from a homogeneous stratocumulus-topped boundary layer that has steady cloud properties despite lying in a region of parameter space that is prone to breaking up, as hypothesised by Lilly (1968), Randall (1980) and Deardorff (1980). Two parameters are perturbed to identify where cloud breakup occurs across the parameter space. We will answer the following questions. First, does the hypothetical cloud-breakup threshold separate two cloud regimes? Second, how well can we characterise the change in cloud behaviour using statistical emulation? Is there a discontinuity or a smooth change? Third, how can we account for the model's natural variability in the emulators so that the response surfaces represent deterministic cloud behaviour rather than noise?

The remainder of this paper is laid out as follows. Section 3.3 gives context to the

cloud-breakup region and section 3.4 describes the model simulation setup, the initial simulation and the parameter perturbations. Section 3.5 discusses the cloud behaviour displayed across the perturbed parameter ensemble and exploring the model's behaviour around the cloud-breakup threshold. The model's natural variability will be quantified and included in the emulation method in section 3.6. The results are discussed further in section 3.7 and conclusions are given in section 3.8.

3.3 Theoretical context

The stratocumulus simulations are based on the conditions observed in the first research flight (RF01) of the Second Dynamics and Chemistry of Marine Stratocumulus field study (DYCOMS-II) (Stevens et al., 2003). The campaign took place off the west coast of California in July 2001. Flight RF01 observed a homogeneous, non-drizzling stratocumulus cloud deck over nine hours through the night. Dropsonde data measured a well-mixed boundary layer above the sea surface at 850 m, meaning that temperature and moisture profiles were nearly constant to this depth. Over the flight time, the boundary layer and cloud depth deepened by 50 m, resulting in a 250 m thick cloud. The well-mixed stratocumulus-topped boundary layer was capped by a temperature inversion, where the potential temperature, θ, increased by 8.5 K and the total water mass mixing ratio, q_t, decreased by 7.5 g kg^{-1} within a few tens of metres of cloud top.

Stevens et al. (2005a) conducted a large-eddy simulation (LES) model intercomparison study based on RF01 to compare ten models, including the Met Office large-eddy model, which is an earlier version of the model we use here. A few models simulated a cloud like the one observed, but the majority simulated a more broken cloud with lower cloud fraction and lower liquid water path (the vertically integrated liquid water content). Most models simulated a deepening boundary layer, a thinning cloud and a rising cloud base, but some simulated a decoupling of the boundary layer, which was not observed. A decoupled boundary layer is no longer well-mixed and tends to decrease the cloud water content because the cloud layer is cut off from the ocean's moisture supply. The differences between the models were mostly attributed to the different resolutions and mixing schemes used, but the temperature and humidity change across the inversion made the simulations particularly sensitive to a cloud-dissipating mechanism that we discuss here. Other LES studies that have simulated DYCOMS-II RF01 generally fall within the multi-model range of the intercomparison study (Yamaguchi and Randall, 2008; Xiao, Wu, and Mechoso, 2011; Ghonima et al., 2015; Pressel et al., 2017).

The stratocumulus-topped marine boundary layer can persist as a uniform cloud field for days before breaking up (sometimes entirely) within a couple of hours. The mechanism behind this rapid change was originally proposed by Lilly (1968) based on

a simplified theoretical model. For specific combinations of temperature and humidity at the inversion, the mixing of warm, dry air into the cloud from above (entrainment) leads to evaporative cooling and enhanced mixing, creating a positive feedback that can rapidly dissipate the cloud. However, as with DYCOMS-II, many observations and LES studies have found stratocumulus clouds persisting within this region of temperature-humidity parameter space (Kuo and Schubert, 1988; Siems et al., 1990; Moeng, 2000; Stevens et al., 2005a). Mellado (2017) summarised recent studies that found that the feedback is generally not strong enough under realistic conditions to dissipate marine stratocumulus clouds, especially alongside other confounding factors.

Randall (1980) and Deardorff (1980) derived an inversion instability parameter, κ, with a threshold beyond which the cloud-dissipating feedback occurs,

$$\kappa = 1 + \frac{c_p}{L_\mathrm{v}} \frac{\Delta\theta_\mathrm{l}}{\Delta q_\mathrm{t}}, \tag{3.1}$$

where c_p is the specific heat of air, L_v is the latent heat of vaporisation, $\Delta\theta_\mathrm{l}$ is the change in potential temperature for liquid water at the inversion, and Δq_t is the change in total water mass mixing ratio at the inversion. Several studies since have made alternative derivations and attempted to map out the dependence of κ on these two parameters, $\Delta\theta_\mathrm{l}$ and Δq_t, using one-at-a-time model sensitivity simulations (Kuo and Schubert, 1988; MacVean and Mason, 1990; Siems et al., 1990; Yamaguchi and Randall, 2008; Xiao, Wu, and Mechoso, 2011; van der Dussen, de Roode, and Siebesma, 2014; Dal Gesso et al., 2015).

Here we simulate DYCOMS-II RF01 and perturb $\Delta\theta$ and Δq_t across a range of values to fully explore the parameter space and map out the cloud behaviour in terms of breakup or growth.

3.4 Experiment design

3.4.1 Model Description

The LES cloud model used here is the UK Met Office/Natural Environment Research Council (NERC) Cloud (MONC) model (Brown et al., 2020). We ran a nocturnal simulation and used a parameterisation to calculate longwave cooling rates at cloud top and base from liquid water content using an exponential decay function (Bretherton et al., 1999a). The horizontal resolution was 30 m and the vertical resolution varied between 7.5 m around the inversion and 10 to 20 m elsewhere in the boundary layer. The domain size was 250 by 250 grid boxes with 110 layers vertically up to 1500 m. The subgrid mixing scheme for unresolved turbulence, diffusion and viscosity is an extension of the Smagorinsky-Lilly model (detailed in Brown, Derbyshire, and Mason, 1994).

The microphysics scheme used is the Cloud AeroSol Interacting Microphysics (CASIM) model, which is a bulk scheme that can use up to three moments for each hydrometeor (Shipway and Hill, 2012; Hill, Shipway, and Boutle, 2015; Dearden et al., 2018; Field et al., 2023). Here CASIM defines cloud liquid and rain droplets by two moments: number concentration and mass mixing ratio.

We used fixed cloud droplet number concentrations. The results shown in the main body of this study used cloud droplet number concentration equal to 50 cm^{-3}, but cloud droplet number concentration equal to 150 cm^{-3} was investigated separately and the results are included in Appendix A.1. Condensation and evaporation were calculated by a saturation adjustment scheme, where any surplus water vapour in the cloud condenses onto the fixed number of cloud droplets and any deficit evaporates from the droplets, keeping the relative humidity within the cloud at 100%. Cloud droplets can be autoconverted and collected into rain droplets, and rain droplets can precipitate and either reach the surface or evaporate in sub-saturated air below the cloud base. Condensation of water vapour onto rain cannot occur due to the saturation adjustment scheme, as in the old LEM (Gray et al., 2001). Sedimentation was switched on for both cloud droplets and rain, which advects water mass downwards through the boundary layer. Autoconversion and collection are dependent on cloud water mass mixing ratio, rain water mass mixing ratio and droplet number concentration (Khairoutdinov and Kogan, 2000). Mixing of new air from above the cloud into the cloud layer is homogeneous mixing, that is new air is mixed in with the cloudy air before the evaporation calculation takes place so all droplets are evaporated equally until saturation is reached. This means that there is a reduction in cloud droplet radius, but cloud droplet number is not affected.

3.4.2 Perturbed parameter ensemble

A base case simulation was initialised to match the DYCOMS-II RF01 setup in Stevens et al. (2005a). The simulation was run for eight hours nocturnally with initial surface sensible and latent heat fluxes of 15 W m^{-2} and 115 W m^{-2}. The initial profiles of θ and q_t are shown in Figure 3.1.

We perturbed $\Delta\theta$ and Δq_t to explore the joint effect of these two parameters, creating a perturbed parameter ensemble (PPE) in the 2-dimensional parameter space (Figure 3.1). The initial profiles were kept the same up to the inversion at 840 m, where the jump size was varied for both. The ranges for these parameters were chosen based on the ranges outlined in van der Dussen, de Roode, and Siebesma (2014):

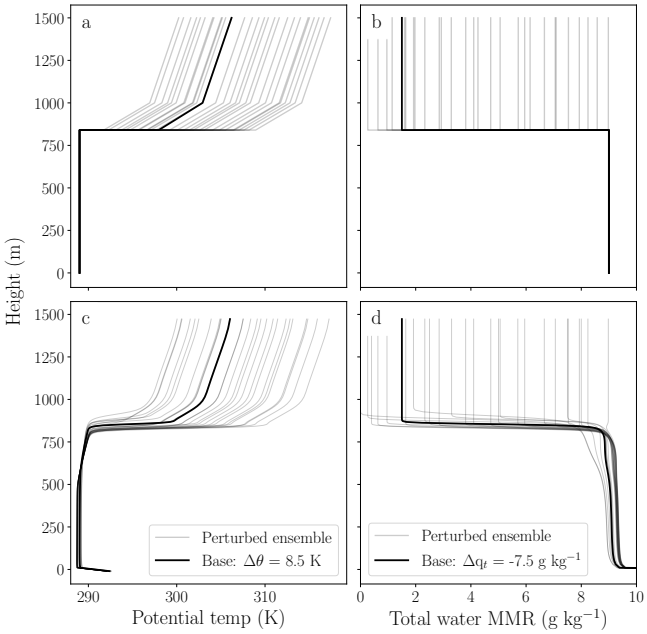

Figure 3.1: The initial profiles for all simulations. The model configuration profiles for a) potential temperature and b) total water mass-mixing ratio. The profiles after model spin up has completed for c) potential temperature and d) total water mass-mixing ratio. The solid lines show the base simulation values taken from the DYCOMS-II observational campaign, research flight RF01, while the grey lines show the profiles for the ensemble members perturbed from the base simulation.

$$2\ K \leq \quad \Delta\theta \quad \leq 20\ K \tag{3.2}$$

$$-9\ g\ kg^{-1} \leq \quad \Delta q_t \quad \leq 0\ g\ kg^{-1}. \tag{3.3}$$

Theoretically, cloud thickening occurs for conditions below the κ threshold which is in the region of parameter space where $\Delta\theta \rightarrow$ 20 K and $\Delta q_t \rightarrow$ 0 g kg^{-1}. Cloud thinning occurs above the κ threshold where $\Delta\theta \rightarrow$ 2 K and $\Delta q_t \rightarrow$ -9 g kg^{-1}. For a cloud fraction$\approx$1, cloud thickening is roughly analogous to an increasing liquid water path throughout the simulation - a positive liquid water path tendency.

The PPE simulation data were used as training data for statistical emulation (described below). The combinations of values of $\Delta\theta$ and Δq_t were defined using a "maximin" Latin hypercube algorithm comprised of 20 simulations, which has been shown to be sufficient to create an emulator over a two-dimensional parameter space (Morris and Mitchell, 1995; Loeppky, Sacks, and Welch, 2009; Lee et al., 2011). The Latin hypercube (Figure 3.2) is a space-filling design that samples the parameter space efficiently to provide as much information as possible about the model to an emulator. In comparison, regular grid (Cartesian) designs are an inefficient way of sampling a

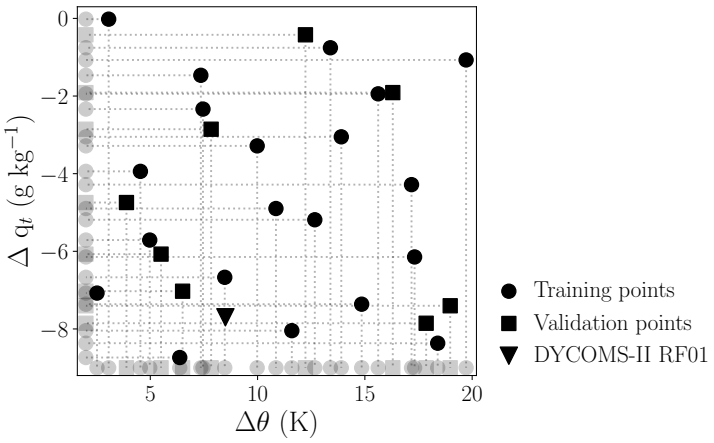

Figure 3.2: The Latin hypercube design for the PPE. The solid circle markers are training points and the solid square markers are validation points. The faded markers show the distribution along each dimension. The triangle marker is the base simulation based on DYCOMS-II RF01.

high-dimensional space. This becomes crucial if the sensitivity to some parameter perturbations is greater than for others. When this type of design is projected to lower dimensions, as in Figure 3.2, design points are not replicated.

3.4.3 Gaussian process emulation

Gaussian process emulation is a Bayesian statistical approach that generates a mapping between a multi-dimensional input space (the parameters) and an output of interest (O'Hagan, 2006). This mapping is used to predict the model's output for many thousands of parameter input combinations at a considerably reduced computational cost. It requires a set of training data, consisting of the input settings and corresponding output data from multiple model simulations over the perturbed parameter ranges. Under the Bayesian paradigm, the approach is initiated with a prior Gaussian process specification for this mapping, which encapsulates any prior knowledge about the model output. The prior is updated using the training data to create a better estimation of the function representing the model output response (also of Gaussian form) to the perturbed inputs. This better estimation is a posterior Gaussian process specification, and is our emulator. The emulator enables the model response to the inputs to be thoroughly sampled to produce a response surface at a significantly cheaper computational cost than via running the cloud model itself. The uncertainty surrounding each emulator-predicted output value is also calculated, assuming a Gaussian error structure and based on how close a point is to the training data. A second smaller set of simulations is used to validate the emulator to ensure that it is producing a reasonable representation of the model's behaviour. The emulation in this work has been conducted in R using the DiceKriging package (R Core Team, 2018; Roustant, Ginsbourger, and Deville, 2012).

3.4.4 Joint effects of parameters

The response surfaces created in this chapter and in Chapter 5 allow us to visualise the joint effects between parameters on the output of interest. The terminology that we use for this is illustrated in Figure 3.3. A parameter (factor) may have a linear or a nonlinear effect on the output. A linear joint effect of two parameters is when their effects are additive in their impact on the output, we also refer to this as a "combined effect". These two parameters may be linear or nonlinear, but their joint effect is linear if the relationship of each parameter and the output does not vary with the second parameter. A nonlinear joint effect is indicated on a 2-dimensional response surface by curvature, which shows that how the output depends on one parameter varies with the other parameter. We also refer to this as an "interaction", since some process relating to the second parameter must be occurring to dampen or amplify the effect of the first parameter. Later when we consider how the variance of each parameter contributes to the variance in the output, the individual effects sum up to exactly account for the variance in the output in a linear joint effect. However in nonlinear joint effects, the sum might not exactly account for the variance in the output, i.e., there may be some residual variance that is unexplained. In this case, the variance in the interactions between parameters also contributes to the variance in the output.

3.5 Results

We will focus on the response of in-cloud liquid water path and cloud fraction to the perturbations. The cloud fraction is the fraction of columns with liquid water content greater than 0.01 g m^{-3}. The output values (training data) for liquid water path and cloud fraction are taken as the mean over the final two hours of the simulation. The tendencies of both are the rate of change over the course of the simulation after a spin-up period of two hours.

3.5.1 Base case simulation

The base case is shown in Figure 3.4, along with the rest of the ensemble. After spin up, the mean liquid water path, $L = 38$ g m^{-2} (dashed line in Figure 3.4a), which is in good agreement with the multi-model mean in Stevens et al. (2005a) of 40 g m^{-2}. The top-down liquid water path snapshots in Figure 3.4c (inset) show that the base simulation cloud initialises as homogeneous stratocumulus and the cells grow and thicken slightly over eight hours. The cloud base is around 600 m and cloud top is at the inversion at 840 m and these stay nearly constant during the simulation. The liquid water path gradually increases through the simulation up to 56 g m^{-2} in the final timestep, so the liquid water path tendency is 2.2 g m^{-2} hr^{-1}, whereas it is slightly negative in Stevens et al. (2005a). After spin-up, cloud fraction, $f_c = 0.87$ (dashed line in Figure 3.4c) and

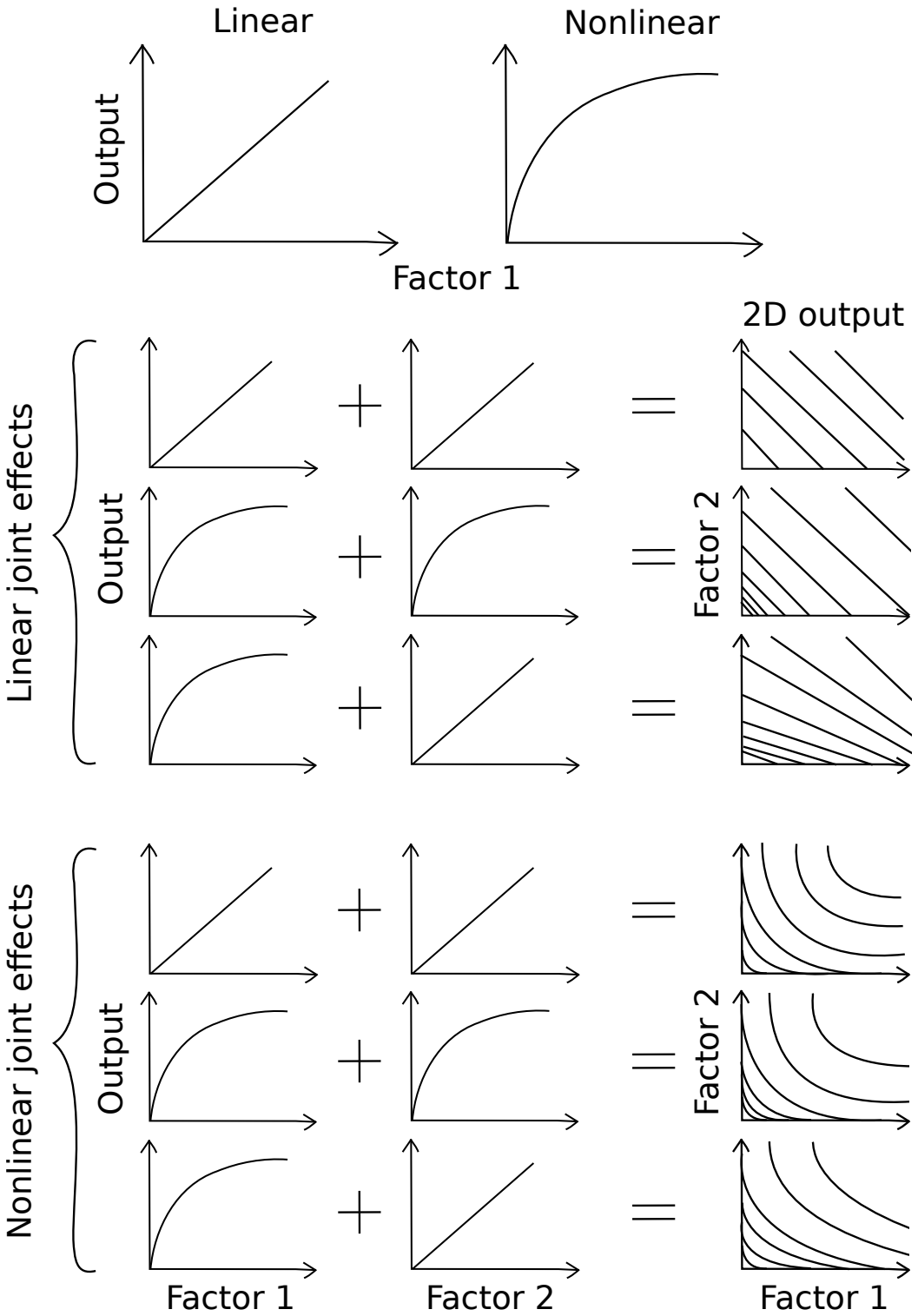

Figure 3.3: Definitions of joint effects. A factor may have a linear or nonlinear effect on an output. If any combination of factors (linear or nonlinear) have a joint effect where the variance in the output is explained entirely by their individual contributions it is a linear joint effect, or a combined effect. Where the contributions from a combination of factors does not entirely account for the variance in the output the factors have a nonlinear joint effect, or an interaction.

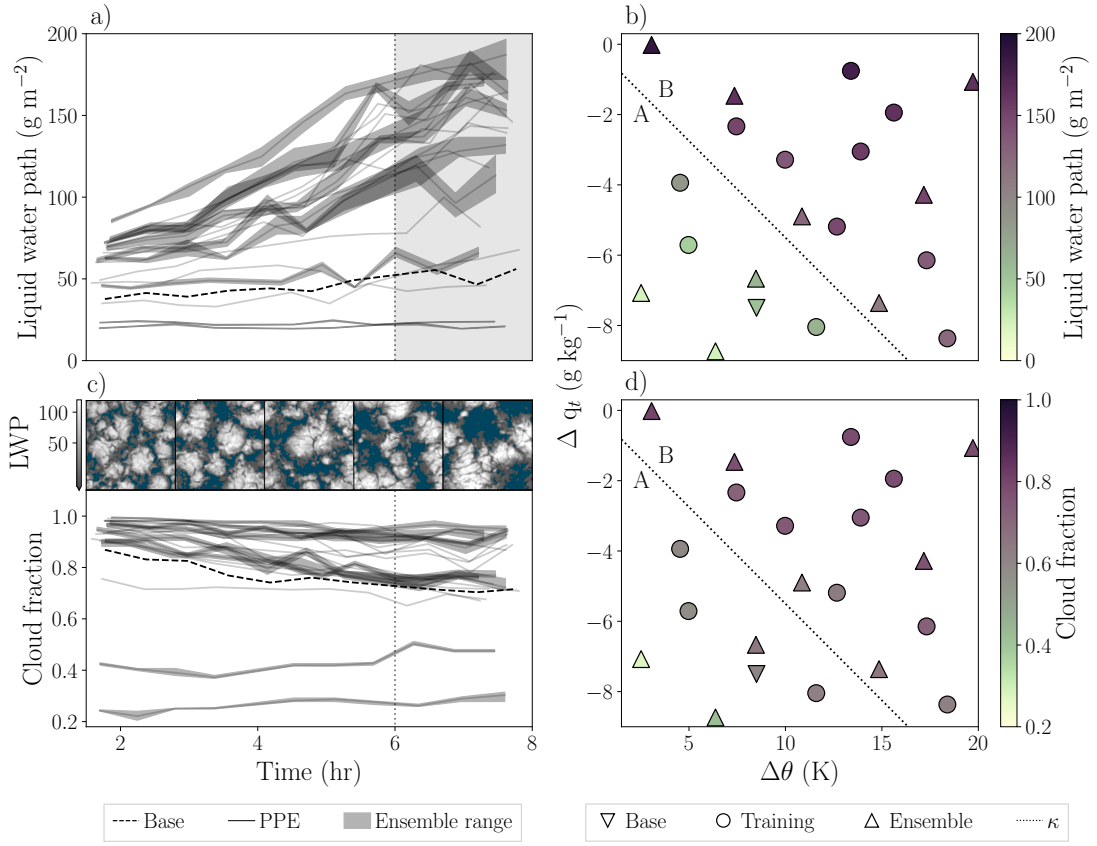

Figure 3.4: Liquid water path and cloud fraction model output for the whole ensemble. a) Liquid water path and c) cloud fraction timeseries post-spinup to the end of the simulation. The last two hours (shaded area) are taken as an average for the training data. The base simulation is shown by the darker line and the point-ensemble simulations show the range of the ensemble as an envelope. The inset in c shows top-down snapshots of the liquid water path for the base simulation. b) Liquid water path and d) cloud fraction training data values plotted in parameter space, $\Delta\theta$ vs Δq_t. The κ line is the theoretical threshold for the κ parameter described in section 3.3, which splits the regions into A and B (see section 3.5.3).

this decreases to 0.72 over the course of the simulation giving a cloud fraction tendency of -0.02 hr^{-1}. The initial cloud fraction is in the lowest quartile of the multi-model range in Stevens et al. (2005a). The ensemble mean cloud fraction begins near 1 and decreases to approximately 0.8, with the majority following similar behaviour, but a small number of models simulated a decrease to around 0.2.

3.5.2 Perturbed cloud behaviour

The timeseries of liquid water path and cloud fraction in Figures 3.4a and c show the spread across the PPE. Two simulations do not spin up any substantial stratocumulus, with $L < 25$ g m^{-2} and $f_c < 0.5$ throughout the simulation. Four simulations spin up a very thin stratocumulus with $25 < L < 50$ g m^{-2} and initial $f_c > 0.7$. These clouds thicken slightly through the simulation with liquid water path values increasing up to

65 g m^{-2} and cloud fraction decreasing by 0.1-0.2 as the cloud water aggregates. This set of simulations make up all but one of the data in the region marked A in parameter space, above the κ parameter threshold. For the simulations in region B, plus the point at coordinates $\Delta\theta$ = 5 K and Δq_t = -4 g kg^{-1}, the liquid water path timeseries spins up in the range of 50 to 80 g m^{-2} and increases by 30 to 120 g m^{-2}. These clouds all have initial stratocumulus with $f_c > 0.9$ and most remain in that region or decrease to 0.8.

The mean liquid water path over the last two hours of the simulation is shown in Figure 3.4b. For a low $\Delta\theta$ (a weak temperature inversion) mean liquid water path is generally low, down to about 21 g m^{-2} at $\Delta\theta$ = 2.5 K. With a stronger inversion, liquid water path also generally increases up to about 160 g m^{-2} at $\Delta\theta$ = 20 K. For a high Δq_t (a moist free troposphere) the liquid water path is high, up to 185 g m^{-2} for Δq_t = 0 g kg^{-1}. With a reduction in free-tropospheric humidity, liquid water path generally decreases down to about 20 g m^{-2} for Δq_t = -8.7 g kg^{-1}. The two parameters have a combined effect such that liquid water path is lowest for weak inversions with a dry free troposphere and highest for strong inversions with humidity similar to the boundary layer.

The mean cloud fraction over the last two hours of the simulation is shown in Figure 3.4d. For low $\Delta\theta$ cloud fraction is generally low, down to about 0.3 at $\Delta\theta$ = 2.5 K. As the inversion gets stronger, cloud fraction generally increases up to 0.9 at $\Delta\theta$ = 20 K. For a free troposphere that is as moist as the boundary layer, cloud fraction approaches 1 for Δq_t = 0 g kg^{-1}. As the free troposphere gets drier, cloud fraction generally decreases down to about 0.5 for Δq_t = -8.7 g kg^{-1}. As with liquid water path, the two parameters have a combined effect such that cloud fraction is lowest for weak inversions with a dry free troposphere and highest for strong inversions with humidity similar to the boundary layer.

The spatial distribution of liquid water path is shown in Figure 3.5 for the last timestep in each simulation. These are arranged approximately in order of the location in parameter space. The two simulations that do not form stratocumulus can be seen to the lower left of the figure as small cumulus clouds. Moving towards higher Δq_t and $\Delta\theta$, the plots show stratocumulus with a higher cloud fraction than the cumulus, and at the top and right of the figure in particular, this becomes quite thick.

None of the simulations are drizzling significantly, but all the simulations in region A, except the point at $\Delta\theta$ = 5 K and Δq_t = -4 g kg^{-1} previously picked out, drizzle two to three orders of magnitude less than those in region B (see Appendix A.2).

In summary, the PPE simulations show that cloud behaviour across parameter space falls into two behavioural regimes that roughly aligns with the theoretical κ parameter threshold. Above the κ threshold, in region A, the simulations generally spin up to

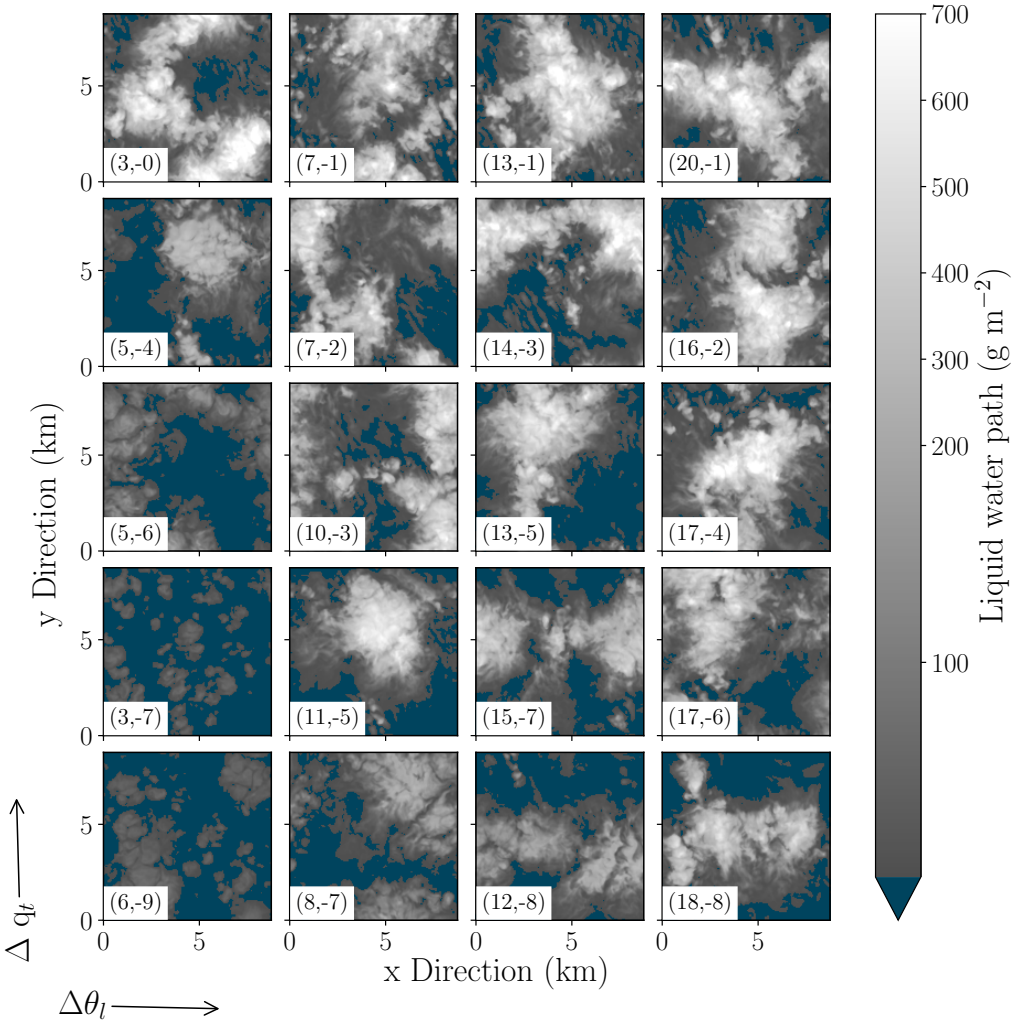

Figure 3.5: Top-down views of liquid water path for each of the 20 training simulations in the last time step. Plots are ordered approximately by location in parameter space. The dark blue shows the areas with liquid cloud droplet mass mixing ratio < 0.01 g kg^{-1} at all levels.

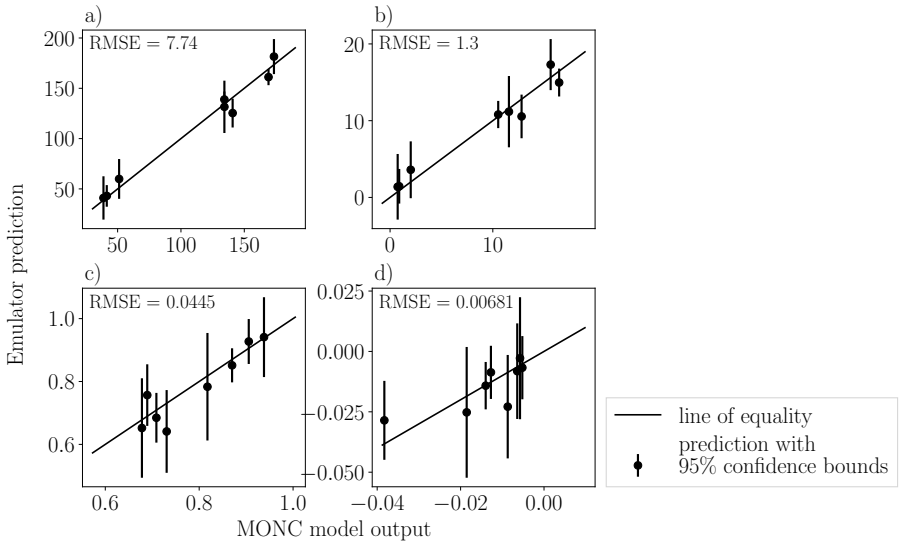

Figure 3.6: Validation plots for the four cloud property emulators (response surfaces in Figure 3.7). a) liquid water path (g m^{-2}), b) liquid water path tendency (g m^{-2} hr^{-1}), c) cloud fraction and d) cloud fraction tendency (hr^{-1}). The MONC output values for each point are on the x axis and the emulator predicted values are on the y axis. The black line shows the line of equality and the error bars indicate the 95% confidence bounds on the emulator mean predictions.

very thin stratocumulus cloud or just small cumulus, that show little to no growth throughout the simulation. Below the κ threshold, in region B, the simulations spin up to stratocumulus cloud with a high cloud fraction and a medium liquid water path that increases throughout the simulation. Simulations in region B have two to three orders of magnitude more drizzle than those in region A. There is one point in region A at $\Delta\theta$ = 5 K and Δq_t = -4 g kg^{-1} that behaves more like the simulations in region B.

3.5.3 Response surface analysis

We used the set of simulations to build Gaussian process emulators of liquid water path, cloud fraction, liquid water path tendency and cloud fraction tendency over the final two hours of the simulations. To validate the emulators, we used the eight validation simulations that were part of the Latin hypercube design, but not used to train the emulators. We compare the emulator predictions at those points of parameter space with the model output in Figure 3.6. For all the emulators, the model values are within the emulator prediction 95% uncertainty range. For the liquid water path and liquid water path tendency (Figure 3.6a and b) the predicted mean value is close to the line of equality, whereas the cloud fraction and cloud fraction tendency emulators have some predicted mean values that are quite far from the line of equality (Figure 3.6c and d), but the large uncertainty means the model value is still within the range. The liquid water path and cloud fraction uncertainty ranges cover around ±10% on average of the mean values, whereas the tendency ranges cover around ±100% on average. So

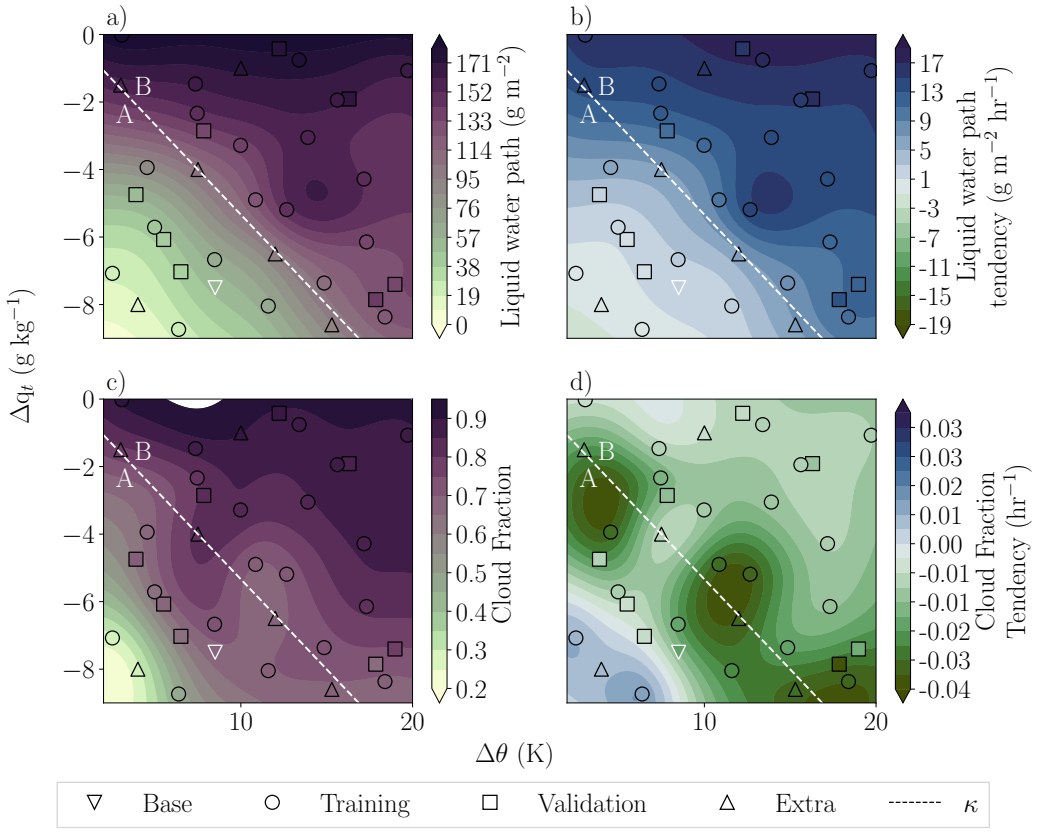

Figure 3.7: Response surfaces produced from emulator mean predictions. a) liquid water path, b) liquid water path tendency, c) cloud fraction and d) cloud fraction tendency. The base simulation is shown by the inverse white triangle, the training data by the black circles, the validation data by the black squares, and the extra simulation points by the black triangles. The dashed white line is the κ threshold, where equation (3.1) equals 0.23, and divides parameter space into region A and B.

although the ranges include the model values, the uncertainties can be quite large.

Emulator response surfaces for the mean liquid water path and cloud fraction over the last two hours, and their tendencies, are shown in Figure 3.7. Originally 20 simulations were run as training data for the emulators (black circles). However we ran six additional simulations to fill in the gaps near to the κ threshold and in regions of parameter space with more extreme model output values and here we show the 26-point training set. The RMSE values in the validation plots (Figure 3.6) show that the liquid water path and the cloud fraction tendency emulators are more confident with the additional points, and the other two emulators are marginally less confident. The general shapes across parameter space are not much different between the training sets.

The liquid water path response surface follows the behaviour described previously by the training data, with low liquid water path for low Δq_t, low $\Delta\theta$ (dry, cool free troposphere) and high liquid water path for high Δq_t, high $\Delta\theta$ (moist, warm free troposphere). But we can clearly see now that Δq_t has a larger effect on liquid water path, and for high Δq_t the liquid water path becomes invariant to $\Delta\theta$. We can also see a local maximum at $\Delta\theta$ = 15 K and Δq_t = -4.5 g kg^{-1}, which we will discuss in section 3.6. The liquid water path tendency follows a similar pattern to the liquid water path. Where the liquid water path is high, the tendency is most positive, i.e., there is most growth. Where the liquid water path is low, the tendency is very close to zero. It also follows the higher dependency on Δq_t and has a local maximum in a similar location. Additionally, the emulator predicts some slightly negative values in the corner of parameter space with low liquid water path, however the emulator has limited information and therefore large uncertainties at extremities.

The cloud fraction response surface also follows the behaviour described previously, with low cloud fraction for low Δq_t, low $\Delta\theta$ (dry, cool free troposphere) and high cloud fraction for high Δq_t, high $\Delta\theta$ (moist, warm free troposphere). As with the liquid water path, Δq_t has a larger effect than $\Delta\theta$, but it is not as stark as in the liquid water path. The cloud fraction tendency is mostly negative across the parameter space, with only a slightly positive region at low values of Δq_t and $\Delta\theta$. This is because there are only small cumulus clouds at start of the simulation (Figure 3.5) and these are mostly unchanging throughout the simulations, but increase in cloud cover slightly. Where cloud fraction is approximately 1, the cloud fraction tendency is close to zero and just slightly negative. The rest of the cloud fraction tendency surface is very uneven (noisy) since there are only small changes in cloud fraction throughout the simulations (Figure 3.4c). Some of the validation points (black squares) are close in value to the predicted surface, but a few points are quite contrasting.

Some of the response surfaces in Figure 3.7 suggest that there are nonlinear joint effects (interactions) between the parameters due to the slight curvature. The strength

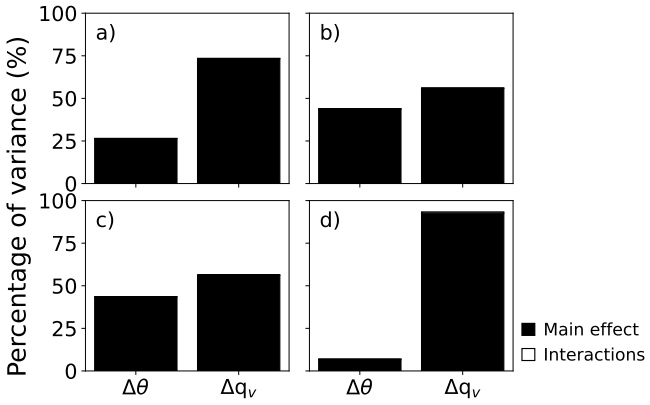

Figure 3.8: Sensitivity analysis for each emulator. a) liquid water path, b) liquid water path tendency, c) cloud fraction and d) cloud fraction tendency. Bars show the percentage contribution from each factor to the variance of the transition time. The black section shows the main effect, i.e. the individual parameter effect, and the white section shows the contribution from interactions with other parameters.

of the inversion will affect how much vapour is transported between the boundary layer and the free troposphere, which in turns affects the jump in specific humidity. Additionally, the specific humidity in the free troposphere affects the strength of longwave cooling, which can strengthen the inversion or weaken it.

Variance-based sensitivity analysis (described in Chapter 2.2.1) shows that Δq_t contributes the most to the variance in the output for all emulators (Figure 3.8), in particular for the mean liquid water path (a) and the cloud fraction tendency (d). This analysis also shows that the interactions between parameters do not contribute a significant amount to the variance in the outputs.

The κ threshold separating regions A and B approximately follows the contours on the liquid water path emulators, other than for the cloud fraction tendency (Figure 3.7d). The surfaces show a smooth gradient between these regions of parameter space, rather than a discontinuity. In the cloud behaviour analysis in section 3.5.2, there was a single point in region A at $\Delta\theta = 5$ K and Δq_t = -4 g kg^{-1} that did not fit with the rest in terms of behaviour. We can now see in liquid water path and liquid water path tendency that the contour lines curve round in this part of parameter space. If the κ function followed the contours at this point, it would be closer to splitting the parameter space by cloud behaviour into very thin stratocumulus cloud or small cumulus plumes, with little growth, in region A and stratocumulus cloud with a high cloud fraction and a medium liquid water path that grows throughout the simulation in region B.

3.6 Natural variability

Here we explore cloud natural variability and how to account for it when building emulators. Cloud properties are sensitive to any small variation in initial conditions, not just the parameter values we have discussed so far but also slight differences in turbulence structure. Each training data point represents only one possible cloud state for those particular parameter settings – i.e., it is effectively a random draw from an unquantified distribution representing natural variability. The effect of this variability is to create 'bumpiness' in the response surface as the emulator interpolates through each training point, instead of allowing for the range of possible values at that point (see Figure 3.9a). Additionally, in attempting to fit to the training data, the emulator may create additional extrema that are far from the training points and not based on the model's actual behaviour. An example of this is the maximum around $\Delta\theta = 15$ and Δq_t = -4.5 in Figure 3.7a. The bumps from training points and the additional extrema do not allow the emulator to accurately represent the deterministic cloud behaviour that we are aiming to capture with the response surface.

A much smoother response surface could be created by running an initial-condition ensemble at each point in parameter space and building an emulator of the ensemble mean (with the ensemble created by randomising the small temperature perturbations that are imposed at the beginning of each simulation, which initiate turbulence and cloud formation in the boundary layer). However, such an initial-condition ensemble would become very computationally expensive for a large number of parameters. Here, we therefore explore how we can use a small number of initial-condition ensembles to estimate natural variability and produce smooth, deterministic emulator surfaces by exploiting a hyperparameter within the emulator called a "nugget term".

In the posterior Gaussian process, the covariance function estimates the prediction uncertainty for any point dependent on that point's distance from the training data. In this study, the covariance between any two points is,

$$V(x_j, x_k) = \sigma^2 K(x_j, x_k), \tag{3.4}$$

where σ^2 is the variance of the Gaussian process and in this case $K(x_j, x_k)$ represents the Matérn class of covariance functions. These functions are stationary since the covariance of the two points depends only on the distance between them. The covariance function can be extended to include the nugget term, σ_N^2,

$$V(x_j, x_k) = \sigma^2 K(x_j, x_k) + \sigma_N^2 \delta_{j,k}, \tag{3.5}$$

where $\delta_{,,}$ is the Kronecker delta function, which is equal to 1 for $j = k$ and equal

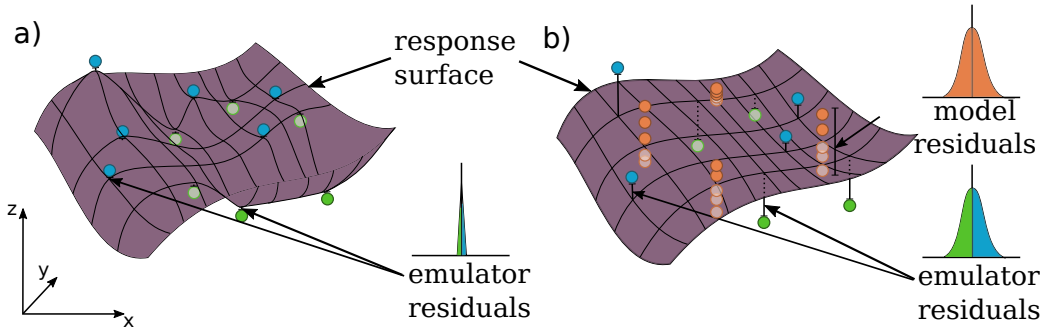

Figure 3.9: Diagram showing the effect of adding a nugget term on the smoothness of the response surface. a) The purple response surface interpolates exactly through the blue and green training points so the emulator residuals are zero. b) The response surface is smooth after a nugget term has been added, where the surface no longer interpolates exactly but through a prescribed buffer around the blue and green training points. Initial-condition model ensembles have been run at a selection of points (orange). The nugget term is appropriately large when the distribution of emulator residuals matches the distribution of model residuals.

to 0 otherwise. The nugget term is often included to alleviate numerical issues in deterministic models, although there are several other additional benefits for adding one (Andrianakis and Challenor, 2012; Gramacy and Lee, 2012). Notably, that a nugget term may help the posterior distribution to be less influenced by inaccuracies in the assumed prior functions. Practically, the nugget term is a variance that is added at each training point. From this variance, a new output value at the training point is predicted that is within the variability at this point, but no longer interpolated exactly.

We hypothesise that the variance represented by the nugget term should be equal to the variance representing natural variability for the response surface to more accurately represent the underlying deterministic behaviour. In Figure 3.9a, the emulator mean function interpolates through the blue and green training points, resulting in a bumpy response surface. In this exact interpolation, the "emulator" residual between the emulator mean function (the response surface) and any training point is zero. However, each of these points is just one in a distribution of possible values, which is shown by the orange initial-condition ensembles in Figure 3.9b. The aim, by adding a nugget term, is to create a smoother surface such that the emulator residuals form a distribution that has similar spread to that of the ensemble, or "model", residuals that account for the natural variability. In doing so, we can achieve a smooth response surface because it no longer has to interpolate the points exactly (Figure 3.9b).

We use the variance of the model residuals to estimate an appropriate nugget term, as follows. For each of the training points, Z_i, in the training data set $Z_1, ..., Z_l$, running initial-condition ensembles gives a set of estimates, $(Z_i^{(1)}, ..., Z_i^{(k)})$, for k ensemble members at Z_i. The liquid water path values averaged over the last two hours in Figure 3.10a show that the variance increases with the mean value. The ensemble means are calculated as

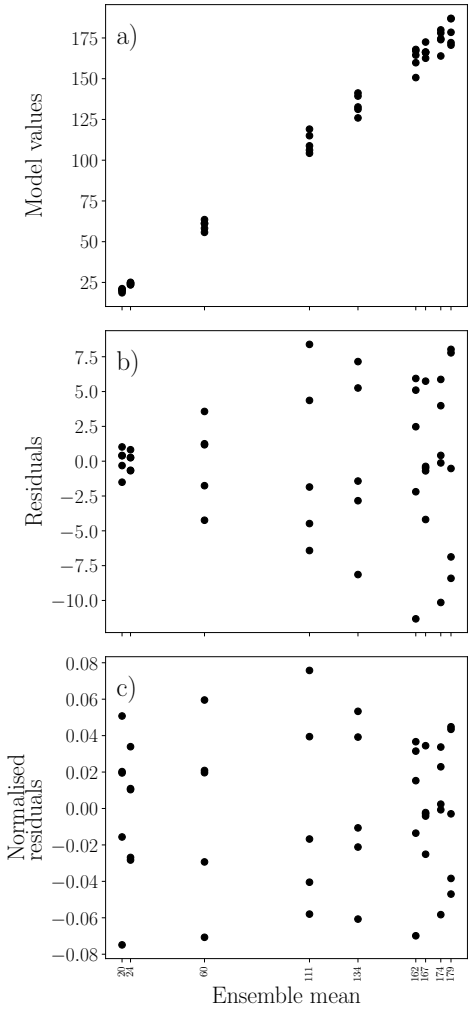

Figure 3.10: Initial-condition "model" ensemble variances. The nine ensemble mean values against a) the 5-member ensemble model values b) the residual values, and c) the residual values normalised by each of the ensemble means.

$$\bar{Z}_i = \frac{1}{k}\sum_{j=1}^{k} Z_i^{(j)}. \tag{3.6}$$

The variances of the model residuals, σ_i^2, between the ensemble members and the ensemble mean also increase with the mean liquid water path (Figure 3.10b). To combine these into one distribution we normalise the model residuals and assume that the normalised variance is constant across the response surface. Note that other data may require a different normalisation process, or may already be normal. Here we can normalise by dividing by the model residual means to obtain the normalised model residuals as:

$$r_i^{(j)} = \frac{Z_i^{(j)} - \bar{Z}_i}{\bar{Z}_i}, \tag{3.7}$$

as shown in Figure 3.10c. We can then assume that each normalised residual is drawn from a normal distribution, R, with mean μ (=0) and standard deviation σ,

$$R \sim \mathcal{N}(\mu,\, \sigma_R^2).$$

Our hypothesis is that using the residual distribution's variance, σ_R^2, is an appropriate substitute for using the variance for each initial-condition ensemble, σ_i^2, which we could only know by running ensembles at every training point. We can use the variance of the sample of model residuals to estimate the population variance

$$\sigma_R^2 = \frac{\sum(r-\mu)^2}{N_R}, \tag{3.8}$$

for the number, N_R, of residuals, r, in the distribution. However, since we normalised the residuals by the ensemble means, we need to multiply by a factor on the same order magnitude as $\bar{Z}_i^2$ to use this estimate in the emulation process (see Appendices A.5 and A.6).

We ran 5-member ensembles at nine training points to estimate the natural variability captured in the model. The timeseries evolution of the ensembles is shown in Figure 3.4 and the intra-ensemble differences in the simulated final cloud fields are shown in Figure 3.11. We explored how the estimated variance depends on the number and location of initial-condition ensemble points in parameter space. We found that a similar result could be achieved from initial-condition ensembles at just three well-spaced points, rather than the full nine (Appendix A.6).

The nugget term is applied as a noise vector, $V = (v_1, ..., v_l)$, where v_i is an estimate

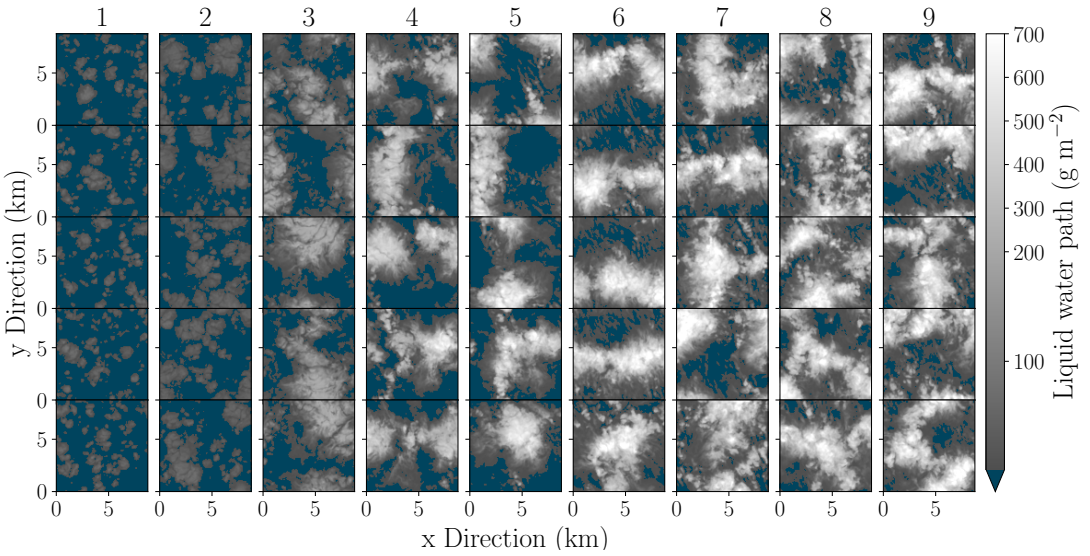

Figure 3.11: Top-down views of the in-cloud liquid water path in the final timestep for each five-member ensemble simulation.

for the variance, σ_i^2, that should be applied at each Z_i. We trialled multiplying our estimate of σ_R^2 by three different squared factors: the value of the cloud property variable at each training point (proportional); the mean value over all training points in the PPE; and the maximum output value from the PPE over the whole parameter space. Two additional noise vectors were tested where we used arbitrary numbers of the maximum value $\times 10$ and $\times 100$.

Figure 3.12 shows that the distribution of emulator residuals compares best with the residual distribution from the model ensembles when we use the max or $\times 10$ multipliers. The largest overlap of the two distributions (0.78) comes from the maximum multiplier in column d. We used the Kolmogorov-Smirnov (KS) two-sample test to test whether these distributions are statistically likely to be from the same distribution. For those with a KS p-value less than 0.05 we must reject the null hypothesis that the samples are drawn from the same distribution, so only the maximum multiplier and the $\times 10$ nugget (columns d and e) fulfil this criteria. The $\times 100$ nugget term (column f) shows that at some point the nugget term is too large and the emulator loses all information from the training data points and defaults to the underlying prior linear function. This appears as a smooth linearly increasing surface across parameter space and does not fit well with the training data. For smaller nugget variances (columns a, b, c) the distribution of the surface residuals is narrower than the distribution of the initial-condition ensembles, showing that the emulator surface is forced to pass too closely to the individual training points.

Figure 3.13 shows the validation of each cloud property emulator with a nugget term added (Figure 3.12d for the liquid water path, the other three cloud property

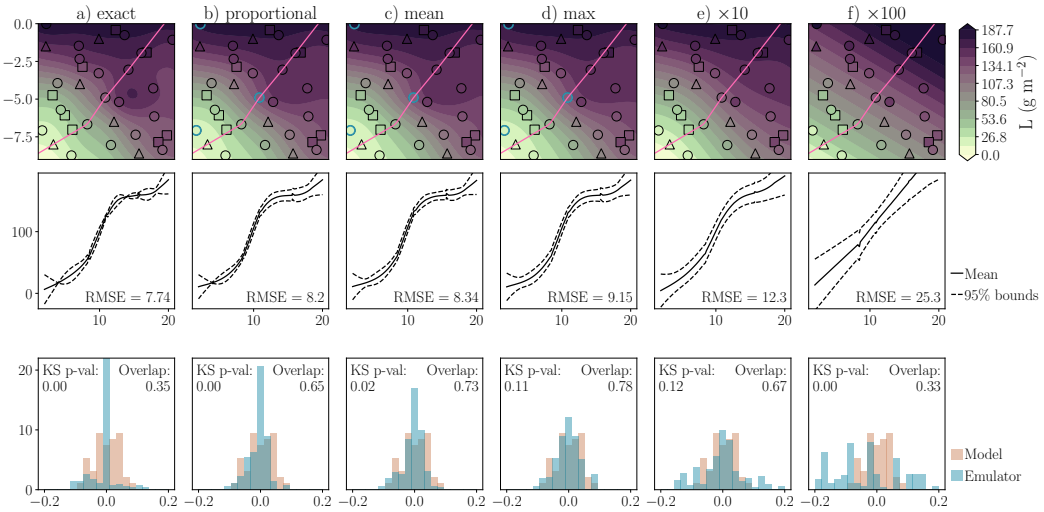

Figure 3.12: The mean liquid water path emulator with different nugget terms applied. a) No nugget term, b) multiplying factor proportional to the training point value, c) mean PPE value multiplying factor, d) maximum PPE value multiplying factor, e) maximum factor ×10, f) maximum factor ×100. Top row: emulator predicted response surfaces. Middle row: a transect through the pink line shown in top row showing mean emulator function and upper and lower 95% confidence bounds. Bottom row: comparison of the histograms of surface residuals and the initial-condition ensemble residuals (Figure 3.9). The RMSE, Kolmogorov-Smirnov p-values, and overlap values are given for each nugget term. The overlap value is computed as the fraction of histogram bars that overlap between the datasets.

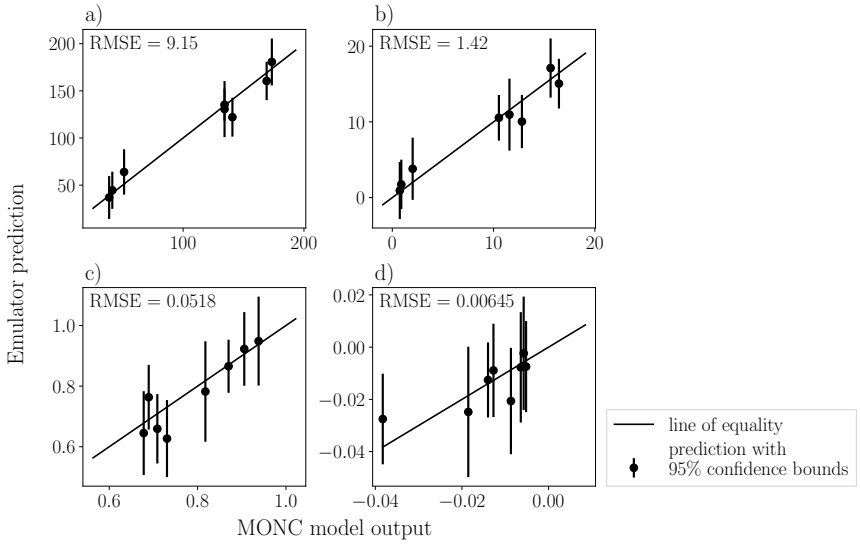

Figure 3.13: Validation plots for the four cloud property emulators with a nugget term included (response surfaces in Figure 3.14). a) liquid water path (g m^{-2}), b) liquid water path tendency (g m^{-2} hr^{-1}), c) cloud fraction and d) cloud fraction tendency (hr^{-1}). The MONC output values for each point are on the x axis and the emulator predicted values are on the y axis. The black line shows the line of equality and the error bars indicate the 95% confidence bounds on the emulator mean predictions.

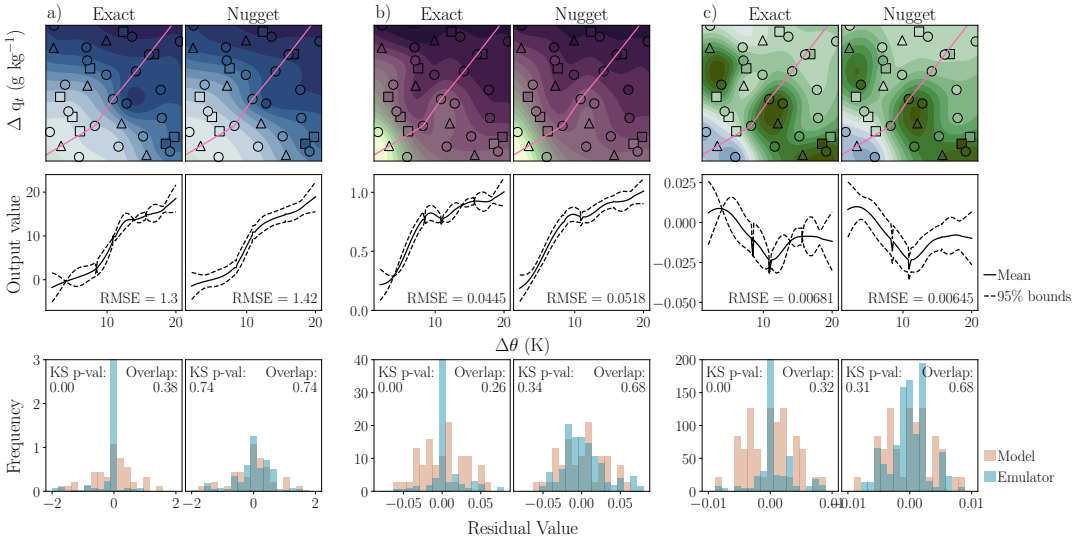

Figure 3.14: The cloud property emulators with and without a nugget term applied. a) liquid water path tendency, b) cloud fraction and c) cloud fraction tendency. Top row: the response surface produced from the emulator predictions. Middle row: a transect through the pink line shown on the response surface with the mean emulator function and the upper and lower 95% confidence bounds. Bottom row: comparison of the histograms of surface residuals and the point-ensemble residuals (Figure 3.9). The RMSE, Kolmogorov-Smirnov p-values, and overlap values are given for each nugget term. The overlap value is computed as the fraction of histogram bars that overlap between the datasets.

nuggets are discussed shortly in reference to Figure 3.14). This figure shows that the 95% confidence bounds have increased in size, as is expected, and in most cases the RMSE has increased, but the predictions are still within the 95% confidence bounds. The cloud fraction tendency RMSE has decreased because this dataset has a very high variability.

In Figure 3.14 we show how adding an appropriately sized nugget term to the remaining emulators removes some of the bumpy behaviour created by the natural variability of the model. We found the procedure for calculating the nugget depended on the output of interest. The residuals from both tendencies could be combined without normalisation, whereas the liquid water path and cloud fraction both required that the residuals were normalised by dividing by the mean. For the liquid water path tendency, we found that using all nine points or some combinations of only three points gave an appropriate nugget. For the cloud fraction and cloud fraction tendency, we found that only the nugget that includes all nine points was appropriate. These required more points because three points that cover a range of behaviour in one cloud property do not necessarily cover the full range of behaviour in another cloud property. For all of these response surfaces with the nugget added, the behaviour across parameter space remains approximately as described in section 3.5.2, but it is now smoother and represents the model's general behaviour better.

3.7 Discussion

In the parameter space we explored, we found there are two distinct behavioural cloud regimes with a smooth transition between them, rather than a discontinuity. As such, we do not find that there is a distinct point beyond which the cloud rapidly breaks up. However the κ parameter hypothesised by Randall (1980) and Deardorff (1980) does approximately mark a change in behaviour between region A (figure 3.7), where there is thin stratocumulus cloud (or small cumulus) and very little growth, and region B, where there is a high cloud fraction of stratocumulus cloud with a moderate liquid water path that grows throughout the simulation. Emulation allowed us to densely sample the parameter space to map out cloud behaviour based on model output and identify interactions between the parameters, and the addition of the nugget term more smoothly captures the underlying deterministic behaviour. Thus, a firm conclusion was drawn about the nature of the transition across parameter space.

Without including aerosol processes in the simulation some aspects of the cloud breakup may not be accounted for, such as rain-depletion feedbacks (Goren et al., 2019). Our base simulation differed from the observed case because we had a lower fixed droplet number concentration, however we tried the same set of simulations with a higher fixed droplet number concentration and found a similar pattern across parameter space. The lack of rapid cloud breakup fits with the conclusion in Mellado (2017) that the feedback mechanism is too weak to cause the cloud to break up by itself.

We have demonstrated the use of a nugget term in building an emulator that accounts for cloud natural variability. Although previous studies have run initial-condition ensembles and used the mean as training data (Johnson, Gosling, and Kennedy, 2011) this has not been done with cloud or climate models due to the expense of running the ensembles. In our method to estimate the variance of the model residuals, we found that information from three well-spaced ensemble points often produced a similar result to the whole nine ensembles. In a higher dimensional parameter space it is harder to judge whether the points are spaced well, but even a small number of point ensembles would take one closer to an approximate estimate. When emulating a stochastic (or quasi-stochastic) model, the inclusion of a nugget term that is large enough to account for natural variability helps to produce a deterministic view of the behaviour across parameter space.

One unexpected benefit of creating a PPE and emulating to produce a response surface was the ability to immediately spot outliers in the data. Against the backdrop of the PPE and the emulated surface these simulations clearly stand out, allowing us to further investigate why they do not fit with the rest of the data. In some cases, this could identify an interesting region of parameter space in the real world,or a natural variability extremity that could be investigated with a small ensemble, or perhaps a

collection of parameter settings for which the model is unstable. If none of those are true and it is simply a bad datapoint, perhaps a corrupted value in the model, it has been caught and can be discarded with minimal confusion.

As computing capabilities increase and climate models get more complex, machine learning techniques are becoming a vital tool for sifting through data and making sense of the results. The number of simulations required to fully explore uncertainties and certain aspects of models is already infeasible, particularly with the non-linear behaviour of clouds. Statistical emulation has proven to be an immensely useful tool for sensitivity analysis of model parameters in climate studies, but here we have shown it in a different capacity by perturbing the initial profiles of cloud-controlling factors, which has only recently begun to be explored. We believe it is an essential tool for exploring cloud processes as we expand to include changes in aerosol concentrations, parameterisation coefficients and more meteorological parameters.

We have shown that at low dimensions the visual mapping between relationships is very informative, and finding a way to display this in a higher number of dimensions would be instrumental in further studies. Glassmeier et al. (2019) and Hoffmann et al. (2020) have already demonstrated one solution by mapping a six-dimensional input parameter space into a two-dimensional state space creating graphics that concisely give a huge amount of information about the relationships of interest. However, the systems cloud modellers are studying have possibly hundreds of uncertain parameters, and statistical emulation has already been used with up to around 50. Expanding to higher dimensions has increased problems of sparsity due to the "curse of dimensionality", but the saving in terms of computational resources is undeniable. In our two-dimensional case here, each simulation took 8 to 10 hours to run on a high-performance computer, yet to emulate and sample the rest of parameter space took only a few seconds on a standard laptop.

3.8 Conclusions

We have used Gaussian process emulation to analyse and visualise the dependence of stratocumulus clouds on the initial profiles of two cloud-controlling factors and their interactions. This method is particularly useful for low, shallow clouds and understanding the covariance between the factors involved in different processes. We have found that the parameter space we explored can approximately be split into two cloud behavioural regimes, with a smooth, yet steep, gradient between them. However, we did not find a point of rapid cloud breakup, rather there is a small corner of parameter space, where the free troposphere is dry and cool, where stratocumulus clouds were not produced. Below the threshold, in the moist, warm free-tropospheric conditions, there is generally high liquid water path and high cloud fraction, with cloud thickening (increasing liquid

water path) and aggregation (clustering in the cloud fraction). Above the threshold, in the dry, cool free-tropospheric conditions, there is low liquid water path, and medium cloud fraction, that is fairly stable or marginally thickening. We used a nugget term to account for cloud natural variability that is captured in the model and in doing so have represented deterministic behaviour across parameter space, instead of individual model realisations. This also allowed us to smooth out extrema that were artefacts of the emulator fitting. We used initial-condition ensembles to estimate the appropriate size of nugget and found that taking the normalised residual variance and multiplying by the maximum value in the PPE gave the best fit.

Using an emulator in this way helps to visualise the relationships between parameters of interest and the model output at a much-reduced computational cost. This is sorely needed in the study of shallow clouds and their behaviours. Our future work will go on to expand the PPE to consider many more parameters, crucially aerosol concentrations, so that we may delve into the heart of understanding these complex systems and all the factors that make up the whole without breaking it down to its parts.

Chapter 4

A perturbed parameter ensemble analysis of the roles of cloud-controlling factors in the stratocumulus-to-cumulus transition

4.1 Abstract

The transition from stratocumulus to cumulus clouds in marine capped boundary layers leads to a halving in cloud fraction and a large change in the cloud radiative effect on climate. In the subtropics, the transition occurs when cloudy air is advected over increasingly warmer sea-surface temperatures. Many environmental or 'cloud-controlling' factors affect the transition, with lower-tropospheric stability being a dominant factor. Previous studies have explored some of these factors, such as large-scale divergence and cloud droplet number concentration, and found that drizzle has only a small role in the transition mechanism. However, very few of these studies have used a microphysics scheme that includes aerosol processing, and even fewer have considered aerosol with the wider environmental conditions. Here, a 97-member perturbed parameter ensemble of a large-eddy simulation model is used to assess how 5 atmospheric initial conditions and 1 microphysical model parameter affect the transition in the Northeast Pacific. A stratocumulus-to-cumulus transition is produced in 34 of these simulations, which gives a huge range of environmental conditions to explore. The results show that aerosol concentration and boundary layer moisture have the strongest correlations with transition time across the perturbed ranges. The ensemble shows the joint effects that factors

have on the transition time. The fastest transitions (under 40 hours) correspond to simulations with low aerosol combined with deep boundary layers, high autoconversion rates and a dry temperature inversion. The amount of drizzle is largely controlled by the boundary layer depth, but the drizzle does not solely determine the transition time. The aerosol has an even stronger relationship with transition time in high drizzle environments and the inversion strength has a larger impact than most of the other factors, via its control of entrainment rate, in low-drizzle environments.

4.2 Introduction

Stratocumulus-to-cumulus transitions occur on the eastern sides of major ocean basins when stratocumulus decks are advected towards the equator across increasingly warmer sea-surface temperatures (SST) (Klein and Hartmann, 1993; Albrecht et al., 1995). There is a large decrease in cloud fraction (and consequently albedo and radiative forcing) as the cloud type transitions to cumulus. Understanding the drivers behind cloud transitions is key to predicting how these cloud regimes will change in the future climate. The stratocumulus-to-cumulus transition is governed by many cloud-controlling factors, whose contributions are still an area of active research. This uncertainty leads to poor parameterisations in global climate models so transitions are not captured well, which creates large uncertainties in simulated cloud properties and their responses to the warming climate (Bony and Dufresne, 2005; Teixeira et al., 2011; Eastman et al., 2021). Low clouds in the subtropics have a cooling effect on the planet, so future decreases in cloud fraction reduce that cooling effect, amplify warming, and contribute to a positive cloud feedback effect (Bretherton, 2015; Ceppi et al., 2017; Nuijens and Siebesma, 2019). Further process understanding of cloud transitions can improve their representation in global climate models and reduce the uncertainty surrounding cloud adjustments and feedbacks.

The typical transition mechanism, termed deepening-warming decoupling, has been determined through observational studies (Paluch and Lenschow, 1991; Bretherton and Pincus, 1995; Bretherton, Austin, and Siems, 1995; Martin et al., 1995; Wang and Lenschow, 1995; Klein, Hartmann, and Norris, 1995; de Roode and Duynkerke, 1996; Pincus, Baker, and Bretherton, 1997) and high-resolution modelling (Krueger, McLean, and Qiang Fu, 1995; Wyant et al., 1997; Bretherton and Wyant, 1997; Svensson, Tjernström, and Koračin, 2000). It describes how the increasing SSTs cause the boundary layer turbulence to be increasingly driven by surface fluxes that deepen the boundary layer. As the boundary layer deepens, mixing throughout the full layer can no longer be sustained and the layer decouples into a stratocumulus cloud layer, and a surface-coupled subcloud layer. Once decoupled, the stratocumulus layer is cut off from the ocean as a moisture source, but the subcloud layer becomes more turbulent, warmer and moist from surface evaporation until cumulus plumes develop. In this cumulus-

under-stratocumulus stage, the plumes at first provide moisture and turbulence to the stratocumulus layer, but more-energetic plumes overshoot and the vigorous mixing eventually dissipates the stratocumulus cloud resulting in a field of cumulus.

The role of drizzle in the transition remains unclear and inconsistent between studies (Miller and Albrecht, 1995; Wang, 1993; Pincus, Baker, and Bretherton, 1997; Svensson, Tjernström, and Koračin, 2000). Several modelling studies have found that drizzle has a small effect on the transition compared to other cloud-controlling factors (Sandu and Stevens, 2011; McGibbon and Bretherton, 2017; Blossey, Bretherton, and Mohrmann, 2021). Sandu and Stevens (2011) used large-eddy simulation (LES) of a composite case derived from thousands of trajectories in the North East Pacific in Sandu, Stevens, and Pincus (2010) as a basis from which they perturbed cloud-controlling factors. They reduced the cloud droplet number concentration from 100 to 33 cm^{-3} to allow precipitation to form earlier and this limited the boundary layer recovery from decoupling through the day by moistening and cooling the subcloud layer, and depleting the cloud layer of water. The increased precipitation caused the cloud to break up sooner, but it is suggested here that initial strength of the temperature inversion capping the boundary layer has the strongest control on the timing of the breakup. This and many other LES studies used a fixed droplet number. Yamaguchi, Feingold, and Kazil (2017) suggested that using a fixed droplet number does not allow for rain feedback mechanisms, which require representation of aerosol in collision-coalescence processes for appropriate droplet depletion.

Including aerosol in LES cloud simulations ensures that there is a feedback between the reduction of droplets as they collide and the reduction in aerosol number concentration, which then further reduces cloud droplet number. Yamaguchi, Feingold, and Kazil (2017) used a bin-emulating bulk microphysics scheme that included aerosol processing in an LES model. They found evidence of a fast transition mechanism initiated by drizzle that develops at the cumulus-under-stratocumulus stage, in a low aerosol environment. In the proposed mechanism, the drizzle droplets are formed in the cumulus plumes and strong updrafts carry them to the stratocumulus layer where they enhance drizzle production because they are larger than the stratocumulus cloud droplets, and therefore more efficient collectors. Through collision-coalescence and wet scavenging, the droplet number and aerosol concentrations are reduced leading to even heavier drizzle, more reduction and a runaway feedback. Using the same model for a different case, Diamond et al. (2022) found also a rapid reduction in cloud fraction through drizzle depletion in low aerosol conditions. However they suggested that the end state was more of an open-cellular organisation rather than a cumulus state. Erfani et al. (2022) considered the two trajectories simulated in Blossey, Bretherton, and Mohrmann (2021), but included a single-mode bulk aerosol scheme with aerosol processing within cloud droplets, and also found precipitation to be a driver of the transition. These

studies do not fully consider the effect of aerosol concentration in the context of other cloud-controlling factors: Diamond et al. (2022) perturbs some large-scale forcings but with a focus on smoke effects and the two trajectories in Erfani et al. (2022) have very different initial conditions but these cover only two extreme cases.

Observations from ships and satellites, along with reanalysis data, provide the wider context of the meteorological conditions (e.g. Mauger and Norris, 2010), but they have not shown clear evidence of a rapid transition to cumulus by a drizzle-depletion mechanism (Pincus, Baker, and Bretherton, 1997; Zhou, Kollias, and Lewis, 2015; Brendecke et al., 2021). Eastman and Wood (2016) conducted a large analysis of Lagrangian trajectories from satellite data and in particular focused on the effect of boundary layer depth, the inversion strength and precipitation on cloud evolution. They found that deep boundary layers and weak inversions tend more towards cloud breakup, but precipitation effects were less clear: in shallow boundary layers, precipitation sustained the cloud longer whereas in deep boundary layers it tended to cause the cloud to break up. Despite finding that aerosol on average increased cloud fraction, Christensen, Jones, and Stier (2020) also did not find precipitation or low aerosol to be a strong driver of cloud breakup. Eastman, McCoy, and Wood (2022) assessed the difference between closed-cell stratocumulus that does transition and that which does not. They find heavy precipitation is linked closely with a transition to open-cell stratocumulus, but the transition to a cumulus state is more likely caused by excess entrainment at cloud top.

There are no studies on the role of drizzle in the stratocumulus-to-cumulus transition that combine the wider meteorological context with high-resolution cloud modelling. Several LES studies have made large one-at-a-time perturbations to wider meteorological conditions, such as subsidence, droplet number, radiation and latent heat fluxes (Sandu and Stevens, 2011; van der Dussen, de Roode, and Siebesma, 2016; Zheng, Zhang, and Li, 2021). There have been LES model intercomparisons of the transition that, when compared with observations, highlight which structural differences create the largest disparities in replicating observed transitions (Bretherton et al., 1999b; van der Dussen et al., 2013; de Roode et al., 2016). Other studies have made small perturbations to initial conditions to represent different stages of the transition (Chung, Matheou, and Teixeira, 2012; Tsai and Wu, 2016; Bellon and Geoffroy, 2016). Additionally, several groups have simulated specific observed or calculated trajectories that have completely different sets of initial conditions and very different characteristics of transition (Goren et al., 2019; Blossey, Bretherton, and Mohrmann, 2021; Erfani et al., 2022). Within these studies, precipitation is found to have no effect or slightly hasten the transition but it is not found to be a key driver. Yet all of these studies are limited to one-at-a-time perturbations or only consider a couple of possible trajectories when there are a very wide range of cloud-controlling factors. In doing so, they barely sam-

ple the parameter space and may miss the covariance of meteorological factors in this complex process (Feingold et al., 2016).

In this study we have used an LES model to create an ensemble of stratocumulus-to-cumulus transitions initiated with a wide range of meteorological conditions covering key cloud-controlling factors. We define "transition" as the time (in hours) taken to transition from the initial stratocumulus state to a cumulus state. Given the potential importance of drizzle formation, the ensemble also samples a range of rates of autoconversion of cloud droplets to rain droplets. Each of these perturbed factors has the potential to affect the characteristics of the transition. In perturbing them together in a perturbed parameter ensemble (PPE) we can learn how these factors jointly affect the transition.

We address the following questions. Do the fastest transitions occur in low aerosol environments? Are the fast transitions limited by other cloud-controlling factors or the autoconversion rate? Under what conditions does drizzle play an important role in the transition? Section 4.3 describes the model setup and ensemble design before the results are shown in section 4.4 and discussed in greater detail in section 4.5.

4.3 Simulation and ensemble design

4.3.1 Model configuration

The ensemble of simulations generated in this study is based on the composite case created for the NE Pacific Ocean basin in Sandu and Stevens (2011). Sandu, Stevens, and Pincus (2010) calculated thousands of forward and backward air parcel trajectories from areas of extensive cloud cover, over six days of advection, and retrieved the boundary layer properties for this period from satellite data and meteorological reanalysis. The averaged datasets were found to be representative of individual trajectories, so they used a subset to build a reference case for the three days where the majority of the transition takes place (see Sandu and Stevens, 2011). This meteorological state in this reference case is a good starting point for simulating a typical transition, which can then be perturbed to explore cloud behaviour over a wider range of cloud-controlling factors.

The ensemble was simulated using the LES model from the UK Met Office and National Environmental Research Council (NERC), called the MONC (Met Office/NERC Cloud) model (Dearden et al., 2018; Poku et al., 2021; Böing et al., 2019). The MONC model solves a set of Boussinesq-type equations and here we have used the anelastic approximation, which is based on a reference potential temperature profile that depends only on height. The subgrid turbulence parameterization is an extension of the Smagorinsky-Lilly model and is based on that described in Brown, Derbyshire,

and Mason (1994). Here, MONC was coupled to the 2-moment Cloud AeroSol Interaction Microphysics scheme (CASIM) (Shipway and Hill, 2012; Hill, Shipway, and Boutle, 2015) and the Suite of Radiation Transfer Codes based on Edwards and Slingo (SOCRATES) (Edwards and Slingo, 1996).

Stratocumulus-to-cumulus transitions are often simulated in a Lagrangian style, where the domain moves with the advection of the cloudy air (Krueger, McLean, and Qiang Fu, 1995; Sandu and Stevens, 2011; de Roode et al., 2016). Here, although our model domain is advected along a typical airmass trajectory, we retained wind profiles to ensure there was appropriate ocean surface evaporation, but the model has periodic boundary conditions so the domain was always focused on the same cloud cell. As in other studies, we simulated the advection towards the equator by forcing the SSTs to increase over the course of the simulation. The simulations were run for 3-4 days and the SST is increased by nearly 1.5 K per day, following Sandu and Stevens (2011), Bretherton and Blossey (2014) and Yamaguchi, Feingold, and Kazil (2017). The domain was 12.8 by 12.8 by 3.1 km^3. The horizontal resolution was 50 m, and the vertical resolution varied from 20 m near the surface, to 5 m around the temperature inversion, and gradually increased above that.

CASIM is a 2-moment bulk microphysics scheme that represents hydrometeors using gamma distributions for mass and number (Grosvenor et al., 2017). In this study, we used only warm-cloud processes (cloud liquid and rain) since ice processes are not part of the stratocumulus-to-cumulus transition in the NE Pacific. The simulations are initiated with soluble aerosol, also represented by mass and number prognostics, in the Aitken and accumulation modes. The Aitken mode distribution has a standard deviation of 1.25 and a mean radius of 25 nm. The accumulation mode distribution has a standard deviation of 1.5 and a mean radius of 100 nm. The density of all aerosol particles is assumed to be 1500 km m^{-3}. At saturation, the number of aerosol particles activated into cloud droplets is calculated using the scheme of Abdul-Razzak and Ghan (2000), and these activated aerosol are represented using a separate in-cloud prognostic. The aerosol contained within droplets grows through droplet collision and coalescence with the assumption that one aerosol particle is present in each droplet, and is returned to the appropriate aerosol size mode on evaporation of the cloud droplets (including the coarse mode). Accretion and autoconversion are represented by the Khairoutdinov and Kogan (2000) parameterization. Rain evaporates in the subsaturated grid boxes, but aerosol is not returned to the size modes through this process.

4.3.2 Perturbed parameter ensemble

We used a PPE in this study because it is a valuable tool for learning about the covarying effects of parameters on model output. This is especially true for cloud systems, where a shift in some cloud property in response to an environmental change may

Table 4.1: Parameter descriptions, symbols and ranges in parameter space.

Parameter description	*Symbol*	*Range*
BL vapour mass mixing ratio	BL q_v	7 to 11 g kg^{-1}
BL depth	BL z	500 to 1300 m
Inversion jump in potential temperature	$\Delta\theta$	2 to 21 K
Inversion jump in vapour mass mixing ratio	Δq_v	-7 to -1 g kg^{-1}
BL aerosol concentration	BL N_a	10 to 500 cm^{-3}
Autoconversion rate parameter	b_{aut}	-2.3 to -1.3

be buffered by another change that has occurred. Perturbing multiple environmental conditions simultaneously and in a well-designed way allows us to understand more about the combinations of parameters that affect certain outputs of the model. We perturbed five cloud-controlling factors, which relate to features of the initial thermodynamic vertical profiles, and a sixth factor that determines the autoconversion rate, which is a model process-related parameter in the CASIM code (see Table 4.1). All factors were perturbed over a range that has the base simulation (Sandu and Stevens, 2011) well within it. The initial vertical profiles evolve a small amount during model spinup, therefore in our exploration of their joint effects we analysed dependencies of cloud properties on the initialised factors and their post-spinup values (see Appendix B.1).

Boundary layer vapour mass mixing ratio

We perturbed the boundary layer vapour mass mixing ratio (specific humidity) since this directly determines at what point saturation is reached and how much moisture is available for cloud droplets to form. It also determines how much drizzle will be evaporated below cloud base.

Inversion properties

We perturbed three properties of the inversion; the jumps in potential temperature and specific humidity across the inversion, and boundary layer depth. The dissipation of the stratocumulus cloud is a defining part of the transition and is largely caused by the entrainment of warm, dry air from above the inversion, via overshooting cumulus plumes. Thus, the rapidity of this dissipation is related to the strength of the inversion and the humidity in the free troposphere (Wood et al., 2018), which can be perturbed with the changes in temperature and moisture across the inversion (the jump in potential temperature will be used interchangeably with inversion strength). Additionally, the humidity in the free troposphere determines the rate of longwave cooling which relates to entrainment and evaporation (Siems, Lenschow, and Bretherton, 1993). The boundary layer depth was perturbed since it determines how well mixed the boundary layer can be, and consequently how well supplied with surface-evaporated moisture the

stratocumulus cloud layer is. Eastman and Wood (2016) showed that precipitation may have opposite effects on stratocumulus cloud transitions depending on whether it is occurring in deep layers, leading to break up, or shallow layers, leading to cloud persistence.

Boundary layer aerosol

We perturbed the initial boundary layer concentration of accumulation mode aerosol. Most aerosol that activates into cloud droplets (cloud condensation nuclei) is from the accumulation mode. The free-tropospheric aerosol can also be a source of cloud condensation nuclei and could be important in simulations with low aerosol concentrations in the boundary layer (Wyant et al., 2022). However, the effect of this source is beyond the scope of this paper so we kept the free-tropospheric concentrations constant across the ensemble.

Autoconversion rate parameter

The autoconversion rate determines how readily cloud droplets form rain droplets in a parameterisation of the collision-coalescence process. In the Khairoutdinov and Kogan (2000) parameterisation, the autoconversion rate is given by

$$\left(\frac{\delta q_r}{\delta t}\right)_{auto} = 1350 q_c^{2.47} N_c^{-1.79},$$

where q_r is the rain mass-mixing ratio, q_c is the cloud liquid mass-mixing ratio (both in kg kg^{-1}), and N_c is the cloud droplet number concentration (cm^{-3}). We have perturbed the exponent of cloud droplet number concentration from its value of -1.79. The parameter values in this approximation have been estimated by reducing the mean squared error between this function and an explicit microphysics model, and as such, there is a large uncertainty for each of these values. There has been some progress on refining parameterisations of autoconversion (Kogan, 2013). Here, we want to compare the sensitivity of cloud properties to environmental conditions with the effect of this key uncertain model parameter.

Perturbation method

The six parameters were simultaneously perturbed using a Latin hypercube to design which combinations of parameter values within the chosen ranges to use. We used a "maximin" Latin hypercube approach that maximises the minimum distance between points to ensure that values are well-spaced across a multi-dimensional parameter space and each 1-dimensional axis (Morris and Mitchell, 1995). Figure 4.1 shows the design in the 6-dimensional parameter space. The values for the autoconversion parameter have

been transformed using the inverse log since it is the exponent of N_c. This means that the resulting autoconversion rates were approximately uniformly distributed, rather than the values for the parameter.

We ran 85 simulations initially, but found that 31 did not form stratocumulus because the boundary layer was too shallow and dry (see Appendix B.2). Out of those simulations that had stratocumulus, 26 did not transition to a cumulus state before the end of the simulation. We expected that not all the simulations would produce transitions since we have broadly perturbed initial conditions to sample a wide range of model behaviour. The remaining 28 simulations that transitioned to cumulus were topped up by 6 transitioning simulations, out of 12 points that were augmented to the original design. These additional 12 were augmented based on our new understanding of the regions of parameter space that would not produce stratocumulus and were unlikely to transition within simulation time.

The ranges for each parameter were chosen to span the breadth of the studies on stratocumulus-to-cumulus transitions in the subtropics. Often case studies are designed for LES simulation from observations of particularly fast or slow transitions, so a broad range of behaviours were included in the parameter space by spanning these reported cases (Sandu and Stevens, 2011; de Roode et al., 2016; Blossey, Bretherton, and Mohrmann, 2021). Since many LES studies have not focused on the aerosol effect, the range for the accumulation mode concentrations was informed by the Cloud System Evolution in the Trades (CSET) and Marine ARM GPCI Investigation of Clouds (MAGIC) campaigns (Bretherton et al., 2019; Painemal, Minnis, and Nordeen, 2015). Note that we have not included extremely polluted cases, such as the biomass burning region off the western coast of Africa. There is much work surrounding the aerosol semi-direct effect on the stratocumulus-to-cumulus transition in the Atlantic ocean, with some contradicting results (Yamaguchi et al., 2015; Zhou et al., 2017; Diamond et al., 2022). Further understanding of transition mechanisms will help to untangle these joint effects.

The perturbed values were used in idealised initial profiles to configure the model Figure 4.2. The jumps at the temperature inversion were applied over a vertical distance of 30 m, and the lapse rates in the free troposphere were consistent across all simulations. The initial boundary layer potential temperature was set at 290.70 K for all simulations. Although not perturbed, the initial Aitken mode concentration was set as 150 cm^{-3} in the boundary layer and 200 cm^{-3} in the free troposphere. The initial free-tropospheric accumulation mode concentration was set as 100 cm^{-3} and perturbed in the boundary layer (Figure 4.2). To account for adjustments to the initial values after the model has completed the spin up period, we recalculated the values of the parameters after spinup and used the adjusted values as our Latin hypercube design (Figure 4.1, see Appendix B.1 for adjustments).

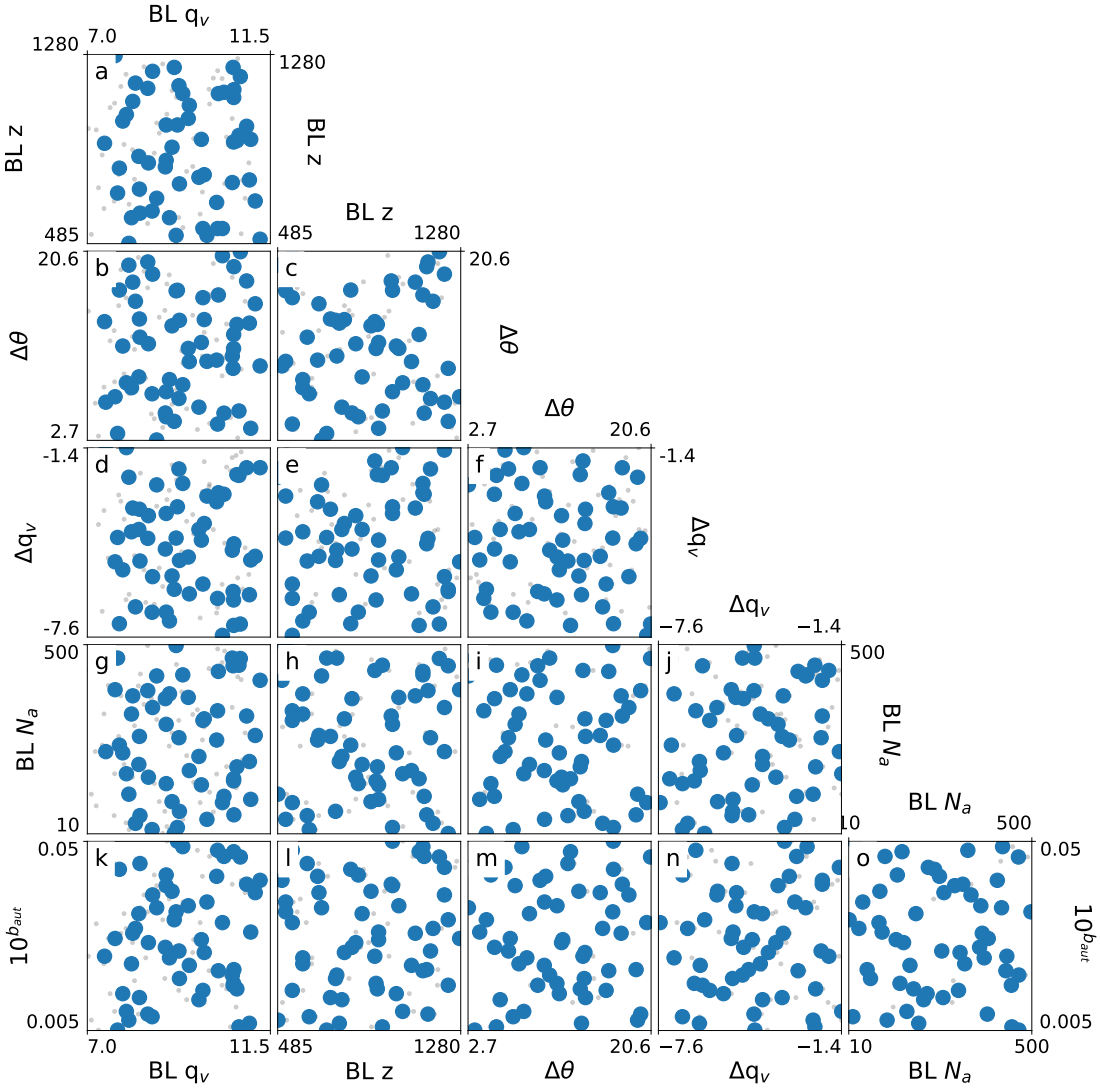

Figure 4.1: The Latin hypercube design for the perturbed parameter ensemble. Each 2-dimensional plot shows a different combination of two of the six parameters over the chosen ranges (see Table 4.1). The grey points show the values used for the initial conditions in each simulation from the original Latin hypercube design and the blue points show how these values shifted after the model had finished spinning up.

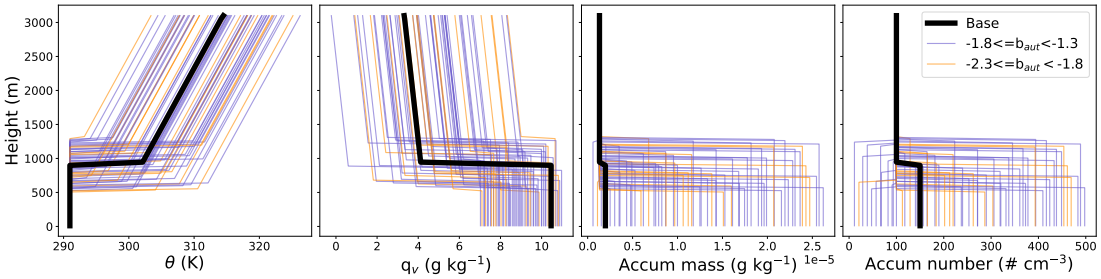

Figure 4.2: The initial profiles used to configure the model. The thick black lines shows the profiles for the base simulation and the orange and purple lines show the range across the PPE members. Purple lines have a high autoconversion rate and orange lines have a low autoconversion rate.

4.4 Results

We begin by evaluating the cloud properties in the base simulation, which is central to our PPE design. We then discuss the cloud fraction timeseries across the ensemble, before using the PPE to identify combinations of factors that control the transition time. Finally we assess the controls on drizzle and its relation to the transition time.

4.4.1 Cloud properties in the base simulation

The stratocumulus-to-cumulus transition in the base simulation is similar to that of previous LES studies based on the Sandu and Stevens (2011) composite case (Bretherton and Blossey, 2014; Yamaguchi, Feingold, and Kazil, 2017). Figure 4.3 shows three snapshots of liquid water content from the beginning, middle and end of the simulation, and their associated cloud fraction. The cloud fraction is defined as the fraction of cloudy columns with a cloud liquid mass-mixing ratio greater than 0.01 g kg^{-1}. Column a is from around 12 hours into the simulation and shows a uniform stratocumulus cloud with a cloud fraction of 0.99. The inversion height, and cloud top, are around 1000 m with a cloud layer thickness of about 300 m. Column b is from a day later and shows a slightly more broken cloud but still a high cloud fraction of 0.94. The cross section shows that the boundary layer deepened and the cloud top rose by a couple of hundred metres during the intervening day. The lowest cloud base remains around 700 m, but now the base marks the bottom of cumulus-like plumes that feed into the higher stratocumulus cloud base, around 100 m above. Since the first day, the liquid water path has decreased towards the edges of the cloud as the stratocumulus layer thinned. Column c is from the last two hours of simulation, at the end of the third day, and shows a much more broken cloud that is representative of a cumulus cell, with a cloud fraction of 0.53. At this stage the boundary layer is around another 100 m deeper and the cloud top has risen with it.

Changes in cloud properties during the simulation are shown in Figure 4.4. The

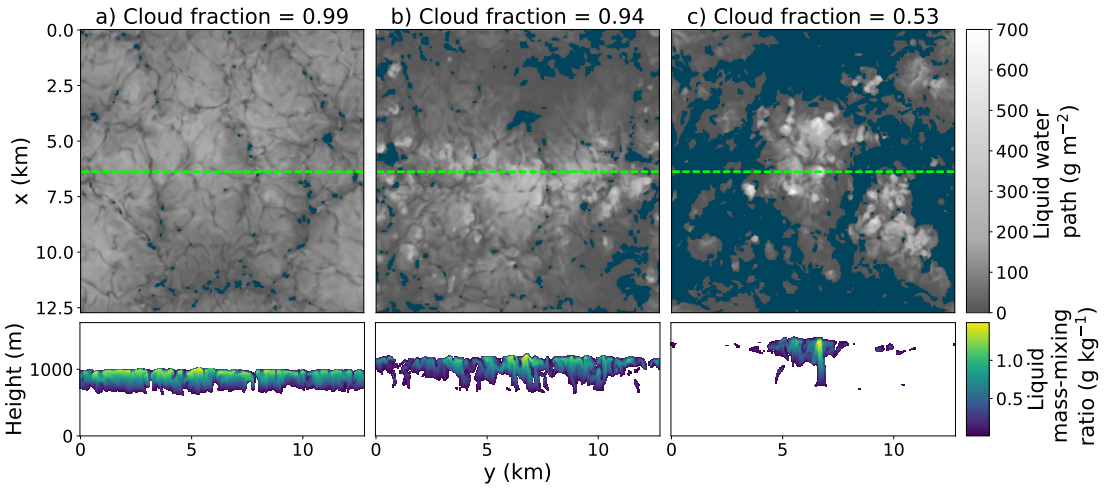

Figure 4.3: Snapshots of liquid water throughout the base simulation. The top row shows the top-down view of liquid water path and the bottom row shows a vertical cross section of liquid water mass-mixing ratio at the x location of the green dotted line in the top row. a) was taken near the beginning of the simulation at around 12 hours, b) near the middle at around 34 hours, and c) at the end at around 72 hours.

cloud fraction (a) remains near one through the first day and night, and the liquid water path (LWP: b) follows a diurnal cycle with a peak at the beginning of the second day. There is a small amount of drizzle, shown by the rain water path (RWP: b, mass mixing ratio: l) at the end of the first night and beginning of the second day. During the second day, the boundary layer begins to decouple (i), from the increase in SST and also solar surface heating, and the cloud fraction falls to around 0.9 towards the end of the second day as the boundary layer deepens and mixing is not well sustained. The cloud water recovers a little bit (LWP $\approx$ 100 g m^{-2}) at the start of the second night, through longwave cooling-enhanced convection (Wyant et al., 1997), before the drizzle increases (RWP $\approx$ 20 g m^{-2}) and the liquid water path recovery becomes limited by the drizzle and depth of the boundary layer. The cloud fraction begins to decline in the early hours of the third morning to below 0.6 midway through the day. There is a sharp drop in cloud fraction at this time where much of the remaining stratocumulus suddenly dissipates. This coincides with a sharp drop in the inversion strength (c) to around 7 K, and a decrease in the specific humidity jump (d), which is a combination of cloud evaporation (causing latent cooling and an increase in moisture) and the transport of moisture to the inversion by overshooting cumulus plumes. The boundary layer (k and l) continues to deepen to the end of the simulation, but the cloud base (k and l) remains steady. The cloud shows some recovery (cloud fraction and LWP) at the start of the third night before declining again towards the fourth day. The drizzle is less during the third night compared with the second. This shows a characteristic stratocumulus-

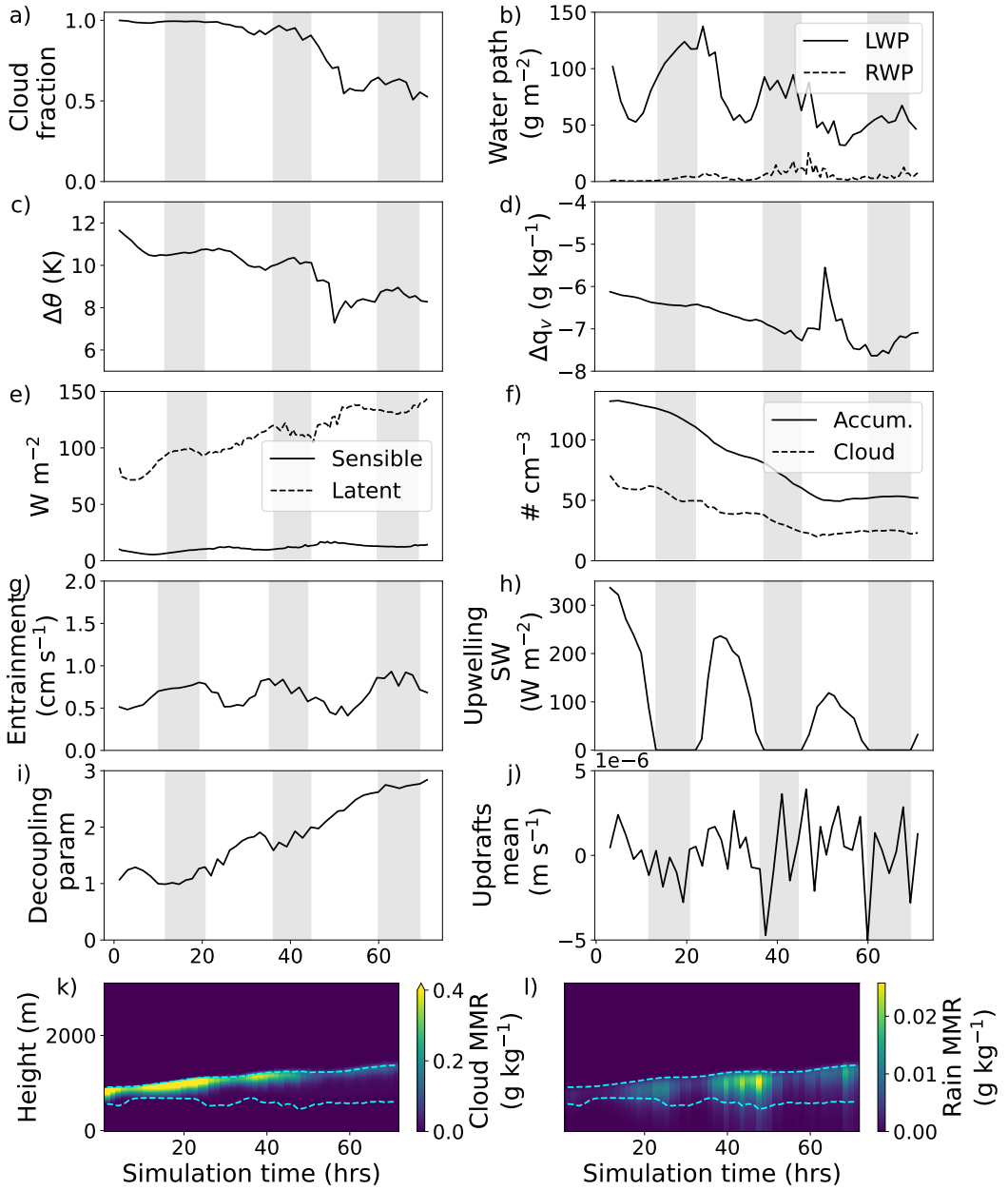

Figure 4.4: Base simulation timeseries data. a) Cloud fraction b) liquid and rain water paths c) jump in potential temperature at the inversion d) jump in vapour mass mixing ratio at the inversion e) surface heat fluxes f) droplet number concentrations g) entrainment h) upwelling shortwave radiation i) decoupling parameter - difference in total water mass mixing ratio between the bottom and top 25% of the boundary layer (Jones, Bretherton, and Leon, 2011) j) mean updraft velocity k) mean cloud liquid water mass mixing ratio (MMR) l) mean rain MMR. The blue dotted lines in k) and l) show the mean cloud base and top.

to-cumulus transition that is mostly driven by deepening-warming decoupling (Wyant et al., 1997), with a minor role from drizzle that further limits the recovery of the cloud.

Compared to other simulations of this composite case, we found that the boundary layer did not deepen to the same degree and there was less drizzle. Previous LES studies of this case resulted in a boundary layer depth between 1.5 to 2.5 km, whereas our simulation has a maximum depth of 1.4 km at the end (Sandu and Stevens, 2011; Bretherton and Blossey, 2014; de Roode et al., 2016; Yamaguchi, Feingold, and Kazil, 2017). This could be due to the different radiation schemes and mixing processes in the models, or to the stretching of the vertical layers in the top of the domain. The RWP in our simulation peaks at about 25 g m^{-2} at the beginning of the third day, which aligns roughly with the sensitivity tests in Yamaguchi, Feingold, and Kazil (2017) where they used the Khairoutdinov and Kogan (2000) parameterisation in a similar domain size. However it is much less than the peak of 150 g m^{-2} for the same domain size using their bin-emulating bulk microphysics scheme. The transitions in our simulations may be slower than those in the previous studies since the boundary layer decoupling could be limited by the shallower boundary layer and the lower RWP may limit the potential for a drizzle-depletion mechanism.

4.4.2 PPE cloud fraction analysis

In this study we have focused on the time that each simulated cloud takes to transition from a stratocumulus regime to a cumulus regime, henceforth called the transition time. Figure 4.5 shows two examples of how this was calculated for all the ensemble members based on the cloud fraction. We class the cloud as stratocumulus for a cloud fraction above 0.9 and cumulus for a cloud fraction below 0.55. Figure 4.5a shows the base simulation, which has stratocumulus from the start of the simulation (T0) so T1 is set equal to T0 although realistically T1 could be earlier. The cloud fraction decreases below the cumulus threshold just after 50 hours, but it recovers until the final time step when it reaches the threshold again, T2. We find that this member has a transition time of about 68 hours. Of course the cloud could recover again were the simulation to be run for longer. We repeated the following analysis with the criteria that clouds had to remain as cumulus for 12 hours before the simulation end and found the overall results were the same but with fewer data points so appeared noisier (Appendix B.3). Figure 4.5b shows a simulation that takes about 12 hours to build up stratocumulus, which is why we have not calculated transition time based on simulation length. Hence subtracting the time when cumulus forms, T2, from the start time of stratocumulus, T1, gives a transition time of about 32 hours.

Across the ensemble, the range of initial cloud fractions produced is large, as shown in Figure 4.6a. We expect a wide range of cloud behaviour because we have perturbed several initial conditions over a large range of environmental conditions. We have 34

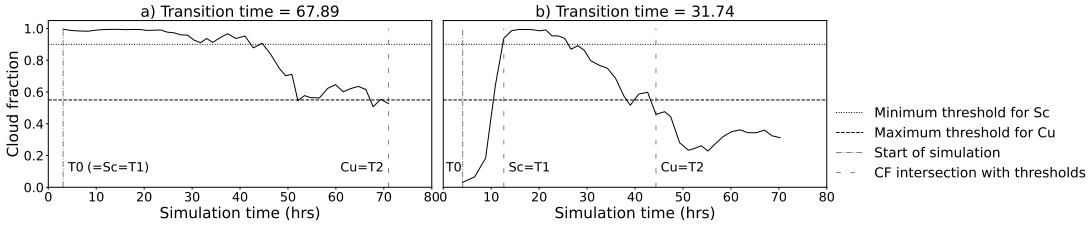

Figure 4.5: Transition time calculation based on cloud fraction. a) shows an ensemble member that has stratocumulus from the start of the simulation, T0, so T1 is set equal to T0. b) shows a member that takes about 12 hours to build stratocumulus. The solid black line shows the cloud fraction timeseries, the dotted line shows the 0.9 threshold which is the minimum for stratocumulus, the dashed line shows the 0.55 threshold which is the maximum for cumulus. The loosely dashed lines show where the cloud fraction intersects with the stratocumulus (Sc) and cumulus (Cu) thresholds.

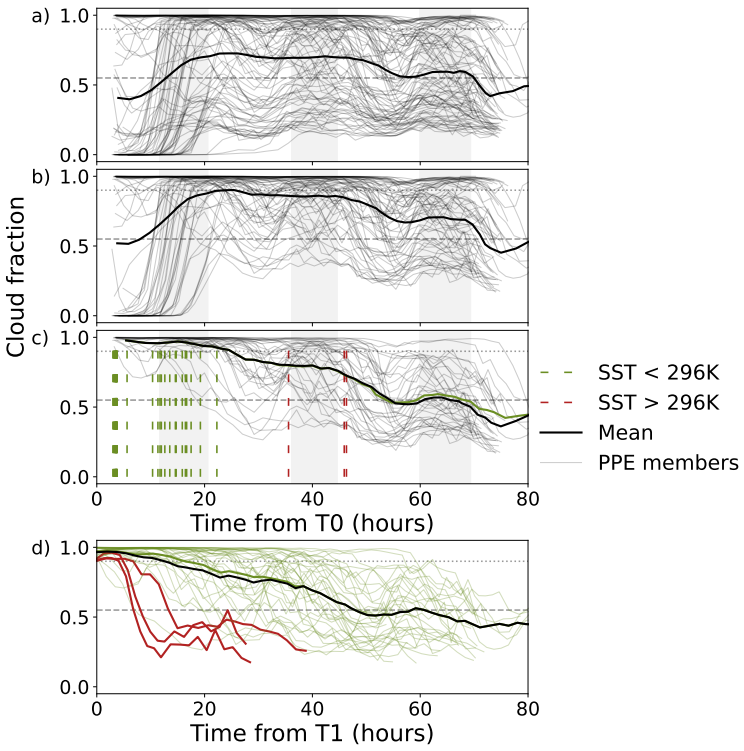

Figure 4.6: Cloud fraction timeseries for a) the whole ensemble, b) the members that form stratocumulus, c) the members that also form cumulus, and d) as in c) but aligned to the start of stratocumulus, T1. The thick, solid, black lines show the mean of the timeseries. The dashed lines show the start time of stratocumulus for each member, coloured either green or red depending on whether the SST at the start of stratocumulus is below or above 296 K. The ensemble members in d) are coloured by the SST threshold as well. The solid, green line shows the mean of the ensemble without the members with stratocumulus start SST above 296 K.

simulations that produce a transition from a stratocumulus state to a cumulus state within the three day simulation. Those that do not form stratocumulus throughout the three days are removed in Figure 4.6b (31 simulations), and those that form stratocumulus but do not transition to cumulus are removed in Figure 4.6c (30 simulations). Figure 4.6c (34 simulations) shows the subset of transitioning simulations with the subset mean. The subset mean is a similar shape to the base simulations, but the rest of the PPE members show a wide range of behaviours. On average, the cloud fraction stays near one through the first day and night, before dipping in the second day to a cloud fraction ≈ 0.75 and on the third day it crosses the cumulus threshold and stays below. A diurnal cycle can be seen in many of the members with some members dipping to as much as cloud fraction ≈ 0.4 and still recovering in the second night. Additionally some members keep a cloud fraction ≈ 1 until the third day and then transition rapidly.

While many of the simulations that transitioned formed stratocumulus within the first day, there were three simulations that only formed stratocumulus beyond the end of the second day when the SST had increased and the boundary layer became humid enough to support the cloud layer. These three simulations have an SST at least 1 K higher than the others at the start of stratocumulus and they transitioned very quickly. The subset of transitioning simulations are "epoch aligned" in Figure 4.6d by aligning time = 0 as the formation of stratocumulus for each member, and the high SST members are highlighted. This fast transition occurs despite being in areas of parameter space where you might not expect it, for example in a very shallow boundary layer with a low autoconversion rate. This subset of simulations shows that warmer initial SSTs may act to considerably speed up the transition, above meteorological conditions, which has implications for the future warmer climate. However, here these simulations have been removed from this analysis since the difference in SST at initial stratocumulus is akin to perturbing a seventh parameter, but one that was not initially accounted for in our experimental design, so the data points are not well spaced across parameter space.

4.4.3 Transition time analysis

Transition times plotted against each parameter (Figure 4.7) show that the boundary layer aerosol concentration, BL N_a, has the strongest relationship based on correlation coefficients of marginal relationships. Note that each point in these plots has a different value of the 5 other parameters so we expect marginal relationships to be generally low. Transitions faster than 40 hours (fastest 25%) only occur in aerosol concentrations, $10^{b_{aut}}$, less than 250 cm^{-3} (bottom half of perturbed range). The boundary layer specific humidity, BL q_v, has the next strongest relationship and shows that transitions slower than 68 hours (slowest 25%) only occur in simulations with specific humidity greater than 9 g kg^{-1} (top half of perturbed range), which is most likely because these clouds are thicker initially.

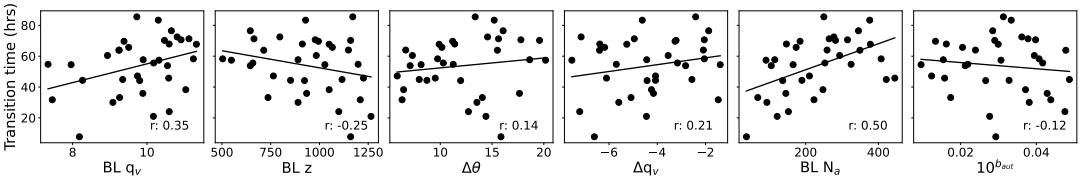

Figure 4.7: One-dimensional scatter plots against transition time for each parameter. The scatter points show the 34 simulations that transitioned within the simulation time. A line of best fit is drawn and the correlation coefficient is given in each case.

The other parameters are described in order of decreasing correlation with transition time. Deeper boundary layers, high BL z, are associated with faster transitions, in line with Eastman and Wood (2016), where decoupling occurs more easily because the boundary layer is less well mixed. Larger jumps in specific humidity, Δq_v, are associated with slower transitions. A more humid free troposphere reduces the drying from entraining above-cloud air (which would act to prolong cloud) and the rate of longwave cooling (which would lead to less cloud recovery through the night). Since we see slower transitions for a more humid free troposphere, the decrease in drying air has a larger effect than the decrease in longwave cooling. The inversion strength, $\Delta\theta$, shows a very weak positive relationship for a weak inversion (small $\Delta\theta$), as in Sandu and Stevens (2011), but shows no clear relationship for strong inversions (high $\Delta\theta$). The transition time has a slightly negative relationship with $10^{b_{aut}}$, with slow transitions occurring for low parameter values (converts to low autoconversion rates) and fast transitions for high values (autoconversion rates), which indicates higher drizzle rates deplete cloud water and hasten transitions. These are only marginal relationships, but by analysing the joint effects between factors we can understand the complexity in the drivers of transitions.

Figure 4.8 shows the transition time for all 2-dimensional parameter combinations, which allows us to build up the wider environmental conditions behind fast and slow transition times. The fastest transitions are those with low BL N_a (Figure 4.7), but they are also generally combined with deep boundary layers (panel h), high autoconversion rates (panel o) and dry inversions (panel j). The slowest transitions occur in very moist boundary layers (high specific humidity) under strong temperature inversions (panel b).

Figure 4.8 also shows the regions of parameter space that did not produce stratocumulus or did not transition to cumulus by the end of the simulation (marked with small grey dots). The majority of simulations that did not produce stratocumulus started from a dry, shallow boundary layer (low BL q_v and BL z; panel 1). Additionally, simulations with the weakest inversions also did not produce stratocumulus (bottom edge

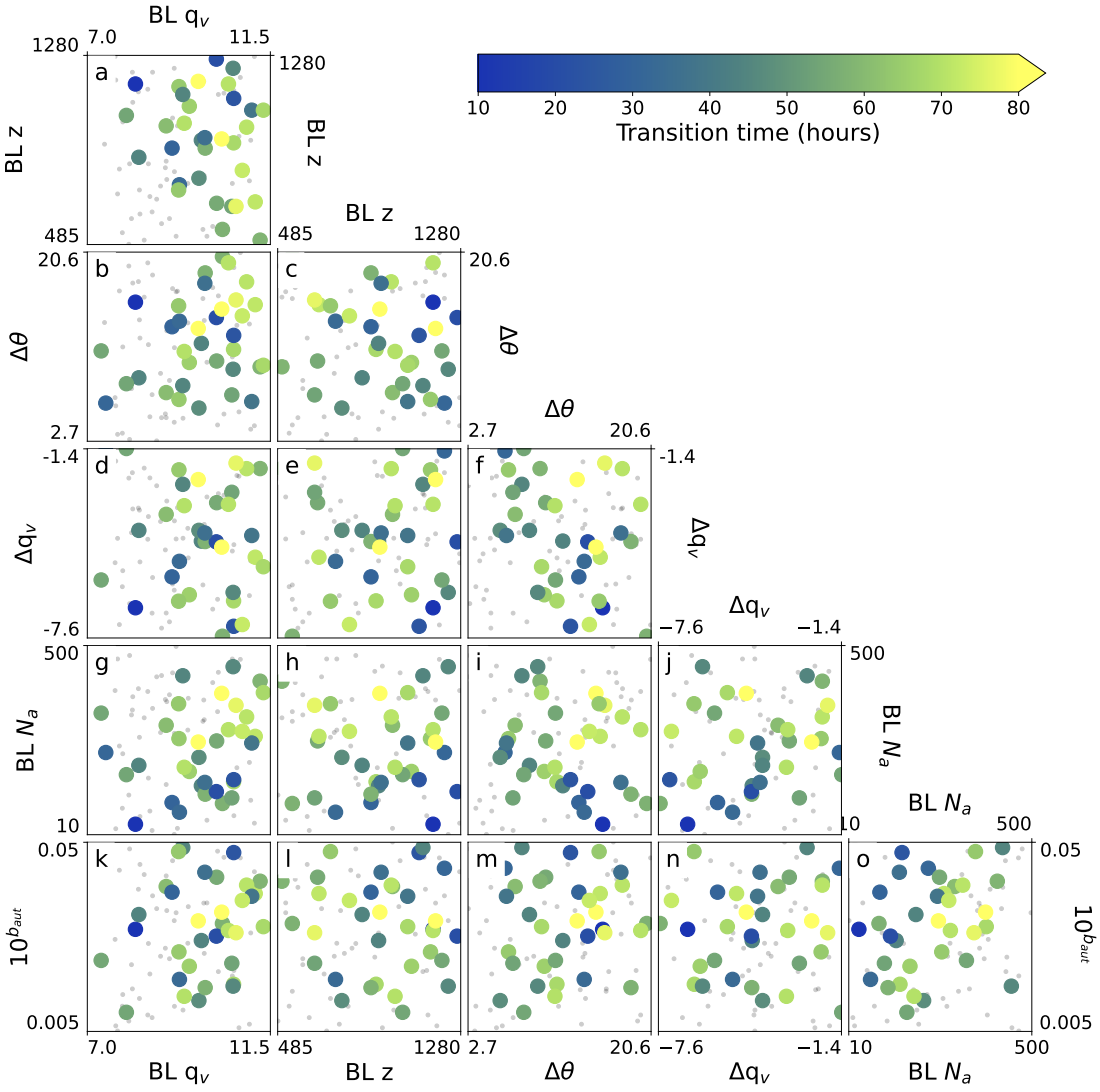

Figure 4.8: Pairwise plot showing a scatter plot of each parameter combination, coloured by transition time. Small, grey markers show the locations of the simulations which did not form stratocumulus and transition.

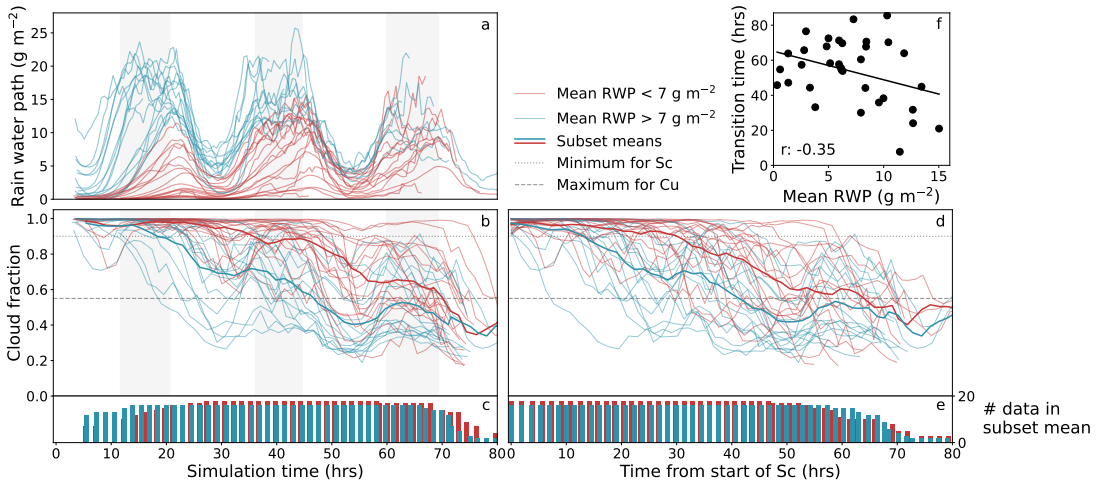

Figure 4.9: The rain water path across the ensemble. a) The domain-averaged rain water path timeseries for each member split by temporal mean rain water path greater than 7 g m^{-2} (blue) or less than (red). b) The cloud fraction timeseries as in Figure 4.6c but coloured by mean RWP. The means over each subset (high or low mean RWP) are shown in bold. c) The number of data points used in calculating the mean of each subset at each timestep in b). d) As in b) but aligned to the start of stratocumulus. e) As in c) but for d). f) A scatter of the mean RWP for each member against the transition time, with a line of best fit.

of second row and left edge of the third column). Many of these simulations produced low cloud fractions around 0.2 to 0.4.

4.4.4 Rain water path analysis

We analysed the RWP in the PPE to determine whether the drivers of the transition might have acted through a drizzle depletion mechanism. The RWP across the PPE is summarised in Figure 4.9, with the domain-averaged timeseries for each member shown in panel a. In this plot the PPE is split into "low" and "high" RWP by a temporal mean threshold of 7 g m^{-2} (approximately half of the highest member). The cloud fraction for the transitioning simulations (simulation time aligned in panel b and epoch aligned in panel d) has also been coloured low and high for RWP, with corresponding subset means. The histograms in panels c and e show the number of points being averaged over at a given time in each subset, which varies because of the different stratocumulus formation times (Section 4.4.2 and Figure 4.6).

We find that the simulations with higher RWP transitioned approximately 22 hours ahead of those with lower RWP (Figure 4.9d). Figure 4.9a shows that those with higher mean RWP produced drizzle much more in the first and second day, whereas in those with lower RWP the drizzle builds up during the simulation. In Figure 4.9b, where the timeseries are lined up with the diurnal cycle, the high RWP subset mean recovers more than the low RWP mean during the nights. This might suggest that the simulations

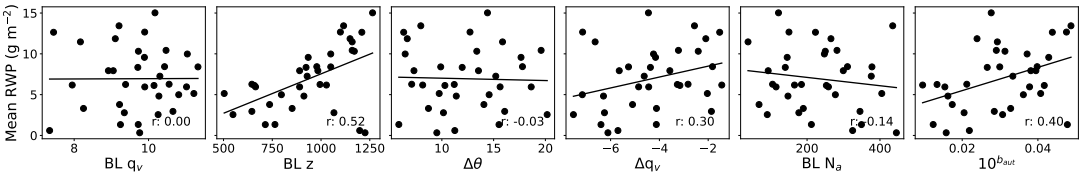

Figure 4.10: One-dimensional scatter plots against mean RWP for each parameter. The scatter points show the 34 simulations that transitioned within the simulation time. A line of best fit is drawn and the correlation coefficient is given in each case.

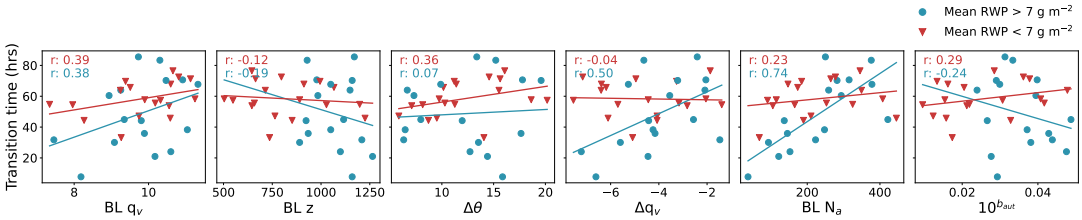

Figure 4.11: One-dimensional scatter plots against transition time for each parameter. The scatter points show the 34 simulations that transitioned within the simulation time and are coloured by high mean RWP (blue circles) or low mean RWP (red triangles). Lines of best fit are drawn and the correlation coefficients are given for each case.

with more initial rain transition to a state like open-cell stratocumulus rather than cumulus, which would enable more recovery through the night. In Diamond et al. (2022), they found that drizzle depletion caused the stratocumulus to transition to open-cell behaviour rather than cumulus, but did not determine which factors would cause one transition over the other.

Figure 4.9f shows that although the fastest transitions do have a higher mean RWP, the RWP is clearly not the only important factor determining the transition time. Rather, other factors are impacting the characteristics of the transition, such as the degree of decoupling and the ability to recover through the night.

Figure 4.10 shows that the mean RWP is most dependent on BL z and to a lesser extent, $10^{b_{aut}}$. High mean RWP results from deep boundary layers and from high autoconversion rates, as is expected. Generally, moister air above the inversion also results in a higher mean RWP (Δq_v). There is a weak negative relationship with BL N_a, with high aerosol tending towards low RWP. This suggests that although the fastest transitions have high mean RWP and low aerosol concentrations, it is the combination with deep boundary layers that is causing any drizzle depletion.

BL N_a has a much stronger relationship with the transition time if we consider only the simulations that have high mean RWP in Figure 4.11. In stronger precipitating cases, BL N_a has a bigger effect on the transition time than in weaker precipitating

cases. Δq_v also has a stronger relationship with transition time in high mean RWP simulations (more vapour available allows a faster transition). We also find that $\Delta\theta$ is much better correlated with transition time for the low RWP simulations, which is most likely due to its control on the entrainment rate, which also correlates better for low RWP simulations (see Appendix B.4).

These results show that multiple factors determine the transition time with the dominant factor depending on the wider environmental conditions. The boundary layer depth and autoconversion rate most strongly determine the amount of drizzle. Aerosol concentration controls the transition time in high-drizzle environments, whereas the inversion strength, via the entrainment rate, controls the transition time in low-drizzle environment.

4.5 Discussion

Our results show that the fastest transitions in our ensemble do occur in low aerosol environments, but the aerosol primarily has this effect when combined with deep boundary layers, high autoconversion rate and a dry inversion. We find that the amount of drizzle correlates best with the depth of the boundary layer. The simulations that have high mean rain water path (deeper boundary layer) make an average transition around 22 hours ahead of those with low rain water path (shallower boundary layer), but generally drizzle does not strongly control the timing of the transition. Rather, in deep boundary layers where there is more drizzle, the aerosol has a strong correlation with transition time, and in shallow boundary layers where there is less drizzle, the inversion strength becomes much more relevant through its strong control of entrainment rate.

The drizzle-depletion effect seen in Yamaguchi, Feingold, and Kazil (2017) could be reduced in our simulations since we have considerably less drizzle, but also many of our simulations form drizzle much earlier on, with peaks in the first or second day. This is still likely to cause a drizzle-depletion effect by removing aerosol and moisture from the cloud layer, but unlikely to be the cumulus-initiated rain that they find causes a positive-depletion feedback, since they find the cumulus generally forms from the second day onward. The cause of these differences in rain water path is most likely due to the differences in domain size or the microphysics schemes. Yamaguchi, Feingold, and Kazil (2017) did a sensitivity test with a smaller domain size (12 by 12 km^2), which is closer in size to ours than their main simulation domain (24 by 24 km^2) and also using the Khairoutdinov and Kogan (2000) microphysics scheme, rather than their bin-emulating bulk scheme. The rain water path in this test is much closer to what we see in our simulations (Figure 4.9 and their Figure 10c).

Yamaguchi, Feingold, and Kazil (2017) find that the Khairoutdinov and Kogan (2000) microphysics scheme with fixed droplet number is not capable of producing a

transition. The microphysics scheme that we use, CASIM, uses the Khairoutdinov and Kogan (2000) parameterisations for autoconversion and accretion, however we do find the transition takes place since we are using it with aerosol processing, where collision and coalescence of cloud droplets reduces the concentration of aerosol. This supports the conclusion in Yamaguchi, Feingold, and Kazil (2017) that those simulations do not transition because using a fixed droplet number does not allow rain feedbacks, and hence why previous studies have found drizzle to be only a minor effect (Sandu and Stevens, 2011; Blossey, Bretherton, and Mohrmann, 2021), and the transition time to be dominated by lower tropospheric stability and entrainment rate.

The boundary layer deepening is lower in our base simulation compared with other simulations of the same case, and this could restrict circulation and also precipitation. The maximum height of the boundary layer in our base is around 1400 m, whereas other studies have deepening up to around 2500 m (Sandu and Stevens, 2011; Bretherton and Blossey, 2014; de Roode et al., 2016; Yamaguchi, Feingold, and Kazil, 2017). The previous version of the MONC model was used in the de Roode et al. (2016) model intercomparison, and it does have the shallowest boundary layer with a maximum height of about 1800 m for the reference case (our base case), which suggests that it could be partly down to the model structure.

Where previous studies of the aerosol effect on the stratocumulus to cumulus transition have only included an accumulation mode in their simulations, we have also included Aitken and coarse modes. The Aitken buffering hypothesis of McCoy et al. (2021) has been supported by simulations in Wyant et al. (2022) that show Aitken-sized aerosol can be transported to the boundary layer where the larger particles act as cloud condensation nuclei. High concentrations of Aitken mode in the free troposphere slowed the transition from stratocumulus to an ultraclean layer, which otherwise would have occurred through aerosol removal and precipitation feedbacks. In our simulations, the concentrations of Aitken mode do not show significant depletion throughout the simulations, but this could be a small factor to consider. Additionally, we have not included a source of aerosol through the simulation whereas in reality, sea spray is a primary source of aerosol away from coastal environments. This source would have acted to slow all transitions equally since we did not perturb controlling factors, such as wind speed.

The transition time was determined using stratocumulus and cumulus thresholds for cloud fraction, but this method was limited by the bounds of the simulation time. As mentioned previously, some of the cumulus clouds may have recovered to stratocumulus after the simulation ends. Similarly for the clouds that began with stratocumulus, there is an unquantifiable amount of time before the simulation where the cloud may have been formed. These limitations likely result in noise in the data which may obscure some of the 1-dimensional relationships in this PPE analysis. A more robust adaptation

would be to spin up a base cloud before making perturbations and to have a restriction on how long the cloud must remain as cumulus before the end of the simulation. Two alternative methods could be to study the time taken for the cloud to transition from the end point of stratocumulus to the start of cumulus, or the gradients in the decline from stratocumulus.

Using cloud fraction is a reliable way to measure a transition in cloud behaviour, but it is hard to quantify whether the resulting cloud is in a cumulus state, especially in a domain of this size. It would be easier to distinguish between an end state of mesoscale cumulus organisation and open-cell stratocumulus with a larger domain. Diamond et al. (2022) found open-cell stratocumulus in their study of the transition that used a domain of a similar size, but they did not determine under which conditions the stratocumulus transitioned to a cumulus state or an open-cell state. Despite the small domain size, further analysis of the simulations in this ensemble could give insight into this problem.

The autoconversion parameter has the strongest relationship with rain water path, other than the boundary layer depth, but a weak relationship with transition time compared with the cloud-controlling factors. In many of these simulations the drizzle is only a minor part of the transition that is largely determined by other factors, however in the high rain water path simulations the correlation of the autoconversion parameter with transition time is comparable to that of the cloud-controlling factors. When uncertainty in parameterisations such as this can have such a large influence on the drizzle and timing of transition, modelling studies can produce vastly different results depending on where in parameter space the model lies. Here we have perturbed only one autoconversion parameter, but in the Khairoutdinov and Kogan (2000) parameterisation there are three uncertain parameters and there are uncertainties in the accretion parameterisation too. Additionally, how sensitive a model is to a parameter value will be affected by structural differences in models. The effects of structural differences on these sensitivities could be evaluated if other modelling groups were to replicate this work, creating a multi-model PPE.

We find that in simulations with high rain water path, the inversion strength has a negligible effect on the transition time, whereas in the low rain water path simulations it is the second strongest correlation (after boundary layer moisture). Previous studies have found the lower tropospheric stability, which is quite closely linked to inversion strength since it is the difference in potential temperature at 700 hPa and the surface, to be a major control on the timing of the transition (Sandu and Stevens, 2011). Our results suggest that this is true when drizzle is playing a minor role in the deepening-warming-decoupling mechanism, but when drizzle depletion is driving the transition, the inversion strength (and consequently the lower tropospheric stability) have less of an effect.

We may not be observing fast transitions by aerosol and drizzle in the real world because quite rare conditions are required for them. We have found in this study that particularly deep, pristine boundary layers are required to see a rain-hastened transition. It is unlikely that campaigns, particularly in the NE Pacific Ocean off the coast of North America, are going to observe such conditions and hence there are no clear observations of a low-aerosol induced rain-hastened mechanism in this region.

4.6 Conclusions

In this study, we have created a perturbed parameter ensemble from an LES model to interrogate the effect of aerosol and drizzle in the stratocumulus-to-cumulus transition. This is a novel approach to understand the processes behind the transition, and, as we show, it is essential to evaluate interactions between multiple factors to better understand the complexity of the transition drivers.

We find that aerosol concentration has the strongest relationship with transition time, where low aerosol environments produce transition times of under 40 hours. The fastest transitions also occur in deep boundary layers, under dry inversions and with high autoconversion rates. Simulations that have a high mean rain water path have an average transition time around 22 hours faster than for low mean rain water path. Deep boundary layers and autoconversion most strongly determine the mean rain water path. For simulations that have a high mean rain water path (deep boundary layer) the aerosol concentration has an even stronger relationship with the transition time, whereas for simulations that have a low mean rain water path (shallow boundary layer) the inversion strength has a stronger relationship with the transition time through its control of entrainment rate.

Due to the dependence of the transition drivers on the wider environment, it would be beneficial to do further analyses of a range of conditions rather than focusing on binary fast and slow cases. There are multiple areas of parameter space that can give the same transition time (equifinality), so analysing single cases could give only a small part of the picture.

Chapter 5

Gaussian process emulation to explore interaction of cloud-controlling factors

5.1 Abstract

The stratocumulus-to-cumulus transitions are driven by a multitude of interacting cloud-controlling factors. A deep understanding of these interactions is required to accurately represent cloud responses to climate changes in global climate model parameterisations. In Chapter 4, a perturbed parameter ensemble (PPE) analysis found the fastest transitions (under 40 hours) corresponded to low aerosol concentrations combined with deep boundary layers, high autoconversion rates, and dry temperature inversions. Here, the 6-dimensional PPE is used as training data for Gaussian process emulation, which creates a statistical representation of the relationships between the parameters and two properties of the transition: transition time and average rain water path. Using the emulators, thousands of predictions are made for the transition properties, which allows visualisation of response surfaces and quantification of parameter contributions to the outputs' variances. In low-aerosol regimes (< 200 cm^{-3}) the transition time is dominated by aerosol concentration, but outside the low-aerosol regime, the inversion strength becomes more important. For the specified realistic ranges considered here, the aerosol concentration contributes 56% and inversion strength contributes 16% of the variance in the transition time. The total interaction effects from all parameters contribute 17% of the variance. The dependency of drizzle on the parameters is studied using the average rain water path. The dependencies of rain water path on the parameters are much more linear than for the transition time. The boundary layer depth contributes 32%, aerosol concentration contributes 26%, and autoconversion contributes 20% of the rain water path variance. The interacting (joint) effects of

factors apparent in the emulators show the complexity of factors that determine the transition time, whereas the rain water path is directly determined by single factors.

5.2 Introduction

Stratocumulus clouds are sensitive to changes in their environment, such as changes in aerosol or temperature, which can drive them to transition into other cloud types leading to a decrease in cloud cover (Albrecht et al., 1995; Stevens et al., 2005b; Albrecht et al., 2019; Eastman, McCoy, and Wood, 2022). Cloud parameterisations in global climate models poorly represent these transitions due to a lack of understanding of the key drivers and the environments that cause different end states (Eastman et al., 2021; Diamond et al., 2022). As such, there are large uncertainties in the responses of stratocumulus to future climate change (Bony and Dufresne, 2005; Teixeira et al., 2011). This is concerning because stratocumulus clouds have a strong cooling effect, so reductions in their extent with warming could act to amplify the warming – a positive cloud feedback (Gettelman and Sherwood, 2016; Ceppi et al., 2017). We need to be assessing the environmental conditions surrounding these transitions to improve our process-level understanding of stratocumulus clouds.

In Chapter 4, we analysed 34 simulations from a perturbed parameter ensemble (PPE) of stratocumulus-to-cumulus transitions to investigate the roles of aerosol concentrations and drizzle in the transition. Several studies have found the occurrence of drizzle speeds up the transition (Sandu and Stevens, 2011; Diamond et al., 2022; Erfani et al., 2022), and Yamaguchi, Feingold, and Kazil (2017) found a "fast mechanism", an alternative to the deepening-warming decoupling transition, brought on by depletion of cloud water by drizzle in low aerosol conditions. Our analysis of the PPE members in Chapter 4 found aerosol concentration to have the strongest correlation with transition time out of the 6 perturbed parameters, but drizzle was primarily controlled by boundary layer depth and did not solely determine transition time. In high-drizzle environments, the aerosol had an even stronger correlation with transition time and, in low-drizzle environments, the inversion strength became more correlated than most other factors. As well as quantifying parameter correlations with transition time we analysed the parameter combinations that corresponded to fast transition times using multiple visualisation methods but the ensemble data were very sparse (only 34 parameter combinations in the 6-dimensional space). In sparse data in multiple dimensions, interpretations can be strongly influenced by single points. Statistical emulation is designed to overcome this limitation.

Using Gaussian process emulation we can form a statistical representation of the 6-dimensional relationship between the perturbed parameters and transition properties. Gaussian process emulators allow us to make predictions for any combination of

parameter values, which will fill all of the 6-dimensional space, and allow us to quantify the contributions from each parameter to the variance in the model output. In Chapter 3, we emulated a 2-dimensional parameter space of perturbed free-tropospheric cloud-controlling factors. We proposed and tested a method for incorporating the natural variability of the system into the emulator build and used the resulting emulators to create response surfaces to visualise the model outputs: liquid water path and cloud fraction. The surfaces showed the interactions (non-linear joint effects) of the two parameters and that there were two distinct regimes in parameter space: one of thin and patchy yet steady stratocumulus, and another of thick growing stratocumulus with high cloud fraction. Analysing the stratocumulus-to-cumulus transition in the 6-dimensional PPE (Chapter 4) has given us some insight into the transition behaviour across parameter space, but the interactions could not be robustly quantified because of the relatively small number of simulations in the PPE. The 34-member PPE only gives sparse coverage of the 6-dimensional parameter space.

In this chapter, we apply Gaussian process emulation to the PPE of stratocumulus-to-cumulus transitions to create emulators of two characteristic properties of the transition: the transition time and average rain water path. The rain water path is used to analyse how the cloud-controlling factors affect drizzle (see Chapter 4). We produce response surfaces for each property to analyse the parameter joint effects, and use variance-based sensitivity analysis to quantify how these transition properties depend on each parameter and their interactions. The analysis focuses on three questions: 1) Which parameters are most important in determining the transition? 2) Which parameters are most important in determining the average rain water path? 3) What additional information do we gain from using emulator predictions for thousands of new parameter values that we did not have from the PPE analysis in Chapter 4?

Section 5.3 summarises some of the key information from Chapters 3 and 4, including descriptions of the nugget term calculation, validation of the emulators, and sensitivity analysis. In Section 5.4, the emulator response surfaces are used to discuss the joint effects of factors and the sensitivity analysis results are shown. Finally, in Section 5.5 these results will be synthesised and compared with those from Chapter 4.

5.3 Methods

The analysis in this chapter follows on from the PPE analysis in Chapter 4 and uses the same model simulations. In that chapter, the MONC model was used to simulate 96 perturbations to a stratocumulus-to-cumulus transition composite case (Sandu, Stevens, and Pincus, 2010; Sandu and Stevens, 2011). MONC was coupled to a bulk two-moment microphysics scheme (CASIM, Field et al., 2023) that has prognostic aerosol modes and collision-coalescence of droplets, and a two-stream radiation scheme (SOCRATES) that

Table 5.1: Parameter descriptions, symbols and ranges in parameter space.

Parameter description	*Symbol*	*Range*
BL vapour mass mixing ratio	BL q_v	7 to 11 g kg^{-1}
BL depth	BL z	500 to 1300 m
Inversion jump in potential temperature	$\Delta\theta$	2 to 21 K
Inversion jump in vapour mass mixing ratio	Δq_v	-7 to -1 g kg^{-1}
BL aerosol concentration	BL N_a	10 to 500 cm^{-3}
Autoconversion rate parameter	b_{aut}	-2.3 to -1.3

simulated a diurnal cycle (Manners et al., 2015; Edwards and Slingo, 1996). Full details of the models can be found in Chapter 2, and the model setup, the perturbations and the range of cloud behaviour during the simulations can be found in Chapter 4.3. The table of parameters and perturbed ranges has been copied here for reference (Table 5.1). In this chapter, we also use Gaussian process emulation, as detailed in Chapters 2 and 3.

5.3.1 Nugget term

To calculate a nugget term for the emulators, additional simulations were made to produce initial-condition ensembles, as in Chapter 3. Four points from the PPE were chosen to cover a range of transition time output values at which to repeat the simulations. These simulations all formed stratocumulus initially and transitioned by the end of the simulation, with transition times of 19, 24, 40 and 71 hours. As in Chapter 3, each simulation was repeated four times with the same initial profiles but with a random set of potential temperature fluctuations (between 0 and 0.1 K at random heights) at the start of the simulation (figure 5.1a). There is one exception where the 71-hour simulation was only repeated three times.

Following the method in Chapter 3, the initial-condition ensemble residuals (the difference between member values and the ensemble mean), or "model" residuals, were calculated for the transition time and average rain water path (e.g., figure 5.1b). For each output, the residuals from all initial-condition ensembles were then combined into sets with a total of 19 sample points (e.g., figure 5.1c, pink histogram). Our assumption from Chapter 3 is that all these residuals are sampled from one distribution for the whole parameter space so they can be combined in this way, see Figure 3.9.

The nugget terms were evaluated by comparing the model residuals against the "emulator" residuals (the difference between model data and emulator predictions at training points) in the same way as in Chapter 3 (Figure 5.1). The variance does increase slightly with the mean for both transition properties, however, the variance of the model residuals was found to be an appropriate nugget term for the emulator without normalisation (which was required in Chapter 3). We did normalise by the mean

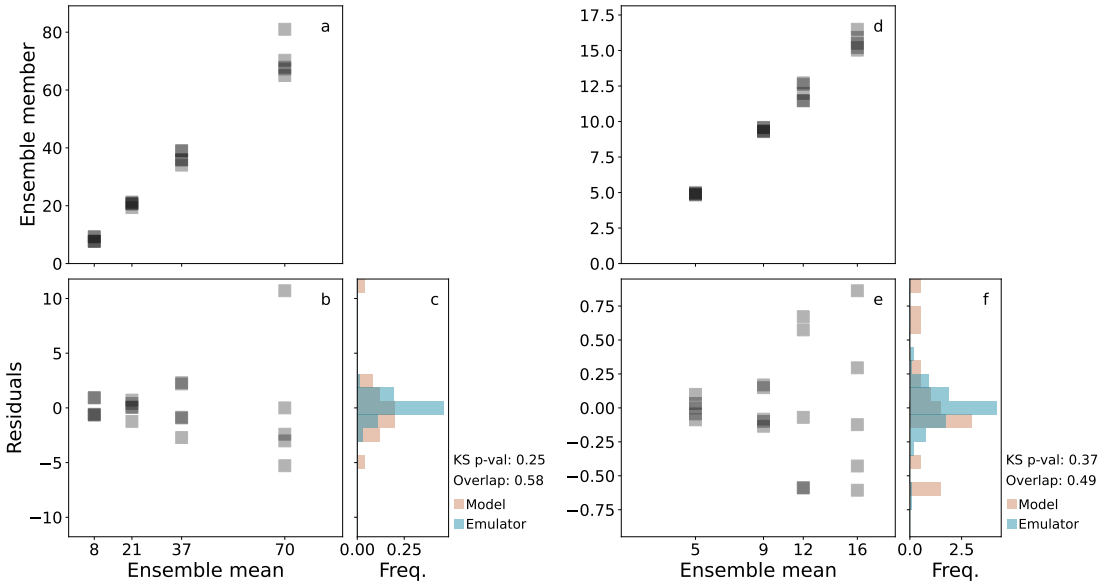

Figure 5.1: Initial-condition ensemble residuals and nugget term evaluation. a-c) Transition time and d-f) rain water path. a, d) Values of ensemble members for each ensemble mean b, e) residuals for each ensemble, c, f) histograms of model and emulator residuals (see text for definitions).

(not shown) and it also produced a suitable emulator, but we chose to use the unnormalised residuals to avoid the extra approximations incurred from finding a multiplier (Chapter 3.6). Using these variances as nugget terms, the distributions of emulator residuals are similar to the distributions of model residuals, as seen in Figure 5.1c and f. The emulator residuals include the training points at which ensembles were created, but at those points the original model outputs were replaced with the ensemble means before the residuals were calculated.

Although the nugget terms required here are quite small in comparison to the data (17% and 2% of the mean transition time and rain water path data), they do create smoother, more deterministic surfaces. This difference is not as clear as in Chapter 3 because we are showing the averaged response surfaces, so some bumps are smoothed in the averaging. However, the rain water path emulator average response surface is particularly improved with a nugget term. See Appendix B.4 for an evaluation of the emulators without nugget terms.

5.3.2 Emulator validation

The emulators of transition time and rain water path were validated using the leave-one-out method, which allowed more data to be used to create the emulators than if we used a separate validation subset. This was chosen because the set of planned training data was already reduced by the number of simulations that failed to form

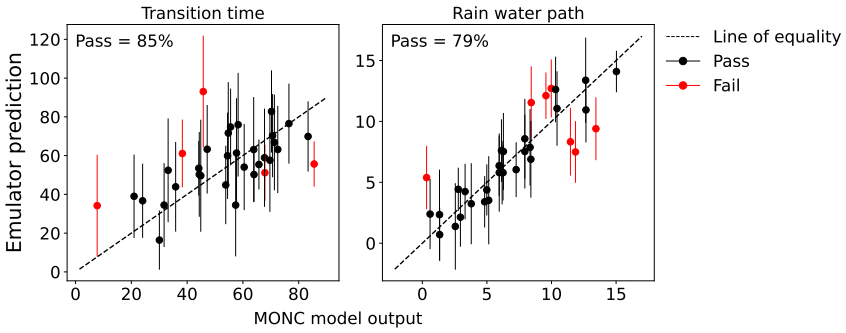

Figure 5.2: Emulator validation using the leave-one-out approach. Transition time is shown on the left and rain water path on the right. Points show the model output against the emulator-predicted values for each training data point that has been left out of the emulator training set in turn. Lines show the upper and lower 95% confidence bounds. Black points are where the model output data lies within the confidence bounds (pass) and red points are where this is not the case (fail).

stratocumulus and failed to transition to cumulus. The leave-one-out validation takes the whole set of training data and creates an emulator from all but one of the data points. That emulator is then used to predict the value for the left-out point. This is repeated one by one for each point and the differences between the predicted values and the actual values are used to gauge how reliably the emulator can reproduce model output.

The leave-one-out validations in Figure 5.2 show that the training points were predicted within the 95% confidence intervals for 85% and 79% of the points for transition time and rain water path. This is an acceptable degree of accuracy considering we only have 34 points in a 6-dimensional space. We additionally validated the emulators by calculating the ratio of the standard deviation of the mean values at the training data (a measure of variation in emulated output) to the mean of the standard deviation of those points (the uncertainty in emulated values). For both emulators, this ratio is larger than 1, which tells us the function changes more than the underlying emulator uncertainty. If the ratio was less than 1, the emulator uncertainty would be too large compared to changes in the function, so it would not be a useful approximation of the relationship.

The emulators were built again after validation to include all 34 of the points. Every point included carries information about a new part of parameter space because we used a Latin hypercube to design simulations. So including all the points ensures we have as much model information as possible. The emulators could be improved with more training data, but this validation shows that they predict model output with sufficient accuracy for us to gain important insights into the processes that drive transitions.

5.3.3 Sensitivity analysis

Variance-based sensitivity analysis was used to quantify the most "important" parameters by their contribution to the variance of the output. That is, variation in the most important parameter causes the largest variation in the output of interest. This analysis follows the method described in Chapter 2.2.1 and applied in Chapter 3.

5.4 Results

Here we discuss the response surface and sensitivity analyses of the transition time model output followed by the rain water path model output. The emulators were used to make predictions for a 1000-point Latin hypercube and a 1 million-point 6-dimensional grid, and these are shown in pairwise plots like the PPE in Chapter 4. The Latin hypercube predictions are denser in parameter space than the 34-member PPE, but still sparse enough to allow the output variation to be seen through all 6 dimensions (even when projected onto two of the dimensions). It should be borne in mind that when plotted as 2-dimensional projections in this way, each of the 1000 points has different parameter values in the other 4 dimensions. Using 1000 points here is sufficient to fill the 2-dimensional plots. However, the 1 million-point grid gives us enough points (10 values along each dimension) to create averaged response surfaces, where we hold the other 4 hidden parameter values constant at their average values in each 2-dimensional plot.

5.4.1 Transition time analysis

The transition time from stratocumulus to cumulus was calculated as the time between when cloud fraction was 0.9 to when it fell below 0.55 and stayed below that threshold until the end of the simulation, as in Chapter 4.

Latin hypercube predictions

The 1000-point Latin hypercube predictions for transition time, shown in Figure 5.3, fill the plot giving far more information than the raw PPE data and immediately begin to inform us about the subtleties in variation across parameter space. Some of the 2-dimensional plots show a clear pattern, which means the transition time varies consistently for those two parameters through the other dimensions not shown in that panel (e.g., panels i and o). Other plots show less clear variations of the transition time for the two parameters, which suggests there is no obvious dependence on these two parameters, or the effects of the four hidden parameters are dominating (e.g., panels a and d). There is a strong pattern in the boundary layer aerosol concentration, BL N_a, with low BL N_a producing the fastest transitions (panels g-j and o). The inversion strength ($\Delta\theta$ in panels b, c, f, i, m) and the autoconversion parameter ($10^{b_{aut}}$ in panels

k-o) also show patterns, which are particularly clear in combination with BL N_a (panels i and o).

Average response surfaces

The strength of output dependencies on each parameter and the interactions between parameters can be more easily interpreted in the averaged 1 million-point response surfaces in Figure 5.4. This figure also shows the training data distribution and their values. It is not expected that these data would fit the contoured surfaces very closely since they are single points in 6 dimensions and the surfaces are averaged in the 4 hidden dimensions. However, where single points do correspond to values on the 2-dimensional surface shows that those 2 parameters are important in determining the output and the hidden parameters contribute little. We can also infer that the emulator may be performing less well where the training data are sparse. For example, in the lower values of the boundary layer specific humidity some of the simulations did not form stratocumulus, or only did so for a high sea surface temperature, and were removed. This could be why the emulator finds almost no dependency on the boundary layer specific humidity, so the mean function relaxes back to the prior specification. Significant interactions between parameters can be identified by the curved surfaces (e.g., panels c, i and o), whereas surfaces that look linear (e.g., panels e and f) have negligible interaction effects.

The transition time has the strongest dependencies on aerosol concentration, BL N_a, jump in potential temperature, $\Delta\theta$, and the autoconversion parameter, $10^{b_{aut}}$. Most of the panels show at least linear joint effects and several show non-linear joint effects (interactions, shown by the curvature) between parameters. Here we analyse the dependencies seen in the response surfaces. We suggest mechanisms from relevant studies since identifying specific mechanisms with 6 perturbed parameters would require much greater analysis and many emulators for other diagnostics, such as entrainment and decoupling.

Beginning with the boundary layer specific humidity, BL q_v, on the left of the figure (panels a, b, d, g, k), the transition time does not have a strong dependency on this parameter. The transition time is nearly invariant to changes in BL q_v, though there is a weak control showing that more humidity in the boundary layer results in longer transitions and vice versa. Moist boundary layers allow thicker clouds to form, which would then take longer to dissipate through entrainment (Zhou and Bretherton, 2019). Some weak interactions (curvature) can be seen with the boundary layer depth (BL z), $\Delta\theta$, and $10^{b_{aut}}$ (panels a, b, k).

The boundary layer depth, BL z, shows that deep boundary layers transition faster than shallow ones (panels a, c, e, h, l). This is a stronger control and is seen even

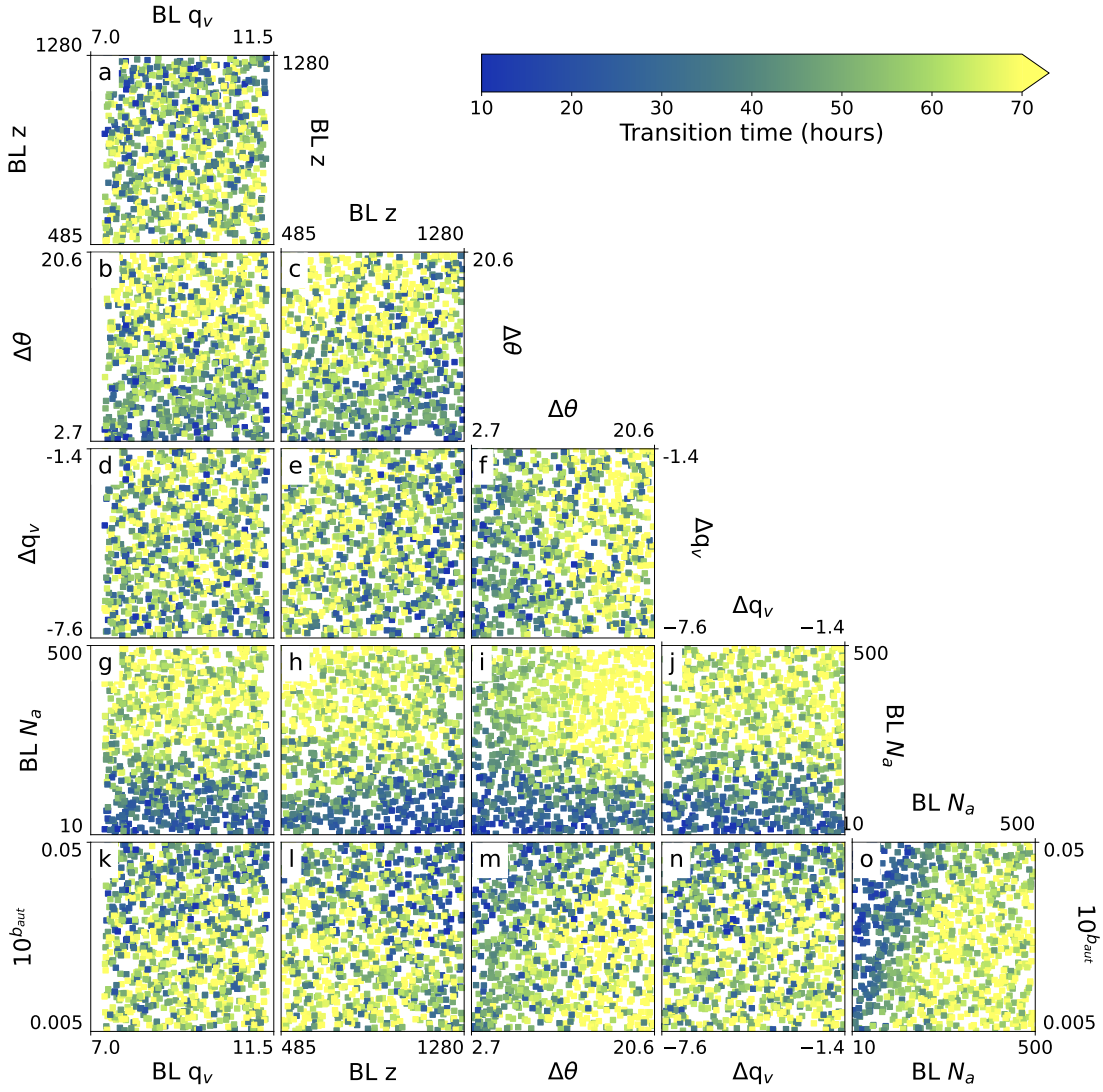

Figure 5.3: Transition time emulator sampled with a 1000-point Latin hypercube. a-o) shows each 2-dimensional combination of the six factors perturbed in the ensemble across the chosen ranges (see Chapter 4 for full details on the design of the ensemble).

more clearly where there are interactions with $\Delta\theta$, BL N_a and $10^{b_{aut}}$ (panels c, h, l). Wood and Bretherton (2006) showed that deep boundary layers are more likely to be decoupled, and since decoupling is part of the classic transition mechanism this stage could be hastened when beginning in a deeper boundary layer. (Eastman and Wood, 2016) found that clouds in deep boundary layers are prone to break up, and they also suggested it is through decoupling.

The inversion strength, $\Delta\theta$, shows a very strong control of faster transitions for weak inversions (small $\Delta\theta$) and slower transitions for strong inversions (large $\Delta\theta$) (panels b-c and f, i, m). There are clear interactions with BL z, BL N_a and $10^{b_{aut}}$ (panels c, i, m). Several studies have found the inversion strength, or the closely related lower tropospheric stability, to be a key control on the transition time (Mauger and Norris, 2010; Sandu and Stevens, 2011; Eastman and Wood, 2016). These studies showed that clouds under weak inversions are prone to break up or that clouds under strong inversions persist. A strong inversion traps moisture in the boundary layer and reduces boundary layer deepening and decoupling, which is a key stage in the classic transition.

The jump in specific humidity, Δq_v, has a very weak control on transition time showing faster transitions for drier air above the boundary layer (panels d-f, j and n). Zhou, Kollias, and Lewis (2015) found that the entrainment of dry warm air at cloud top was a major driver of decoupling through sudden drying of the boundary layer and subsequent rising of the condensation point. Eastman, Wood, and Kuan Ting (2017) also found this pattern but suggested that more vapour above the cloud increases the downwelling longwave, which offsets some of the longwave cooling, reducing mixing and boundary layer deepening. However, Sandu and Stevens (2011) found that transitions were faster for increased downwelling longwave radiation, so our results suggest the strong relationship that Zhou, Kollias, and Lewis (2015) and Eastman, Wood, and Kuan Ting (2017) found could be buffered by this effect.

The aerosol concentration, BL N_a, shows the strongest control with faster transitions for lower BL N_a (panels g-j, o). BL N_a below 200 cm^{-3} are the only areas where the transition time is predicted to be below 40 hours. There are clear interaction effects in panels BL z, $\Delta\theta$, Δq_v and $10^{b_{aut}}$ (panels h, i, j, o). Yamaguchi, Feingold, and Kazil (2017) and Diamond et al. (2022) found that low aerosol environments caused drizzle depletion of moisture and aerosol in the boundary layer. The deeper analysis in Yamaguchi, Feingold, and Kazil (2017) found that in their simulations it was specifically cumulus drizzle being lifted to the stratocumulus layer and initiating a rapid depletion. Erfani et al. (2022) found that adding aerosol into a clean case caused a delay in the transition, but adding aerosol into a polluted case had little effect on the transition time.

The autoconversion parameter, given as $10^{b_{aut}}$ here to be uniformly spaced through

the range (see Chapter 4), shows a pattern for faster transitions at higher values (which converts to higher autoconversion rates) in panels k-o. There are interactions with BL z, $\Delta\theta$ and BL N_a (panels l, m and o). Higher autoconversion rates would also incur a drizzle-depletion effect as already discussed. In addition to the previously mentioned studies, Eastman and Wood (2016) found a small, non-linear effect where precipitation sustains cloud cover in shallow boundary layers but promotes cloud breakup in deep boundary layers. The interaction with BL z in panel l agrees with their suggestion that in the shallow case, precipitation creates stronger overturning circulation, but in the deeper case it deprives the stratocumulus layer of moisture when it is also cut off from the ocean source.

The response surface is visualised further in the three most important dimensions in Figure 5.5: BL N_a, $\Delta\theta$, and $10^{b_{aut}}$. The 10 slices at different BL N_a values give a 3-dimensional picture of how transition time varies with all three parameters. The panels i, m and o are the same as in Figure 5.4. Panel m is the average of the 10 panels and panels i and o give BL N_a with $\Delta\theta$ and BL N_a with $10^{b_{aut}}$. For BL $N_a < 100$, the transition time is very low and almost invariant to the other two parameters. As BL N_a increases, there are interaction effects between $\Delta\theta$ and $10^{b_{aut}}$. For BL $N_a > 300$, $\Delta\theta$ and $10^{b_{aut}}$ have almost linear joint effects which become mostly invariant to BL N_a. This gives even more insight into the low-aerosol regime. For very low aerosol concentrations, the aerosol dominates all effects so the drizzle-depletion occurs in a wide range of conditions. As the aerosol increases, the transition time becomes more dependent on the other two factors, so processes affected $\Delta\theta$ begin to interact, such as entrainment. At higher aerosol concentrations, the transition time becomes almost entirely dependent on the linear combination of $\Delta\theta$ and $10^{b_{aut}}$, which could reflect the fact that adding aerosol into already polluted clouds has a smaller effect than in clean clouds.

Sensitivity analysis

The transition time sensitivity analysis, shown in Figure 5.6, quantifies the effects described above in terms of two numbers: the main effect and interaction effect. As defined earlier, the main effect is how much of the variance in the transition time is due to the variance in the individual parameter and the interaction effect is the portion of the variance that cannot be explained by linear combinations of the individual parameters, and is attributed to the interactions between parameters. The BL N_a main effect has the largest contribution to the variance in the transition time of 56%. The $\Delta\theta$ main effect contributes 16%, b_{aut} contributes 13%, BL z contributes 6%, Δq_v contributes 1% and BL q_v contributes less than 1%. The interactions from each factor contribute a total of around 8% of the variance, so the total interactions are more important than several of the parameter main effects. The dependence on the interactions between pa-

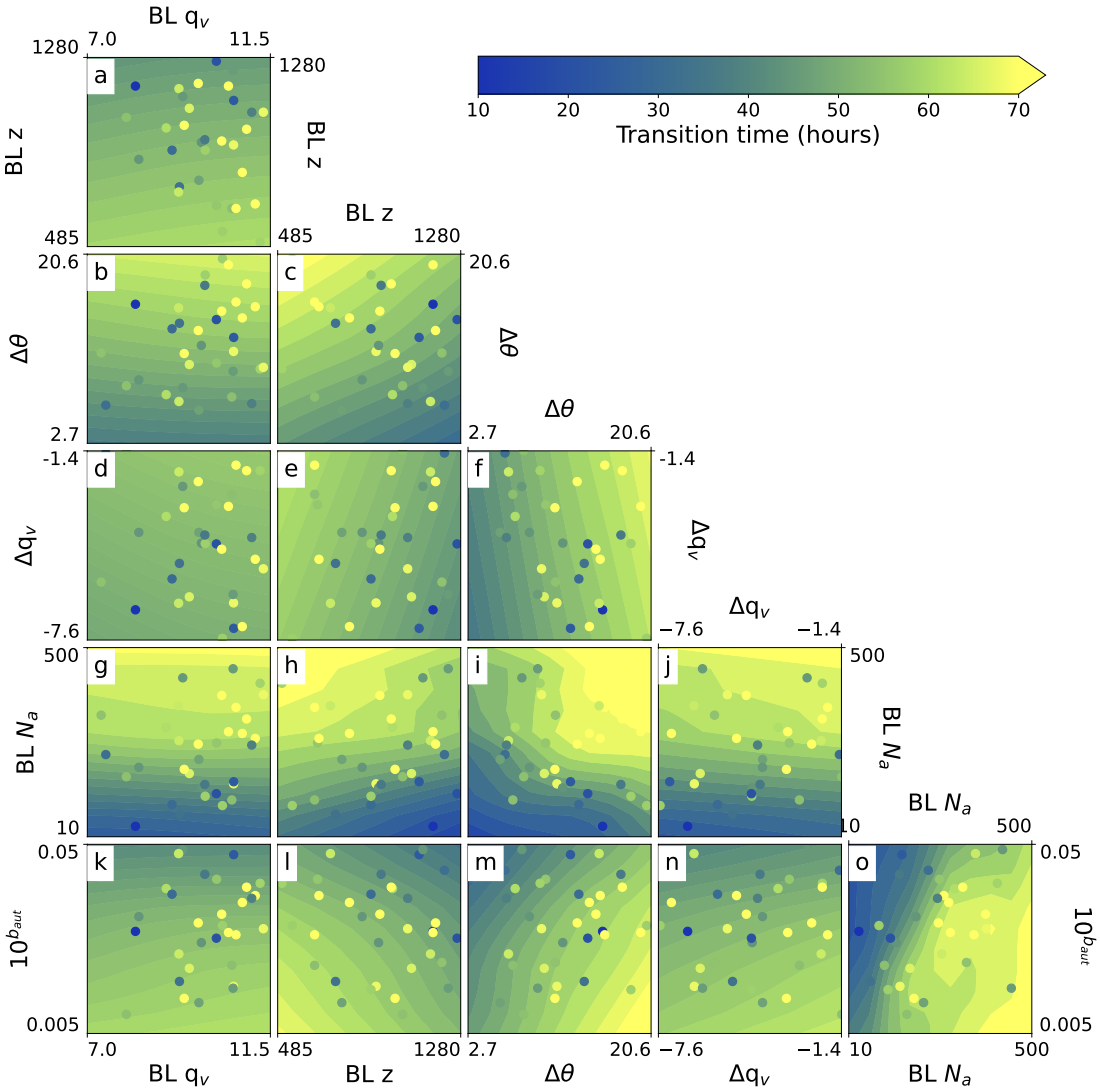

Figure 5.4: Transition time response surface sampled with a 1-million point 6-dimensional grid and averaged across hidden dimensions. a-o) shows each 2-dimensional combination of the six perturbed factors averaged in the four dimensions not shown. Coloured points show the training data distribution and values.

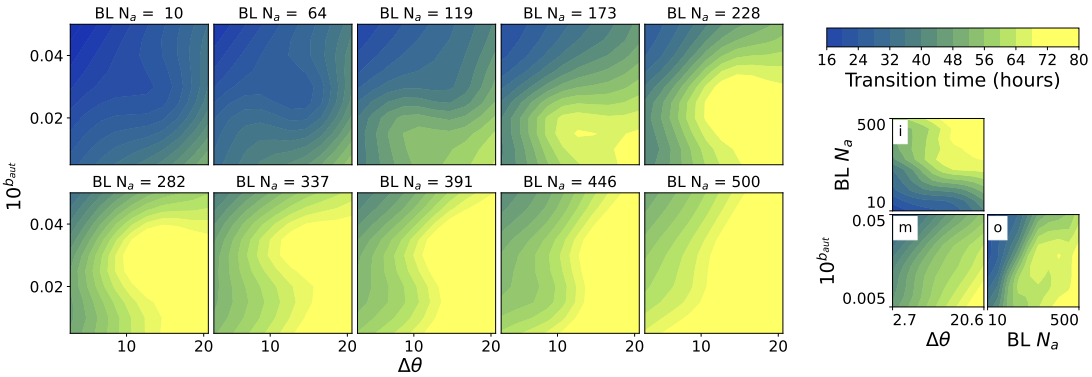

Figure 5.5: Transition time response surface slices. Averaged response surfaces for 10 values of BL N$_a$ in the $10^{b_{aut}}$ and $\Delta\theta$ parameter space, averaged through the 3 remaining parameters not shown. i-o) show the relevant averaged 2-dimensional plots from Figure 5.4. i) $\Delta\theta$ vs BL N$_a$, m) $\Delta\theta$ vs $10^{b_{aut}}$, which is the mean of the 10 plots shown here, and n) BL N$_a$ vs $10^{b_{aut}}$, where slices are taken in order from the bottom of y axes to the top.

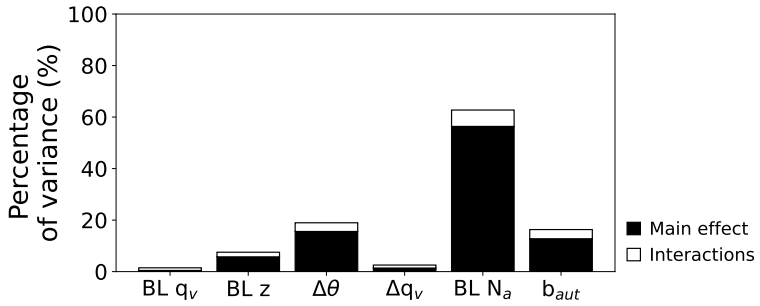

Figure 5.6: Sensitivity analysis for the transition time. Bars show the percentage contribution from each factor to the variance of the transition time. The black section shows the main effect, i.e. the individual parameter effect, and the white section shows the contribution from interactions with other parameters.

rameters demonstrates the complexity of the transition time drivers that other, more traditional, studies have overlooked.

Comparison with PPE analysis

The emulator results agree with those found in Chapter 4 that BL N$_a$ has the strongest relationship with transition time, with b$_{aut}$ also being important. However, here we have found the transition time to be strongly dependent on $\Delta\theta$ and only weakly dependent on BL z. By mapping out parameter space with predictions to make a response surface it has become clear that there is a low-aerosol regime which dominates control of the transition time. In the high-aerosol regime, the aerosol impact on transition time is less strong and there are larger interaction effects, with both the inversion strength and the autoconversion parameter influencing the rate of transition.

5.4.2 Rain water path analysis

The rain water path model output for the emulator is the rain water path averaged over the transition time (Chapter 4.4.4).

Averaged response surfaces

The averaged response surfaces for the rain water path are shown in Figure 5.7. The linear contours make it immediately clear that there are fewer interaction effects compared with the transition time. BL z has the strongest control over rain water path with high rain water paths in deep layers (panels a, c, e, h, l), which has been found in many previous studies (Bretherton et al., 2010; Eastman and Wood, 2016; O, Wood, and Bretherton, 2018). BL N_a has a strong control with high aerosol producing less rain through precipitation suppression (Albrecht, 1989) (panels g, h, i, j and o). Additionally, $10^{b_{aut}}$ has a strong control as it is directly linked to the amount of precipitation formed (panels k-o). For both specific humidity parameters, there is higher rain water path for higher humidity since vapour is available for condensation (BL q_v: panels a, b, d, g, k and Δq_v: panels d, e, f, j, n). $\Delta\theta$ shows slightly higher rain water paths under weaker inversions (panels b, c, f, i, m), possibly because weaker inversions are more likely to rise and create deeper boundary layers, which generally drizzle more.

Sensitivity analysis

Again, the sensitivity analysis of the rain water path emulator in Figure 5.8 quantifies the effects described above and we find that the variance is more widely influenced by all the parameters rather than being dominated by one, as with the transition time. The main effect of BL z contributes the most (32%) to the variance in the rain water path. This is followed by the main effects of BL N_a that contributes 26%, b_{aut} that contributes 20% and both specific humidity parameters at about 9%. The main effect of $\Delta\theta$ contributes less than 1%. The interactions contribute about 2% of the variance in the rain water path, so they are of little importance in comparison to the three most important parameters. This shows that the rain water path is determined more directly by single factors, rather than interactions between them.

Comparison with PPE analysis

The emulator results for the rain water path broadly agree with the PPE analysis in Chapter 4 with BL z being the most important factor, though here there is less of a distinction between the dependency on it and aerosol. By densely sampling the parameter space we have been able to more fully appreciate the relative importance of parameter effects, rather than being directed by a few sparse points. The $\Delta\theta$ has very little effect on the rain water path, which also agrees with Chapter 4 where we found

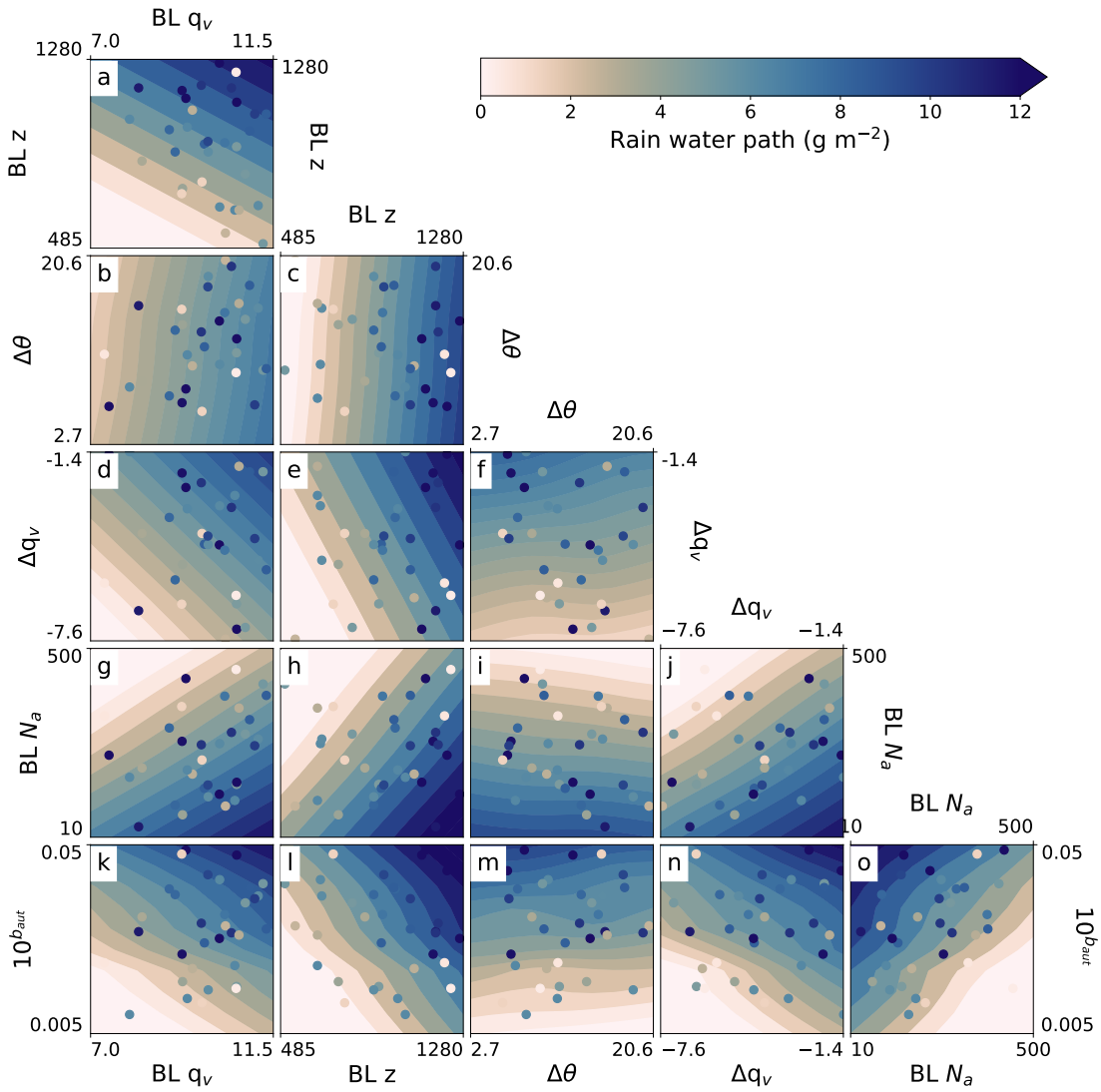

Figure 5.7: Average rain water path response surface sampled with a 1-million point 6-dimensional grid and averaged across hidden dimensions. a-o) shows each 2-dimensional combination of the six perturbed factors averaged in the four dimensions not shown. Coloured points show the training data distribution and values.

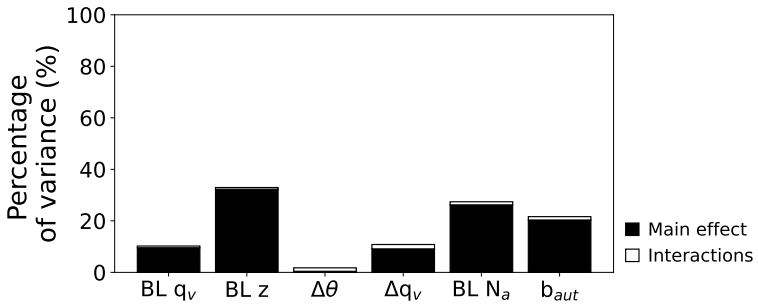

Figure 5.8: Sensitivity analysis for the rain water path. Bars show the percentage contribution from each parameter to the variance of the rain water path. The black section shows the main effect, i.e., the individual parameter effect, and the white section shows the contribution from interactions with other parameters.

it only affects the transition through entrainment, which only has a strong control in environments that have a low rain water path.

5.5 Discussion and conclusions

We have used a PPE of stratocumulus-to-cumulus transition simulations as training data for Gaussian process emulation of two model outputs: transition time and average rain water path. These emulators were used to determine which parameters, out of the six perturbed, are most important in determining the output values, through visualisation of response surfaces and variance-based sensitivity analysis.

We have gained a lot of information about the 6-dimensional parameter space from creating emulators of the 34-member PPE. Firstly, we have been able to densely sample the parameter space with up to 1 million points, from which we have created response surfaces that we can visually inspect to understand the relationships between parameters and the transition properties. These surfaces clearly show which parameters have only individual effects and which have interactions with other parameters. Also, the gradients of the surfaces intuitively inform us how strong the dependency of the output is on each parameter compared with the others. Secondly, sensitivity analysis, which samples the parameter space 1000 times per parameter, actually quantifies those dependencies by calculating the percentage of the variance in the output attributed to each parameter in their main effect and their interactions. Thirdly, through analysing the response surfaces, we have been able to identify that there are regimes of cloud behaviour (sensitivity to the controlling factors) that depend on specific combinations of multiple parameter values.

A much deeper analysis of parameter space has been achieved through the dense sampling with the emulator compared with the analysis in Chapter 4 of the raw PPE data. In both chapters, the parameter with the strongest control on transition time was

aerosol concentration and the parameter with the strongest control on the average rain water path was boundary layer depth. For the transition time, the PPE analysis found the boundary layer specific humidity, boundary layer depth and jump in specific humidity had the next largest correlations, with inversion strength and the autoconversion parameter having the smallest correlations. Here, however, we have found the opposite. The inversion strength and the autoconversion parameter have much stronger controls than the other three parameters. Additionally, we have identified that there are key interactions between aerosol concentration, inversion strength, the autoconversion parameter, and boundary layer depth. For the rain water path, the PPE analysis found the autoconversion parameter and jump in specific humidity to have the next largest correlations, with only a small correlation with aerosol and negligible with boundary layer specific humidity and inversion strength. Here, the emulator analysis has shown the rain water path has stronger dependence on aerosol and the boundary layer specific humidity.

The emulator results are a closer fit with the vast majority of stratocumulus-to-cumulus studies, which have found the lower tropospheric stability (closely related to the jump in potential temperature) to be the primary control on the transition time (Sandu and Stevens, 2011; McGibbon and Bretherton, 2017; Bretherton et al., 2019). We were able to identify that the jump in potential temperature was important for the transition time using the PPE data, but only when we split the dataset by rain water path. However, using the emulator to approximate aspects of the model output and create thousands more points in parameter space, the jump in potential temperature shows a clear relationship in the response surfaces and is found to be the second largest main effect in the sensitivity analysis. Unlike other studies before, which have often neglected aerosol, we have found that there is a strong interaction between jump in potential temperature and aerosol concentration on transition time. In low-aerosol regimes (below 200 cm^{-3}) the aerosol concentration is most important for transition time, but in high-aerosol regimes, the jump in potential temperature is most important. The response surfaces were crucial for discovering this regime split as the sensitivity analysis alone does not give such detailed information.

Our results tell us that the transition time is a complex property to understand, with the interactions between different environmental factors being important. Not only is this shown in the response surfaces, but also by the contribution of the interactions to the variance, quantified with sensitivity analysis as 17%, which is larger than all but the aerosol main effect. Many modelling studies have found differing results on the major transition time controls when carrying out one-at-a-time sensitivity tests (Sandu and Stevens, 2011; van der Dussen, de Roode, and Siebesma, 2016; Yamaguchi, Feingold, and Kazil, 2017; Bretherton et al., 2019; Zheng, Zhang, and Li, 2021; Erfani et al., 2022), and observational studies have struggled to untangle the meteorological

controls (Eastman and Wood, 2016; Sarkar et al., 2020). Our results suggest that the problem is too complex to understand with singular perturbations because the interactions between parameters are too important to neglect. Conversely, the rain water path shows only linear effects in the response surfaces and interaction effects contribute less to the variance than most of the parameter main effects. This shows that several parameters are important but their individual controls are additive.

Emulating with a nugget term absorbs noise from experiment limitations as well as accounting for natural variability. The raw PPE data were potentially made harder to interpret because the transition time data had some noise from including transitions that occurred near the end of simulation time, where we could not guarantee that the cloud remained in a cumulus state. On running the initial-condition ensemble simulations, one of the extra simulations recovered for around 10 hours before transitioning to cumulus, which gave a slightly larger variance in the residuals. In this case, the nugget term absorbs not only the natural variability from the model but also some of the noise incurred by the experiment design.

Choosing which single model output value to emulate from such a large and complex process can influence the results. For example, there is no accepted definition of "transition time" that is appropriate for all conceivable cloud development histories. We chose to define the start of the transition at the formation of stratocumulus. However, we could have defined it from the start of the simulation. We chose this definition to be able to compare more closely with studies that have followed a Lagrangian trajectory approach starting from stratocumulus decks, but this choice had the consequence of altering the "initial" profiles of the perturbed parameters. The emulator has no knowledge of the model other than the training data, which is the set of perturbed inputs and the corresponding values for an output of interest. Thus, it is crucial to remember that the usefulness of the emulator is dependent on the definition of the output. With appropriate definitions, we believe PPEs and emulation are incredibly useful tools with an entirely unique approach to cloud process understanding, which we can learn from in tandem with more classical approaches.

Chapter 6

Summary and concluding remarks

This thesis has explored the use of perturbed parameter ensembles (PPEs) and Gaussian process emulation for understanding stratocumulus cloud responses to changes in cloud-controlling factors. These techniques are well suited for studying clouds, which are complex systems of interacting processes where perturbing one factor at a time may only tell part of the story. For example, take the effect on liquid water path from adding aerosol to a cloud. Ackerman et al. (2004) found that the liquid water path only increased with aerosol when the free-tropospheric air was very humid, or droplet concentrations very low, such that sufficient precipitation was reaching the surface. There is a "joint effect" between aerosol and free-tropospheric humidity on the liquid water path. Using a PPE we have been able to identify complexities such as this, which have been missed in more traditional studies that only study factors in isolation.

In Chapter 3, we first used these techniques on simulations of a temporally stable, nocturnal stratocumulus cloud from which we perturbed two properties of the free troposphere to investigate cloud behaviour around the break-up threshold for cloud top entrainment instability. In Chapter 4, we considered the stratocumulus-to-cumulus transition and perturbed six cloud-controlling factors to assess how they jointly affected two properties of the transition under different meteorological conditions and determine whether a drizzle-depletion mechanism exists, as previously proposed. The behaviours seen across the second ensemble were so extensive that we began by analysing the effects of individual factors in the PPE data. Timeseries analysis of individual PPE simulations was used to understand how best to define emulatable model outputs related to the transition timescale. In Chapter 5, we used Gaussian process emulators to sample the parameter space 1 million times to thoroughly understand interactions between factors and how they jointly effect transition time and rain water path. All model

data was produced using an LES model which provided high-resolution advection of hydrometeors and aerosol populations, down to 5 m vertically and 30 m horizontally. A summary of each chapter and the key findings is presented below, followed by concluding remarks.

6.1 Summary of results

6.1.1 Visualisation of the deterministic response of stratocumulus cloud properties to free-tropospheric controls using statistical emulation

1. Densely sampling the 2-dimensional parameter space of the jumps in specific humidity and potential temperature at the temperature inversion revealed two behavioural regimes. In one regime, where the air above the inversion was dry and cool, the clouds were thin, patchy, and did not grow throughout the simulations. In the second regime, where the air above the inversion was warmer and drier, the clouds were thick with cloud fraction near 1 and grew thicker throughout the simulations. These results agree with more recent studies that cloud top entrainment instability is not a strong enough process by itself to fully dissipate clouds.

2. Unlike previous studies, however, we have mapped out how the liquid water path, cloud fraction and their tendencies depend on these two parameters, which shows the change in regime approximately aligns with the cloud breakup threshold. The change in regime exhibits steep gradients in the liquid water path and its tendency, but there are no discontinuities. The cloud fraction and cloud fraction tendency response surfaces have very shallow gradients at the regime change where the properties almost plateau. The response surfaces also show that the two parameters have non-linear joint effects on the cloud properties.

3. The cloud's natural variability was accounted for by applying a nugget term to the emulator build, which produced response surfaces that more-realistically represented the purely deterministic behaviour of the simulated cloud. A key conclusion of this new approach is that a small sample of points is sufficient to determine the appropriate magnitude of the nugget term, so long as they cover the range of model output well. Thus, estimating a nugget using this method requires only a few extra simulations yet it can greatly improve the statistical representation of the relationship between the input parameters and the output of interest. Response surfaces that are more representative of these relationships will allow the joint effects to be more thoroughly understood in terms of the physical processes.

6.1.2 A perturbed parameter ensemble analysis of the roles of cloud-controlling factors in the stratocumulus-to-cumulus transition

1. The 34-member PPE showed that aerosol concentration had the strongest correlation with transition time with low aerosol concentrations producing the fastest transitions (under 40 hours). This conclusion agrees with several studies that have found a drizzle-depletion effect in simulations of the stratocumulus-to-cumulus transition in low aerosol environments (Yamaguchi, Feingold, and Kazil, 2017; Diamond et al., 2022; Erfani et al., 2022).

2. Visualising the 6-dimensional PPE in parameter space showed that the fastest transitions (under 40 hours) corresponded to simulations with parameter combinations that also had deep boundary layers, high autoconversion rates and a dry temperature inversion. Where previous studies have only considered aerosol, or have been unable to determine a clear aerosol effect due to confounding processes, we have been able to determine that aerosol has a strong effect on the transition time relative to other cloud-controlling factors, with which there are some joint effects. We included an uncertain parameter from the autoconversion parameterisation in our PPE and found that it did not have a strong correlation with transition time in the PPE data.

3. The rain water path (a measure of drizzle) correlated best with boundary layer depth, but it did not solely control the transition time. When the PPE was split by rain water path, aerosol concentration had a stronger relationship with transition time in high-drizzle environments, and inversion strength became one of the strongest correlations in low-drizzle environments. Thus, we conclude from the PPE analysis that drizzle-depletion transitions occur in environments that have low aerosol, deep boundary layers and dry temperature inversions, but otherwise the inversion strength (via entrainment) largely controls the transition time. The fastest transitions may not be observed because these are rare conditions to find off the West coast of major continents.

6.1.3 Gaussian process emulation to explore interaction of cloud-controlling factors

1. Using Gaussian process emulation, the aerosol concentration was found to be the strongest control on the transition time. The transition time also had a strong dependence on inversion strength, autoconversion parameter and the boundary layer depth. We suggest that these four parameters influence the following processes: drizzle depletion of aerosol and moisture for low aerosol and high autoconversion rates, deep boundary layers being more likely to be decoupled; and strong inversions trapping moisture in the boundary layer and reducing deepen-

ing and decoupling. The 1-million point averaged response surfaces also showed that there are strong interaction effects between these four parameters. Previous studies have only been able to identify the individual controls of each parameter, and there has not been a clear consensus on the order of importance. Using sensitivity analysis we have quantified that interaction effects have a significant contribution to the variance in the transition time, being second only to the main effect of the aerosol concentration.

2. The rain water path was highest in deep boundary layers, low aerosol concentrations and high autoconversion rates. Many studies have found that deep boundary layers are more likely to precipitate. Aerosol most likely affects the rain water path through drizzle depletion at low aerosol concentrations and the autoconversion parameter directly controls the amount of precipitation produced. The response surfaces showed only linear joint effects and sensitivity analysis quantified the contribution to the variance of rain water path as less than most of the parameter main effects.

3. The key result agrees with Chapter 4, that the fastest transitions occur in low-aerosol environments through a drizzle-depletion effect. However, with the use of emulators in this chapter we have densely sampled the parameter space to identify linear and non-linear parameter joint effects and quantified the contributions to the variance of transition properties from each parameter. We determined that there is a low-aerosol regime (under 200 cm^{-3}) where the aerosol concentration has the strongest control on transition time, but in the high-aerosol regime (200 to 500 cm^{-3}) the inversion strength determines the transition time. Densely sampled response surfaces were crucial for identifying these regimes and the interactions between other parameters. The uncertainty in the autoconversion parameter was found to have a significant contribution to the variance in both emulators. We conclude that the transition time is a complex process determined by multiple factors with non-linear joint effects, which we have been able to identify using Gaussian process emulation.

6.2 Concluding remarks

The extent to which aerosol concentration influences the stratocumulus-to-cumulus transition has been unclear, with some LES simulations reporting that it does (Yamaguchi, Feingold, and Kazil, 2017; Diamond et al., 2022; Erfani et al., 2022), in-situ observations struggling to find a link (Bretherton et al., 2019), and satellite data showing that the relationship is complex and non-linear (Eastman and Wood, 2016). If we considered only the 1-dimensional relationships between the factors and transition properties from the PPE analysis, aerosol would be the primary control on transition

time. However, creating a PPE of transitions has allowed us to explore the effects of aerosol as one of six cloud-controlling factors (many more could be studied) and to identify their interactions using Gaussian process emulation. Unlike previous studies, we can conclude that even considering the effects of other important cloud-controlling factors, there is a low-aerosol regime where aerosol strongly influences transition time through drizzle depletion. In the high-aerosol regime, the inversion strength is the major control of transition time. Thus, we have found that aerosol has a non-linear relationship with transition time and interactions with cloud-controlling factors need to be considered.

This work follows several aerosol-cloud emulation studies where cloud-controlling factors have been perturbed (Johnson et al., 2015; Wellmann et al., 2018; Glassmeier et al., 2019; Wellmann et al., 2020), but it is the first to show parameter interactions using response surfaces of cloud properties. We have also explored several challenges of emulating cloud model output. Firstly, we accounted for natural variability in the emulator build to produce response surfaces that more-realistically represented deterministic cloud behaviour. Emulator nugget terms have not been derived from initial condition ensembles in this way before. The approach developed here, using initial condition ensembles at a few points in a PPE requires fewer simulations than previous studies that have created an ensemble at every point (Johnson, Gosling, and Kennedy, 2011), which is not computationally feasible in climate models. Secondly, we assessed how model spinup affected the perturbed parameter values and found that some evolved during the first two hours of simulation. We were fortunate that the evolved values were still well spaced along each dimension, which is a requirement for building a Gaussian process emulator. Ideally, when using emulation to further process-level understanding, perturbations should be made after spinning up to a steady cloud. Finally, due to the high sensitivity of clouds to initial conditions and the likelihood of sharp transitions in cloud behaviour based on small perturbations, we expected that there may be discontinuities in the parameter spaces we explored. Discontinuities can be a problem for Gaussian process emulation and alternative, non-stationary methods would be required in that case. However, we found that for both cases a stationary emulator approach worked, with reasonably smooth gradients between regimes, so non-stationary methods are still something to be explored.

Perturbed parameter ensembles are a hugely valuable tool, not just for process-level understanding as used here, but also for quantifying and constraining model uncertainty and identifying model structural deficiencies. In using them to understand cloud processes, there is the temptation to treat them as a large set of simulations that can be individually analysed in detail, but this is not where their strength lies. By their very nature, there are so many differences between each simulation that this is not a feasible approach. Rather, their strength comes from looking at the statistics of the whole

ensemble and understanding the joint effects of parameters. So perturbed parameter ensembles may not be suited to problems that require in-depth analysis of each simulation. For example, it would be quite difficult here to identify whether the end state of each transition was cumulus or open-cell stratocumulus. We have also found that it can be challenging to define an emulatable output that gives enough detail required to solve the problem at hand. Each emulator (in this method) requires that the output from each simulation be a single value. This is much easier when only analysing a small number of simulations, however with a PPE, defining one value that is meaningful for all the behaviours produced from every parameter combination can be the largest part of the challenge.

What has been gained and what could be gained from future emulation of the relationships between cloud-controlling factors and cloud properties? Through identifying clearly defined regimes, as we did in Chapter 3, parameterisations can be defined with different "modes" depending on the regime that the model is in. Creating these parameterisations requires good knowledge of the parameter values that define each regime, but this could provide simpler parameterisations because they only need to account for one type of cloud behaviour. From the work in Chapters 4 and 5, we have concurred with previous studies that there is a low-aerosol regime in which fast transitions take place via drizzle-depletion. This could improve cloud parameterisations by informing the model when a faster switch to a lower cloud fraction is required.

The complexities of clouds and the interactions of cloud-controlling factors are the defining challenges of cloud physics, but it is imperative that cloud responses to climate changes are represented more accurately. The statistical methods presented in this thesis are ideally suited for exploring such complexities and the joint effects of factors, which more traditional methods have struggled to untangle. As such, there is scope to extend the use of these methods to other climate-related challenges where interactions may be important, such as climate feedbacks and adjustments to aerosol forcings. Future climate changes will affect any processes studied in the present-day climate, but currently these are often treated as a separate problem to understand. PPEs allow climate changes to be added as perturbed parameters within the experiment and emulation would provide the opportunity to explore the joint effects of these changes with many drivers.

Bibliography

Abdul-Razzak, H. and Ghan, S. J. (2000). "A parameterization of aerosol activation: 2. Multiple aerosol types". In: *Journal of Geophysical Research: Atmospheres* 105.D5, pp. 6837–6844.

Ackerman, A. S., Kirkpatrick, M. P., Stevens, D. E., and Toon, O. B. (2004). "The impact of humidity above stratiform clouds on indirect aerosol climate forcing". In: *Nature* 432.7020, pp. 1014–1017.

Ackerman, A. S., van Zanten, M. C., Stevens, B., Savic-Jovcic, V., Bretherton, C. S., Chlond, A., Golaz, J. C., Jiang, H., Khairoutdinov, M., Krueger, S. K., Lewellen, D. C., Lock, A., Moeng, C. H., Nakamura, K., Petters, M. D., Snider, J. R., Weinbrecht, S., and Zulauf, M. (2009). "Large-eddy simulations of a drizzling, stratocumulus-topped marine boundary layer". In: *Monthly Weather Review* 137.3, pp. 1083–1110.

Albrecht, B., Ghate, V., Mohrmann, J., Wood, R., Zuidema, P., Bretherton, C., Schwartz, C., Eloranta, E., Glienke, S., Donaher, S., Sarkar, M., McGibbon, J., Nugent, A. D., Shaw, R. A., Fugal, J., Minnis, P., Paliknoda, R., Lussier, L., Jensen, J., Vivekanandan, J., Ellis, S., Tsai, P., Rilling, R., Haggerty, J., Campos, T., Stell, M., Reeves, M., Beaton, S., Allison, J., Stossmeister, G., Hall, S., and Schmidt, S. (2019). "Cloud system evolution in the trades (CSET) following the evolution of boundary layer cloud systems with the NSF-NCAR GV". In: *Bulletin of the American Meteorological Society* 100.1, pp. 93–121.

Albrecht, B. A. (1989). "Aerosols, cloud microphysics, and fractional cloudiness". In: *Science* 245.4923, pp. 1227–1230.

Albrecht, B. A., Bretherton, C. S., Johnson, D., Scubert, W. H., and Frisch, A. S. (1995). "The Atlantic Stratocumulus Transition Experiment - ASTEX". In: *Bulletin of the American Meteorological Society* 76.6, pp. 889–904.

Andrianakis, I. and Challenor, P. G. (2012). "The effect of the nugget on Gaussian process emulators of computer models". In: *Computational Statistics and Data Analysis* 56.12, pp. 4215–4228.

Bellon, G. and Geoffroy, O. (2016). "Stratocumulus radiative effect, multiple equilibria of the well-mixed boundary layer and transition to shallow convection". In: *Quarterly Journal of the Royal Meteorological Society* 142.697, pp. 1685–1696.

Bellon, G. and Stevens, B. (2013). "Time scales of the trade wind boundary layer adjustment". In: *Journal of the Atmospheric Sciences* 70.4, pp. 1071–1083.

Bellouin, N., Quaas, J., Gryspeerdt, E., Kinne, S., Stier, P., Watson-Parris, D., Boucher, O., Carslaw, K. S., Christensen, M., Daniau, A. L., Dufresne, J. L., Feingold, G., Fiedler, S., Forster, P., Gettelman, A., Haywood, J. M., Lohmann, U., Malavelle, F., Mauritsen, T., McCoy, D. T., Myhre, G., Mülmenstädt, J., Neubauer, D., Possner, A., Rugenstein, M., Sato, Y., Schulz, M., Schwartz, S. E., Sourdeval, O., Storelvmo, T., Toll, V., Winker, D., and Stevens, B. (2020). *Bounding Global Aerosol Radiative Forcing of Climate Change*.

Blossey, P. N., Bretherton, C. S., Cheng, A., Endo, S., Heus, T., Lock, A. P., and van der Dussen, J. J. (2016). "CGILS Phase 2 LES intercomparison of response of subtropical marine low cloud regimes to CO2 quadrupling and a CMIP3 composite forcing change". In: *Journal of Advances in Modeling Earth Systems* 8.4, pp. 1714–1726.

Blossey, P. N., Bretherton, C. S., and Mohrmann, J. (2021). "Simulating Observed Cloud Transitions in the Northeast Pacific during CSET". In: *Monthly Weather Review* 149.8, pp. 2633–2658.

Blossey, P. N., Bretherton, C. S., Zhang, M., Cheng, A., Endo, S., Heus, T., Liu, Y., Lock, A. P., de Roode, S. R., and Xu, K.-M. (2013). "Marine low cloud sensitivity to an idealized climate change: The CGILS LES intercomparison". In: *Journal of Advances in Modeling Earth Systems* 5.2, pp. 234–258.

Böing, S. J., Dritschel, D. G., Parker, D. J., and Blyth, A. M. (2019). "Comparison of the Moist Parcel-in-Cell (MPIC) model with large-eddy simulation for an idealized cloud". In: *Quarterly Journal of the Royal Meteorological Society* 145.722, pp. 1865–1881.

Bony, S. and Dufresne, J.-L. (2005). "Marine boundary layer clouds at the heart of tropical cloud feedback uncertainties in climate models". In: *Geophysical Research Letters* 32.20.

Boucher, O., Randall, D., Artaxo, P., Bretherton, C., Feingold, G., Forster, P., Kerminen, V.-M., Kondo, Y., Liao, H., Lohmann, U., Rasch, P., Satheesh, S. K., Sherwood, S., Stevens, B., and Zhang, X. Y. (2014). "Clouds and aerosols". In: *Climate Change 2013 the Physical Science Basis: Working Group I Contribution to the Fifth Assessment Report of the Intergovernmental Panel on Climate Change*. Vol. 9781107057. Cambridge University Press, pp. 571–658.

Brendecke, J., Dong, X., Xi, B., and Wu, P. (2021). "Maritime Cloud and Drizzle Microphysical Properties Retrieved From Ship-Based Observations During MAGIC". In: *Earth and Space Science* 8.5, e2020EA001588.

Bretherton, C. S., Wood, R., George, R. C., Leon, D., Allen, G., and Zheng, X. (2010). "Southeast Pacific stratocumulus clouds, precipitation and boundary layer structure sampled along 20° S during VOCALS-REx". In: *Atmospheric Chemistry and Physics* 10.21, pp. 10639–10654.

Bretherton, C. S., Austin, P., and Siems, S. T. (1995). "Cloudiness and marine boundary layer dynamics in the ASTEX Lagrangian experiments. Part II: cloudiness, drizzle, surface fluxes, and entrainment". In: *Journal of the Atmospheric Sciences* 52.16, pp. 2724–2735.

Bretherton, C. S., Blossey, P. N., and Uchida, J. (2007). "Cloud droplet sedimentation, entrainment efficiency, and subtropical stratocumulus albedo". In: *Geophysical Research Letters* 34.3, p. L03813.

Bretherton, C. S., Macvean, M. K., Bechtold, P., Chlond, A., Cotton, W. R., Cuxart, J., Cuijpers, H., Mhairoutdinov, M., Kosovic, B., Lewellen, D., Moeng, C. H., Siebesma, P., Stevens, B., Stevens, D. E., Sykes, I., and Wyant, M. C. (1999a). "An intercomparison of radiatively driven entrainment and turbulence in a smoke cloud, as simulated by different numerical models". In: *Quarterly Journal of the Royal Meteorological Society* 125.554, pp. 391–423.

Bretherton, C. S. and Pincus, R. (1995). "Cloudiness and marine boundary layer dynamics in the ASTEX Lagrangian experiments. Part I: synoptic setting and vertical structure". In: *Journal of the Atmospheric Sciences* 52.16, pp. 2707–2723.

Bretherton, C. S. (2015). *Insights into low-latitude cloud feedbacks from high-resolution models.*

Bretherton, C. S. and Blossey, P. N. (2014). "Low cloud reduction in a greenhouse-warmed climate: Results from Lagrangian les of a subtropical marine cloudiness transition". In: *Journal of Advances in Modeling Earth Systems* 6.1, pp. 91–114.

Bretherton, C. S., Krueger, S. K., Wyant, M. C., Bechtold, P., Van Meijgaard, E., Stevens, B., and Teixeira, J. (1999b). "A GCSS boundary-layer cloud model intercomparison study of the first ASTEX Lagrangian experiment". In: *Boundary-Layer Meteorology* 93.3, pp. 341–380.

Bretherton, C. S., McCoy, I. L., Mohrmann, J., Wood, R., Ghate, V., Gettelman, A., Bardeen, C. G., Albrecht, B. A., and Zuidema, P. (2019). "Cloud, aerosol, and boundary layer structure across the northeast Pacific stratocumulus-cumulus transition as observed during CSET". In: *Monthly Weather Review* 147.6, pp. 2083–2103.

Bretherton, C. S. and Wyant, M. C. (1997). "Moisture transport, lower-tropospheric stability, and decoupling of cloud-topped boundary layers". In: *Journal of the Atmospheric Sciences* 54.1, pp. 148–167.

Brown, A. R., Derbyshire, S. H., and Mason, P. J. (1994). "Large-eddy simulation of stable atmospheric boundary layers with a revised stochastic subgrid model". In: *Quarterly Journal of the Royal Meteorological Society* 120.520, pp. 1485–1512.

Brown, N., Weiland, M., Hill, A., Shipway, B., Allen, T., Maynard, C., and Rezny, M. (2020). *A highly scalable met office NERC cloud model*.

Carslaw, K. S., Boucher, O., Spracklen, D. V., Mann, G. W., Rae, J. G. L., Woodward, S., and Kulmala, M. (2010). "A review of natural aerosol interactions and feedbacks within the Earth system". In: *Atmospheric Chemistry and Physics* 10.4, pp. 1701–1737.

Carslaw, K. S., Lee, L. A., Reddington, C. L., Pringle, K. J., Rap, A., Forster, P. M., Mann, G. W., Spracklen, D. V., Woodhouse, M. T., Regayre, L. A., and Pierce, J. R. (2013). "Large contribution of natural aerosols to uncertainty in indirect forcing". In: *Nature* 503.7474, pp. 67–71.

Carslaw, K. S. (2022). *Aerosols and Climate*. San Diego: Elsevier.

Ceppi, P., Brient, F., Zelinka, M. D., and Hartmann, D. L. (2017). "Cloud feedback mechanisms and their representation in global climate models". In: *Wiley Interdisciplinary Reviews: Climate Change* 8.4, e465.

Cess, R. D., Potter, G. L., Blanchet, J. P., Boer, G. J., Del Genio, A. D., Déqué, M., Dymnikov, V., Galin, V., Gates, W. L., Ghan, S. J., Kiehl, J. T., Lacis, A. A., Le Treut, H., Li, Z.-X., Liang, X.-Z., McAvaney, B. J., Meleshko, V. P., Mitchell, J. F. B., Morcrette, J.-J., Randall, D. A., Rikus, L., Roeckner, E., Royer, J. F., Schlese, U., Sheinin, D. A., Slingo, A., Sokolov, A. P., Taylor, K. E., Washington, W. M., Wetherald, R. T., Yagai, I., and Zhang, M.-H. (1990). "Intercomparison and interpretation of climate feedback processes in 19 atmospheric general circulation models". In: *Journal of Geophysical Research: Atmospheres* 95.D10, pp. 16601–16615.

Christensen, M. W. and Stephens, G. L. (2011). "Microphysical and macrophysical responses of marine stratocumulus polluted by underlying ships: Evidence of cloud deepening". In: *Journal of Geophysical Research: Atmospheres* 116.D3.

Christensen, M. W., Jones, W. K., and Stier, P. (2020). "Aerosols enhance cloud lifetime and brightness along the stratus-to-cumulus transition". In: *Proceedings of the National Academy of Sciences of the United States of America* 117.30, pp. 17591–17598.

Chung, D., Matheou, G., and Teixeira, J. (2012). "Steady-State Large-Eddy Simulations to Study the Stratocumulus to Shallow Cumulus Cloud Transition". In: *Journal of the Atmospheric Sciences* 69.11, pp. 3264–3276.

Courant, R., Friedrichs, K., and Lewy, H. (1928). "Über die partiellen Differenzengleichungen der mathematischen Physik". In: *Mathematische Annalen* 100.1, pp. 32–74.

Curry, J. A., Schramm, J. L., and Ebert, E. E. (1993). "Impact of clouds on the surface radiation balance of the Arctic Ocean". In: *Meteorology and Atmospheric Physics* 51.3, pp. 197–217.

Dal Gesso, S., van der Dussen, J. J., Siebesma, A. P., de Roode, S. R., Boutle, I. A., Kamae, Y., Roehrig, R., and Vial, J. (2015). "A single-column model intercomparison on the stratocumulus representation in present-day and future climate". In: *Journal of Advances in Modeling Earth Systems* 7.2, pp. 617–647.

de Roode, S. R. and Duynkerke, P. G. (1996). "Dynamics of cumulus rising into stratocumulus as observed during the first 'Lagrangian' experiment of ASTEX". In: *Quarterly Journal of the Royal Meteorological Society* 122.535, pp. 1597–1623.

de Roode, S. R., Sandu, I., van der Dussen, J. J., Ackerman, A. S., Blossey, P., Jarecka, D., Lock, A., Siebesma, A. P., and Stevens, B. (2016). "Large-eddy simulations of EUCLIPSE-GASS lagrangian stratocumulus-to-cumulus transitions: Mean state, turbulence, and decoupling". In: *Journal of the Atmospheric Sciences* 73.6, pp. 2485–2508.

Dearden, C., Hill, A., Coe, H., and Choularton, T. (2018). "The role of droplet sedimentation in the evolution of low-level clouds over southern West Africa". In: *Atmospheric Chemistry and Physics* 18.19, pp. 14253–14269.

Deardorff, J. W. (1974). "Three-dimensional numerical study of turbulence in an entraining mixed layer". In: *Boundary-Layer Meteorology* 7.2, pp. 199–226.

— (1980). "Cloud top entrainment instability." In: *Journal of the Atmospheric Sciences* 37.1, pp. 131–147.

Diamond, M. S., Saide, P. E., Zuidema, P., Ackerman, A. S., Doherty, S. J., Fridlind, A. M., Gordon, H., Howes, C., Kazil, J., Yamaguchi, T., Zhang, J., Feingold, G., and Wood, R. (2022). "Cloud adjustments from large-scale smoke–circulation interactions strongly modulate the southeastern Atlantic stratocumulus-to-cumulus transition". In: *Atmospheric Chemistry and Physics* 22.18, pp. 12113–12151.

Douglas, A. and L'Ecuyer, T. (2021). "Global evidence of aerosol-induced invigoration in marine cumulus clouds". In: *Atmospheric Chemistry and Physics* 21.19, pp. 15103–15114.

Douglas, A. and L'Ecuyer, T. (2020). "Quantifying cloud adjustments and the radiative forcing due to aerosol-cloud interactions in satellite observations of warm marine clouds". In: *Atmospheric Chemistry and Physics* 20.10, pp. 6225–6241.

Dufresne, J. L. and Bony, S. (2008). "An assessment of the primary sources of spread of global warming estimates from coupled atmosphere-ocean models". In: *Journal of Climate* 21.19, pp. 5135–5144.

Duynkerke, P. G. (1993). "The stability of cloud top with regard to entrainment: amendment of the theory of cloud-top entrainment instability". In: *Journal of the Atmospheric Sciences* 50.3, pp. 495–502.

Eastman, R., McCoy, I. L., and Wood, R. (2022). "Wind, Rain, and the Closed to Open Cell Transition in Subtropical Marine Stratocumulus". In: *Journal of Geophysical Research: Atmospheres* 127.20, e2022JD036795.

Eastman, R., Terai, C. R., Grosvenor, D. P., and Wood, R. (2021). "Evaluating the Lagrangian Evolution of Subtropical Low Clouds in GCMs Using Observations: Mean Evolution, Time Scales, and Responses to Predictors". In: *Journal of the Atmospheric Sciences* 78.2, pp. 353–372.

Eastman, R. and Wood, R. (2016). "Factors controlling low-cloud evolution over the eastern subtropical oceans: A Lagrangian perspective using the A-train satellites". In: *Journal of the Atmospheric Sciences* 73.1, pp. 331–351.

Eastman, R., Wood, R., and Kuan Ting, O. (2017). "The subtropical stratocumulus-topped planetary boundary layer: A climatology and the lagrangian evolution". In: *Journal of the Atmospheric Sciences* 74.8, pp. 2633–2656.

Edwards, J. M. and Slingo, A. (1996). "Studies with a flexible new radiation code. I: Choosing a configuration for a large-scale model". In: *Quarterly Journal of the Royal Meteorological Society* 122.531, pp. 689–719.

Erfani, E., Blossey, P., Wood, R., Mohrmann, J., Doherty, S. J., Wyant, M., and O, K.-T. (2022). "Simulating Aerosol Lifecycle Impacts on the Subtropical Stratocumulus-to-Cumulus Transition Using Large-Eddy Simulations". In: *Journal of Geophysical Research: Atmospheres* 127.21, e2022JD037258.

Feingold, G., Jiang, H., and Harrington, J. Y. (2005). "On smoke suppression of clouds in Amazonia". In: *Geophysical Research Letters* 32.2, pp. 1–4.

Feingold, G., McComiskey, A., Yamaguchi, T., Johnson, J. S., Carslaw, K. S., and Schmidte, K. S. (2016). "New approaches to quantifying aerosol influence on the cloud radiative effect". In: *Proceedings of the National Academy of Sciences of the United States of America* 113.21, pp. 5812–5819.

Field, P. R., Hill, A., Shipway, B., Furtado, K., Wilkinson, J., Miltenberger, A., Gordon, H., Grosvenor, D. P., Stevens, R., and Van Weverberg, K. (2023). "Implementation of a Double Moment Cloud Microphysics Scheme in the UK Met Office Regional Numerical Weather Prediction Model". In: *Quarterly Journal of the Royal Meteorological Society* 149.752, pp. 703–739.

Forster, P., Storelvmo, T., Armour, K., Collins, W., Dufresne, J.-L., Frame, D., Lunt, D., Mauritsen, T., Palmer, M., Watanabe, M., Wild, M., and Zhang, H. (2021). "The Earth's Energy Budget, Climate Feedbacks, and Climate Sensitivity". In: *Climate Change 2021: The Physical Science Basis. Contribution of Working Group I to the Sixth Assessment Report of the Intergovernmental Panel on Climate Change*. Cambridge: Cambridge University Press, pp. 923–1054.

Forster, P. M., Richardson, T., Maycock, A. C., Smith, C. J., Samset, B. H., Myhre, G., Andrews, T., Pincus, R., and Schulz, M. (2016). "Recommendations for diagnosing effective radiative forcing from climate models for CMIP6". In: *Journal of Geophysical Research: Atmospheres* 121.20, pp. 412–460.

Gettelman, A. and Sherwood, S. C. (2016). "Processes Responsible for Cloud Feedback". In: *Current Climate Change Reports* 2.4, pp. 179–189.

GEWEX Cloud System Science Team (1993). "The GEWEX cloud system study (GCSS)". In: *Bulletin - American Meteorological Society* 74.3, pp. 387–399.

Ghonima, M. S., Norris, J. R., Heus, T., and Kleissl, J. (2015). "Reconciling and validating the cloud thickness and liquid water path tendencies proposed by R. Wood and J. J. van der Dussen et al." In: *Journal of the Atmospheric Sciences* 72.5, pp. 2033–2040.

Glassmeier, F., Hoffmann, F., Johnson, J. S., Yamaguchi, T., Carslaw, K. S., and Feingold, G. (2019). "An emulator approach to stratocumulus susceptibility". In: *Atmospheric Chemistry and Physics* 19.15, pp. 10191–10203.

Goren, T., Kazil, J., Hoffmann, F., Yamaguchi, T., and Feingold, G. (2019). "Anthropogenic Air Pollution Delays Marine Stratocumulus Breakup to Open Cells". In: *Geophysical Research Letters* 46.23, pp. 14135–14144.

Gramacy, R. B. and Lee, H. K. (2008). "Bayesian treed Gaussian process models with an application to computer modeling". In: *Journal of the American Statistical Association* 103.483, pp. 1119–1130.

— (2012). "Cases for the nugget in modeling computer experiments". In: *Statistics and Computing* 22.3, pp. 713–722.

Gray, M. E. B., Petch, J., Derbyshire, S. H., Brown, A. R., Lock, A. P., Swann, H. A., and Brown, P. R. A. (2001). "Version 2.3 of the Met Office Large Eddy Model: Part II. Scientific Documentation". In: *Met O (APR) Turbulence and Diffusion Note No. 276.*

Green, P. and Sibson, R. (1978). "Computing Dirichlet Tessellations in the Plane". In: *The Computer Journal* 21.2, pp. 168–173.

Grosvenor, D. P., Field, P. R., Hill, A. A., and Shipway, B. J. (2017). "The relative importance of macrophysical and cloud albedo changes for aerosol-induced radiative effects in closed-cell stratocumulus: Insight from the modelling of a case study". In: *Atmospheric Chemistry and Physics* 17.8, pp. 5155–5183.

Gryspeerdt, E., Goren, T., Sourdeval, O., Quaas, J., Mülmenstädt, J., Dipu, S., Unglaub, C., Gettelman, A., and Christensen, M. (2019). "Constraining the aerosol influence on cloud liquid water path". In: *Atmospheric Chemistry and Physics* 19.8, pp. 5331–5347.

Hansen, J., Sato, M., and Ruedy, R. (1997). "Radiative forcing and climate response". In: *Journal of Geophysical Research: Atmospheres* 102.D6, pp. 6831–6864.

Hansen, J., Nazarenko, L., Ruedy, R., Sato, M., Willis, J., Genio, A. D., Koch, D., Lacis, A., Lo, K., Menon, S., Novakov, T., Perlwitz, J., Russell, G., Schmidt, G. A., and Tausnev, N. (2005). "Earth's Energy Imbalance: Confirmation and Implications". In: *Science* 308.5727, pp. 1431–1435.

Hartmann, D. L., Ockert-Bell, M. E., and Michelsen, M. L. (1992). "The Effect of Cloud Type on Earth's Energy Balance: Global Analysis". In: *Journal of Climate* 5.11, pp. 1281–1304.

Henderson, D. A., Boys, R. J., Krishnan, K. J., Lawless, C., and Wilkinson, D. J. (2009). "Bayesian Emulation and Calibration of a Stochastic Computer Model of Mitochondrial DNA Deletions in Substantia Nigra Neurons". In: *Journal of the American Statistical Association* 104, pp. 76–87.

Hill, A. A. and Dobbie, S. (2008). "The impact of aerosols on non-precipitating marine stratocumulus. II: The semi-direct effect". In: *Quarterly Journal of the Royal Meteorological Society* 134.634, pp. 1155–1165.

Hill, A. A., Shipway, B. J., and Boutle, I. A. (2015). "How sensitive are aerosol-precipitation interactions to the warm rain representation?" In: *Journal of Advances in Modeling Earth Systems* 7.3, pp. 987–1004.

Hill, A. A., Feingold, G., and Jiang, H. (2009). "The Influence of Entrainment and Mixing Assumption on Aerosol–Cloud Interactions in Marine Stratocumulus". In: *Journal of the Atmospheric Sciences* 66.5, pp. 1450–1464.

Hoffmann, F., Glassmeier, F., Yamaguchi, T., and Feingold, G. (2020). "Liquid Water Path Steady States in Stratocumulus: Insights from Process-Level Emulation and Mixed-Layer Theory". In: *Journal of the Atmospheric Sciences* 77.6, pp. 2203–2215.

Igel, A. L., van den Heever, S. C., and Johnson, J. S. (2018). "Meteorological and Land Surface Properties Impacting Sea Breeze Extent and Aerosol Distribution in a Dry Environment". In: *Journal of Geophysical Research: Atmospheres* 123.1, pp. 22–37.

Iooss, B., Janon, A., and Pujol, G. (2023). *Global Sensitivity Analysis of Model Outputs.*

Johnson, B. T., Shine, K. P., and Forster, P. M. (2004). "The semi-direct aerosol effect: Impact of absorbing aerosols on marine stratocumulus". In: *Quarterly Journal of the Royal Meteorological Society* 130.599, pp. 1407–1422.

Johnson, J. S., Cui, Z., Lee, L. A., Gosling, J. P., Blyth, A. M., and Carslaw, K. S. (2015). "Evaluating uncertainty in convective cloud microphysics using statistical emulation". In: *Journal of Advances in Modeling Earth Systems* 7.1, pp. 162–187.

Johnson, J. S., Gosling, J. P., and Kennedy, M. C. (2011). "Gaussian process emulation for second-order Monte Carlo simulations". In: *Journal of Statistical Planning and Inference* 141.5, pp. 1838–1848.

Johnson, J. S., Regayre, L. A., Yoshioka, M., Pringle, K. J., Lee, L. A., Sexton, D. M., Rostron, J. W., Booth, B. B., and Carslaw, K. S. (2018). "The importance of comprehensive parameter sampling and multiple observations for robust constraint of aerosol radiative forcing". In: *Atmospheric Chemistry and Physics* 18.17, pp. 13031–13053.

Jones, B. and Johnson, R. T. (2009). "Design and analysis for the Gaussian process model". In: *Quality and Reliability Engineering International* 25.5, pp. 515–524.

Jones, C. R., Bretherton, C. S., and Leon, D. (2011). "Coupled vs. decoupled boundary layers in VOCALS-REx". In: *Atmospheric Chemistry and Physics* 11.14, pp. 7143–7153.

Jones, C. R., Bretherton, C. S., and Blossey, P. N. (2014). "Fast stratocumulus time scale in mixed layer model and large eddy simulation". In: *Journal of Advances in Modeling Earth Systems* 6.1, pp. 206–222.

Kazil, J., Yamaguchi, T., and Feingold, G. (2017). "Mesoscale organization, entrainment, and the properties of a closed-cell stratocumulus cloud". In: *Journal of Advances in Modeling Earth Systems* 9.5, pp. 2214–2229.

Khairoutdinov, M. and Kogan, Y. (2000). "A New Cloud Physics Parameterization in a Large-Eddy Simulation Model of Marine Stratocumulus". In: *Monthly Weather Review* 128.1.

Klein, S. A., Hartmann, D. L., and Norris, J. R. (1995). "On the relationships among low-cloud structure, sea surface temperature, and atmospheric circulation in the summertime northeast Pacific". In: *Journal of Climate* 8.5, pp. 1140–1155.

Klein, S. A. and Hartmann, D. L. (1993). "The Seasonal Cycle of Low Stratiform Clouds". In: *Journal of Climate* 6.8, pp. 1587–1606.

Klimont, Z., Kupiainen, K., Heyes, C., Purohit, P., Cofala, J., Rafaj, P., Borken-Kleefeld, J., and Schöpp, W. (2017). "Global anthropogenic emissions of particulate matter including black carbon". In: *Atmospheric Chemistry and Physics* 17.14, pp. 8681–8723.

Kogan, Y. (2013). "A Cumulus Cloud Microphysics Parameterization for Cloud-Resolving Models". In: *Journal of the Atmospheric Sciences* 70.5, pp. 1423–1436.

Krueger, S. K., McLean, G. T., and Qiang Fu (1995). "Numerical simulation of the stratus-to-cumulus transition in the subtropical marine boundary layer. Part I: boundary-layer structure". In: *Journal of the Atmospheric Sciences* 52.16, pp. 2839–2850.

Kuo, H.-C. and Schubert, W. H. (1988). "Stability of cloud-topped boundary layers". In: *Quarterly Journal of the Royal Meteorological Society* 114.482, pp. 887–916.

Lee, L. A., Carslaw, K. S., Pringle, K. J., Mann, G. W., and Spracklen, D. V. (2011). "Emulation of a complex global aerosol model to quantify sensitivity to uncertain parameters". In: *Atmospheric Chemistry and Physics* 11.23, pp. 12253–12273.

Lee, L. A., Pringle, K. J., Reddington, C. L., Mann, G. W., Stier, P., Spracklen, D. V., Pierce, J. R., and Carslaw, K. S. (2013). "The magnitude and causes of uncertainty in global model simulations of cloud condensation nuclei". In: *Atmospheric Chemistry and Physics* 13.17, pp. 8879–8914.

Leonard, B. P., MacVean, M. K., and Lock, A. P. (1993). "Positivity-preserving numerical schemes for multidimensional advection". In: *NASA Technical Memorandum 106055 (ICOMP-93905)*. NASA technical memorandum ; 106055. Ed. by U. S. N. A. Administration and Space.

Lilly, D. K. (1962). "On the numerical simulation of buoyant convection". In: *Tellus* 14.2, pp. 148–172.

Lilly, D. K. (1968). "Models of cloud-topped mixed layers under a strong inversion". In: *Quarterly Journal of the Royal Meteorological Society* 94.401, pp. 292–309.

Loeppky, J. L., Sacks, J., and Welch, W. J. (2009). "Choosing the sample size of a computer experiment: A practical guide". In: *Technometrics* 51.4, pp. 366–376.

Lohmann, U., Lüönd, F., and Mahrt, F. (2016). *An Introduction to Clouds: From the Microscale to Climate*. Cambridge: Cambridge University Press.

MacVean, M. K. and Mason, P. J. (1990). "Cloud-Top Entrainment Instability through Small-Scale Mixing and Its Parameterization in Numerical Models". English. In: *Journal of Atmospheric Sciences* 47.8, pp. 1012–1030.

Malavelle, F. F., Haywood, J. M., Jones, A., Gettelman, A., Clarisse, L., Bauduin, S., Allan, R. P., Karset, I. H. H., Kristjánsson, J. E., Oreopoulos, L., Cho, N., Lee, D., Bellouin, N., Boucher, O., Grosvenor, D. P., Carslaw, K. S., Dhomse, S., Mann, G. W., Schmidt, A., Coe, H., Hartley, M. E., Dalvi, M., Hill, A. A., Johnson, B. T., Johnson, C. E., Knight, J. R., O'Connor, F. M., Stier, P., Myhre, G., Platnick, S., Stephens, G. L., Takahashi, H., and Thordarson, T. (2017). "Strong constraints on aerosol-cloud interactions from volcanic eruptions". In: *Nature* 546.7659, pp. 485–491.

Manners, J., Edwards, J. M., Hill, P., and Thelen, J.-C. (2015). *SOCRATES (Suite Of Community RAdiative Transfer codes based on Edwards and Slingo) Technical Guide*.

Marshall, L., Johnson, J. S., Mann, G. W., Lee, L., Dhomse, S. S., Regayre, L., Yoshioka, M., Carslaw, K. S., and Schmidt, A. (2019). "Exploring How Eruption Source Parameters Affect Volcanic Radiative Forcing Using Statistical Emulation". In: *Journal of Geophysical Research: Atmospheres* 124.2, pp. 964–985.

Marshall, L. R., Schmidt, A., Johnson, J. S., Mann, G. W., Lee, L. A., Rigby, R., and Carslaw, K. S. (2021). "Unknown Eruption Source Parameters Cause Large Uncertainty in Historical Volcanic Radiative Forcing Reconstructions". In: *Journal of Geophysical Research: Atmospheres* 126.13, e2020JD033578.

Martin, G. M., Johnson, D. W., Rogers, D. P., Jonas, P. R., Minnis, P., and Hegg, D. A. (1995). "Observations of the Interaction between Cumulus Clouds and Warm Stratocumulus Clouds in the Marine Boundary Layer during ASTEX". English. In: *Journal of Atmospheric Sciences* 52.16, pp. 2902–2922.

Mauger, G. S. and Norris, J. R. (2010). "Assessing the impact of meteorological history on subtropical cloud fraction". In: *Journal of Climate* 23.11, pp. 2926–2940.

McCoy, I. L., Bretherton, C. S., Wood, R., Twohy, C. H., Gettelman, A., Bardeen, C. G., and Toohey, D. W. (2021). "Influences of Recent Particle Formation on Southern Ocean Aerosol Variability and Low Cloud Properties". In: *Journal of Geophysical Research: Atmospheres* 126.8, e2020JD033529.

McGibbon, J. and Bretherton, C. S. (2017). "Skill of ship-following large-eddy simulations in reproducing MAGIC observations across the northeast Pacific stratocu-

mulus to cumulus transition region". In: *Journal of Advances in Modeling Earth Systems* 9.2, pp. 810–831.

McKay, M. D., Beckman, R. J., and Conover, W. J. (1979). "A Comparison of Three Methods for Selecting Values of Input Variables in the Analysis of Output from a Computer Code". In: *Technometrics* 21.2, p. 239.

Mellado, J. P. (2017). *Cloud-Top Entrainment in Stratocumulus Clouds*.

Miller, M. A. and Albrecht, B. A. (1995). "Surface-based observations of mesoscale cumulus-stratocumulus interaction during ASTEX". In: *Journal of the Atmospheric Sciences* 52.16, pp. 2809–2826.

Miltenberger, A. K., Field, P. R., Hill, A. A., Rosenberg, P., Shipway, B. J., Wilkinson, J. M., Scovell, R., and Blyth, A. M. (2018). "Aerosol–cloud interactions in mixed-phase convective clouds – Part 1: Aerosol perturbations". In: *Atmospheric Chemistry and Physics* 18.5, pp. 3119–3145.

Moeng, C. H., Cotton, W. R., Bretherton, C., Chlond, A., Khairoutdinov, M., Krueger, S., Lewellen, W. S., MacVean, M. K., Pasquier, J. R., Rand, H. A., Siebesma, A. P., Stevens, B., and Sykes, R. I. (1996). "Simulation of a stratocumulus-topped planetary boundary layer: Intercomparison among different numerical codes". In: *Bulletin of the American Meteorological Society* 77.2, pp. 261–278.

Moeng, C. H. (1984). "A Large-Eddy-Simulation Model for the Study of Planetary Boundary-Layer Turbulence". In: *Journal of Atmospheric Sciences* 41.13, pp. 2052–2062.

— (2000). "Entrainment Rate, Cloud Fraction, and Liquid Water Path of PBL Stratocumulus Clouds". In: *Journal of the Atmospheric Sciences* 57.21, pp. 3627–3643.

Mohammadi, H., Challenor, P., Goodfellow, M., and Williamson, D. (2019). "Emulating computer models with step-discontinuous outputs using Gaussian processes". In: *arXiv e-prints*.

Montagna, S. and Tokdar, S. T. (2013). "Computer emulation with non-stationary Gaussian processes". In: *arXiv e-prints* 4, pp. 26–47.

Morris, M. D. and Mitchell, T. J. (1995). "Exploratory designs for computational experiments". In: *Journal of Statistical Planning and Inference* 43.3, pp. 381–402.

Mülmenstädt, J. and Feingold, G. (2018). "The Radiative Forcing of Aerosol–Cloud Interactions in Liquid Clouds: Wrestling and Embracing Uncertainty". In: *Current Climate Change Reports* 4.1, pp. 23–40.

Myhre, G., Shindell, D., Bréon, F.-m., Collins, W., Fuglestvedt, J., Huang, J., Koch, D., Lamarque, J.-f., Lee, D., Mendoza, B., Nakajima, T., Robock, A., Stephens, G., Takemura, T., and Zhang, H. (2013). *Anthropogenic and Natural Radiative Forcing. In: Climate Change 2013: The Physical Science Basis. Contribution of Working Group I to the Fifth Assessment Report of the Intergovernmental Panel on Climate Change*. Tech. rep. Cambridge: Cambridge University Press.

Nicholls, S. (1984). "The dynamics of stratocumulus: Aircraft observations and comparisons with a mixed layer model". In: *Quarterly Journal of the Royal Meteorological Society* 110.466, pp. 783–820.

Nuijens, L. and Siebesma, A. P. (2019). "Boundary Layer Clouds and Convection over Subtropical Oceans in our Current and in a Warmer Climate". In: *Current Climate Change Reports 2019 5:2* 5.2, pp. 80–94.

O, K.-T., Wood, R., and Bretherton, C. S. (2018). "Ultraclean Layers and Optically Thin Clouds in the Stratocumulus-to-Cumulus Transition. Part II: Depletion of Cloud Droplets and Cloud Condensation Nuclei through Collision–Coalescence". In: *Journal of the Atmospheric Sciences* 75.5, pp. 1653–1673.

O'Hagan, A. (2006). "Bayesian analysis of computer code outputs: A tutorial". In: *Reliability Engineering and System Safety* 91.10-11, pp. 1290–1300.

Oyebamiji, O. K., Wilkinson, D. J., Jayathilake, P. G., Curtis, T. P., Rushton, S. P., Li, B., and Gupta, P. (2017). "Gaussian process emulation of an individual-based model simulation of microbial communities". In: *Journal of Computational Science* 22, pp. 69–84.

Painemal, D., Minnis, P., and Nordeen, M. (2015). "Aerosol variability, synoptic-scale processes, and their link to the cloud microphysics over the northeast pacific during MAGIC". In: *Journal of Geophysical Research* 120.10, pp. 5122–5139.

Paluch, I. R. and Lenschow, D. H. (1991). "Stratiform Cloud Formation in the Marine Boundary Layer". English. In: *Journal of Atmospheric Sciences* 48.19, pp. 2141–2158.

Park, J. M., van den Heever, S. C., Igel, A. L., Grant, L. D., Johnson, J. S., Saleeby, S. M., Miller, S. D., and Reid, J. S. (2020). "Environmental Controls on Tropical Sea Breeze Convection and Resulting Aerosol Redistribution". In: *Journal of Geophysical Research: Atmospheres* 125.6.

Piacsek, S. A. and Williams, G. P. (1970). "Conservation properties of convection difference schemes". In: *Journal of Computational Physics* 6.3, pp. 392–405.

Pier Siebesma, A., Bretherton, C. S., Brown, A., Chlond, A., Cuxart, J., Duynkerke, P. G., Jiang, H., Khairoutdinov, M., Lewellen, D., Moeng, C. H., Sanchez, E., Stevens, B., and Stevens, D. E. (2003). "A large eddy simulation intercomparison study of shallow cumulus convection". In: *Journal of the Atmospheric Sciences* 60.10, pp. 1201–1219.

Pincus, R. and Baker, M. B. (1994). "Effect of precipitation on the albedo susceptibility of clouds in the marine boundary layer". In: *Nature* 372.6503, pp. 250–252.

Pincus, R., Baker, M. B., and Bretherton, C. S. (1997). "What controls stratocumulus radiative properties? Lagrangian observations of cloud evolution". In: *Journal of the Atmospheric Sciences* 54.17, pp. 2215–2236.

Poku, C., Ross, A. N., Hill, A. A., Blyth, A. M., and Shipway, B. (2021). "Is a more physical representation of aerosol activation needed for simulations of fog?" In: *Atmospheric Chemistry and Physics* 21.9, pp. 7271–7292.

Pope, C. A., Gosling, J. P., Barber, S., Johnson, J. S., Yamaguchi, T., Feingold, G., and Blackwell, P. G. (2021). "Gaussian Process Modeling of Heterogeneity and Discontinuities Using Voronoi Tessellations". In: *Technometrics* 63.1, pp. 53–63.

Possner, A., Eastman, R., Bender, F., and Glassmeier, F. (2020). "Deconvolution of boundary layer depth and aerosol constraints on cloud water path in subtropical stratocumulus decks". In: *Atmospheric Chemistry and Physics* 20.6, pp. 3609–3621.

Pressel, K. G., Mishra, S., Schneider, T., Kaul, C. M., and Tan, Z. (2017). "Numerics and subgrid-scale modeling in large eddy simulations of stratocumulus clouds". In: *Journal of Advances in Modeling Earth Systems* 9.2, pp. 1342–1365.

Quaas, J. and Gryspeerdt, E. (2022). "Aerosol-cloud interactions in liquid clouds". In: *Aerosols and Climate*. Ed. by K. Carslaw. San Diego: Elsevier. Chap. 12, pp. 489–544.

R Core Team (2018). *R: A language and environment for statistical computing*. Vienna, Austria.

Randall, D. A., Coakley, J. A., Lenschow, D. H., Fairall, C. W., Kropfli, R. A., Randall, D. A., J. A. Coakley, J., Fairall, C. W., Kropfli, R. A., and Lenschow, D. H. (1984). "Outlook for Research on Subtropical Marine Stratification Clouds". In: *Bulletin of the American Meteorological Society* 65.12, pp. 1290–1301.

Randall, D. A. (1980). "Conditional instability of the first kind up-side down." In: *Journal of the Atmospheric Sciences* 37.1, pp. 125–130.

Reddington, C. L., Carslaw, K. S., Stier, P., Schutgens, N., Coe, H., Liu, D., Allan, J., Browse, J., Pringle, K. J., Lee, L. A., Yoshioka, M., Johnson, J. S., Regayre, L. A., Spracklen, D. V., Mann, G. W., Clarke, A., Hermann, M., Henning, S., Wex, H., Kristensen, T. B., Leaitch, W. R., Pöschl, U., Rose, D., Andreae, M. O., Schmale, J., Kondo, Y., Oshima, N., Schwarz, J. P., Nenes, A., Anderson, B., Roberts, G. C., Snider, J. R., Leck, C., Quinn, P. K., Chi, X., Ding, A., Jimenez, J. L., and Zhang, Q. (2017). "The global aerosol synthesis and science project (GASSP): Measurements and modeling to reduce uncertainty". In: *Bulletin of the American Meteorological Society* 98.9, pp. 1857–1877.

Regayre, L. A., Schmale, J., Johnson, J. S., Tatzelt, C., Baccarini, A., Henning, S., Yoshioka, M., Stratmann, F., Gysel-Beer, M., Grosvenor, D. P., and Carslaw, K. S. (2020). "The value of remote marine aerosol measurements for constraining radiative forcing uncertainty". In: *Atmospheric Chemistry and Physics* 20.16, pp. 10063–10072.

Regayre, L. A., Pringle, K. J., Booth, B. B., Lee, L. A., Mann, G. W., Browse, J., Woodhouse, M. T., Rap, A., Reddington, C. L., and Carslaw, K. S. (2014). "Un-

certainty in the magnitude of aerosol-cloud radiative forcing over recent decades". In: *Geophysical Research Letters* 41.24, pp. 9040–9049.

Regayre, L. A., Johnson, J. S., Yoshioka, M., Pringle, K. J., Sexton, D. M., Booth, B. B., Lee, L. A., Bellouin, N., and Carslaw, K. S. (2018). "Aerosol and physical atmosphere model parameters are both important sources of uncertainty in aerosol ERF". In: *Atmospheric Chemistry and Physics* 18.13, pp. 9975–10006.

Regayre, L. A., Pringle, K. J., Lee, L. A., Rap, A., Browse, J., Mann, G. W., Reddington, C. L., Carslaw, K. S., Booth, B. B., and Woodhouse, M. T. (2015). "The climatic importance of uncertainties in regional aerosol-cloud radiative forcings over recent decades". In: *Journal of Climate* 28.17, pp. 6589–6607.

Ringer, M. A., McAvaney, B. J., Andronova, N., Buja, L. E., Esch, M., Ingram, W. J., Li, B., Quaas, J., Roeckner, E., Senior, C. A., Soden, B. J., Volodin, E. M., Webb, M. J., and Williams, K. D. (2006). "Global mean cloud feedbacks in idealized climate change experiments". In: *Geophysical Research Letters* 33.7, p. L07718.

Roustant, O., Ginsbourger, D., and Deville, Y. (2012). "DiceKriging, DiceOptim: Two R Packages for the Analysis of Computer Experiments by Kriging-Based Metamodeling and Optimization". In: *Journal of Statistical Software* 51.1, pp. 1–55.

Saltelli, A., Tarantola, S., and Chan, K. P.-S. (1999). "A Quantitative Model-Independent Method for Global Sensitivity Analysis of Model Output". In: *Technometrics* 41.1, pp. 39–56.

Saltelli, A., Chan, K., and Scott, E. M. (2000). *Sensitivity Analysis*. Chichester, England: Wiley.

Sandu, I., Stevens, B., and Pincus, R. (2010). "On the transitions in marine boundary layer cloudiness". In: *Atmospheric Chemistry and Physics* 10.5, pp. 2377–2391.

Sandu, I. and Stevens, B. (2011). "On the Factors Modulating the Stratocumulus to Cumulus Transitions". In: *Journal of the Atmospheric Sciences* 68.9, pp. 1865–1881.

Sansom, R. (2021). "Demystifying the complex nature of stratocumulus clouds with machine learning". In: *Weather* 76.6, pp. 185–191.

Sarkar, M., Zuidema, P., Albrecht, B., Ghate, V., Jensen, J., Mohrmann, J., and Wood, R. (2020). "Observations pertaining to precipitation within the northeast Pacific stratocumulus-to-cumulus transition". In: *Monthly Weather Review* 148.3, pp. 1251–1273.

Schneider, T., Kaul, C. M., and Pressel, K. G. (2019). "Possible climate transitions from breakup of stratocumulus decks under greenhouse warming". In: *Nature Geoscience* 12.3, pp. 163–167.

Schneider, T., Teixeira, J., Bretherton, C. S., Brient, F., Pressel, K. G., Schär, C., and Siebesma, A. P. (2017). "Climate goals and computing the future of clouds". In: *Nature Climate Change* 7.1, pp. 3–5.

Shen, Z., Sridhar, A., Tan, Z., Jaruga, A., and Schneider, T. (2022). "A Library of Large-Eddy Simulations Forced by Global Climate Models". In: *Journal of Advances in Modeling Earth Systems* 14.3, e2021MS002631.

Shipway, B. J. and Hill, A. A. (2012). "Diagnosis of systematic differences between multiple parametrizations of warm rain microphysics using a kinematic framework". In: *Quarterly Journal of the Royal Meteorological Society* 138.669, pp. 2196–2211.

Siems, S. T., Lenschow, D. H., and Bretherton, C. S. (1993). "A Numerical Study of the Interaction between Stratocumulus and the Air Overlying It". In: *Journal of Atmospheric Sciences* 50.21, pp. 3663–3676.

Siems, S. T., Bretherton, C. S., Baker, M. B., Shy, S., and Breidenthal, R. E. (1990). "Buoyancy reversal and cloud-top entrainment instability". In: *Quarterly Journal of the Royal Meteorological Society* 116.493, pp. 705–739.

Smagorinsky, J. (1963). "GENERAL CIRCULATION EXPERIMENTS WITH THE PRIMITIVE EQUATIONS". In: *Monthly Weather Review* 91.3, pp. 99–164.

Smith, C. J., Kramer, R. J., Myhre, G., Alterskjr, K., Collins, W., Sima, A., Boucher, O., Dufresne, J. L., Nabat, P., Michou, M., Yukimoto, S., Cole, J., Paynter, D., Shiogama, H., M. O'Connor, F., Robertson, E., Wiltshire, A., Andrews, T., Hannay, C., Miller, R., Nazarenko, L., Kirkevg, A., Olivi, D., Fiedler, S., Lewinschal, A., MacKallah, C., Dix, M., Pincus, R., and M. Forster, P. (2020). "Effective radiative forcing and adjustments in CMIP6 models". In: *Atmospheric Chemistry and Physics* 20.16, pp. 9591–9618.

Soden, B. J. and Held, I. M. (2006). "An Assessment of Climate Feedbacks in Coupled Ocean–Atmosphere Models". In: *Journal of Climate* 19.14, pp. 3354–3360.

Stechmann, S. N. and Hottovy, S. (2016). "Cloud regimes as phase transitions". In: *Geophysical Research Letters* 43.12, pp. 6579–6587.

Stephens, G. L. and Greenwald, T. J. (1991). "The Earth's radiation budget and its relation to atmospheric hydrology: 2. Observations of cloud effects". In: *Journal of Geophysical Research: Atmospheres* 96.D8, pp. 15325–15340.

Stephens, G. L., Li, J., Wild, M., Clayson, C. A., Loeb, N., Kato, S., L'Ecuyer, T., Stackhouse, P. W., Lebsock, M., and Andrews, T. (2012). "An update on Earth's energy balance in light of the latest global observations". In: *Nature Geoscience* 5.10, pp. 691–696.

Stevens, B. (2000). "Cloud transitions and decoupling in shear-free stratocumulus-topped boundary layers". In: *Geophysical Research Letters* 27.16, pp. 2557–2560.

Stevens, B., Ackerman, A. S., Albrecht, B. A., Brown, A. R., Chlond, A., Cuxart, J., Duynkerke, P. G., Lewellen, D. C., Macvean, M. K., Neggers, R. A., Sánchez, E., Siebesma, A. P., and Stevens, D. E. (2001). "Simulations of trade wind cumuli under a strong inversion". In: *Journal of the Atmospheric Sciences* 58.14, pp. 1870–1891.

Stevens, B., Cotton, W. R., Feingold, G., and Moeng, C. H. (1998). "Large-eddy simulations of strongly precipitating, shallow, stratocumulus-topped boundary layers". In: *Journal of the Atmospheric Sciences* 55.24, pp. 3616–3638.

Stevens, B. and Feingold, G. (2009). *Untangling aerosol effects on clouds and precipitation in a buffered system.*

Stevens, B., Lenschow, D. H., Faloona, I., Moeng, C. H., Lilly, D. K., Blomquist, B., Vali, G., Bandy, A., Campos, T., Gerber, H., Haimov, S., Morley, B., and Thornton, D. (2003). "On entrainment rates in nocturnal marine stratocumulus". In: *Quarterly Journal of the Royal Meteorological Society* 129.595, pp. 3469–3493.

Stevens, B., Moeng, C. H., Ackerman, A. S., Bretherton, C. S., Chlond, A., de Roode, S., Edwards, J., Golaz, J. C., Jiang, H., Khairoutdinov, M., Kirkpatrick, M. P., Lewellen, D. C., Lock, A., Müller, F., Stevens, D. E., Whelan, E., and Zhu, P. (2005a). "Evaluation of large-eddy simulations via observations of nocturnal marine stratocumulus". In: *Monthly Weather Review* 133.6, pp. 1443–1462.

Stevens, B., Vali, G., Comstock, K., Wood, R., van Zanten, M. C., Austin, P. H., Bretherton, C. S., and Lenschow, D. H. (2005b). "Pockets of open cells and drizzle in marine stratocumulus". In: *Bulletin of the American Meteorological Society* 86.1, pp. 51–57.

Stubenrauch, C. J., Rossow, W. B., Kinne, S., Ackerman, S., Cesana, G., Chepfer, H., Girolamo, L. D., Getzewich, B., Guignard, A., Heidinger, A., Maddux, B. C., Menzel, W. P., Minnis, P., Pearl, C., Platnick, S., Poulsen, C., Riedi, J., Sun-Mack, S., Walther, A., Winker, D., Zeng, S., and Zhao, G. (2013). "Assessment of Global Cloud Datasets from Satellites: Project and Database Initiated by the GEWEX Radiation Panel". In: *Bulletin of the American Meteorological Society* 94.7, pp. 1031–1049.

Svensson, G., Tjernström, M., and Koračin, D. (2000). "The Sensitivity Of A Stratocumulus Transition: Model Simulations Of The Astex First Lagrangian". In: *Boundary-Layer Meteorology* 95.1, pp. 57–90.

Teixeira, J., Cardoso, S., Bonazzola, M., Cole, J., Delgenio, A., Demott, C., Franklin, C., Hannay, C., Jakob, C., Jiao, Y., Karlsson, J., Kitagawa, H., Köhler, M., Kuwano-Yoshida, A., Ledrian, C., Li, J., Lock, A., Miller, M. J., Marquet, P., Martins, J., Mechoso, C. R., Meijgaard, E. v., Meinke, I., Miranda, P. M. A., Mironov, D., Neggers, R., Pan, H. L., Randall, D. A., Rasch, P. J., Rockel, B., Rossow, W. B., Ritter, B., Siebesma, A. P., Soares, P. M. M., Turk, F. J., Vaillancourt, P. A., Von Engeln, A., and Zhao, M. (2011). "Tropical and subtropical cloud transitions in weather and climate prediction models: The GCSS/WGNE pacific cross-section intercomparison (GPCI)". In: *Journal of Climate* 24.20, pp. 5223–5256.

Tsai, J. Y. and Wu, C. M. (2016). "Critical transitions of stratocumulus dynamical systems due to perturbation in free-atmosphere moisture". In: *Dynamics of Atmospheres and Oceans* 76, pp. 1–13.

Twomey, S. (1974). "Pollution and the planetary albedo". In: *Atmospheric Environment (1967)* 8.12, pp. 1251–1256.

van der Dussen, J. J., de Roode, S. R., Ackerman, A. S., Blossey, P. N., Bretherton, C. S., Kurowski, M. J., Lock, A. P., Neggers, R. A. J., Sandu, I., and Siebesma, A. P. (2013). "The GASS/EUCLIPSE model intercomparison of the stratocumulus transition as observed during ASTEX: LES results". In: *Journal of Advances in Modeling Earth Systems* 5.3, pp. 483–499.

van der Dussen, J. J., de Roode, S. R., and Siebesma, A. P. (2014). "Factors controlling rapid stratocumulus cloud thinning". In: *Journal of the Atmospheric Sciences* 71.2, pp. 655–664.

— (2016). "How large-scale subsidence affects stratocumulus transitions". In: *Atmospheric Chemistry and Physics* 16.2, pp. 691–701.

Vial, J., Dufresne, J.-L., and Bony, S. (2013). "On the interpretation of inter-model spread in CMIP5 climate sensitivity estimates". In: *Climate Dynamics* 41.11, pp. 3339–3362.

Volodina, V. and Williamson, D. B. (2018). "Nonstationary Gaussian Process Emulators with Kernel Mixtures". In: *arXiv e-prints*.

Wang, Q. and Lenschow, D. H. (1995). "An observational study of the role of penetrating cumulus in a marine stratocumulus-topped boundary layer". In: *Journal of the Atmospheric Sciences* 52.16, pp. 2778–2787.

Wang, S. (1993). "Modeling Marine Boundary-Layer Clouds with a Two-Layer Model: A One-Dimensional Simulation". In: *Journal of the Atmospheric Sciences* 50.24, pp. 4001–4021.

Watson-Parris, D., Bellouin, N., Deaconu, L. T., Schutgens, N. A. J., Yoshioka, M., Regayre, L. A., Pringle, K. J., Johnson, J. S., Smith, C. J., Carslaw, K. S., and Stier, P. (2020). "Constraining Uncertainty in Aerosol Direct Forcing". In: *Geophysical Research Letters* 47.9, e2020GL087141.

Wellmann, C., Barrett, A. I., Johnson, J. S., Kunz, M., Vogel, B., Carslaw, K. S., and Hoose, C. (2018). "Using Emulators to Understand the Sensitivity of Deep Convective Clouds and Hail to Environmental Conditions". In: *Journal of Advances in Modeling Earth Systems* 10.12, pp. 3103–3122.

Wellmann, C., I Barrett, A., S Johnson, J., Kunz, M., Vogel, B., S Carslaw, K., and Hoose, C. (2020). "Comparing the impact of environmental conditions and microphysics on the forecast uncertainty of deep convective clouds and hail". In: *Atmospheric Chemistry and Physics* 20.4, pp. 2201–2219.

Wild, M., Hakuba, M. Z., Folini, D., Dörig-Ott, P., Schär, C., Kato, S., and Long, C. N. (2019). "The cloud-free global energy balance and inferred cloud radiative effects: an assessment based on direct observations and climate models". In: *Climate Dynamics* 52.7, pp. 4787–4812.

Williams, A. S. and Igel, A. L. (2021). "Cloud Top Radiative Cooling Rate Drives Non-Precipitating Stratiform Cloud Responses to Aerosol Concentration". In: *Geophysical Research Letters* 48.18, e2021GL094740.

Williamson, D. and Blaker, A. T. (2014). "Evolving Bayesian Emulators for Structured Chaotic Time Series, with Application to Large Climate Models". In: *SIAM/ASA Journal on Uncertainty Quantification* 2.1, pp. 1–28.

Wood, R. (2015). "Stratus and Stratocumulus". In: *Encyclopedia of Atmospheric Sciences*. Ed. by G. North, J. Pyle, and F. Zhang. 2nd ed. Vol. 2. London: Academic Press. Chap. 10.9, pp. 196–200.

Wood, R. (2007). "Cancellation of Aerosol Indirect Effects in Marine Stratocumulus through Cloud Thinning". English. In: *Journal of the Atmospheric Sciences* 64.7, pp. 2657–2669.

— (2012). *Stratocumulus clouds*.

Wood, R. and Bretherton, C. S. (2006). "On the Relationship between Stratiform Low Cloud Cover and Lower-Tropospheric Stability". English. In: *Journal of Climate* 19.24, pp. 6425–6432.

Wood, R., O, K.-T., Bretherton, C. S., Mohrmann, J., Albrecht, B. A., Zuidema, P., Ghate, V., Schwartz, C., Eloranta, E., Glienke, S., Shaw, R. A., Fugal, J., and Minnis, P. (2018). "Ultraclean layers and optically thin clouds in the stratocumulus-to-cumulus transition. Part I: Observations". In: *Journal of the Atmospheric Sciences* 75.5, pp. 1631–1652.

Wyant, M. C., Bretherton, C. S., Wood, R., Blossey, P. N., and McCoy, I. L. (2022). "High Free-Tropospheric Aitken-Mode Aerosol Concentrations Buffer Cloud Droplet Concentrations in Large-Eddy Simulations of Precipitating Stratocumulus". In: *Journal of Advances in Modeling Earth Systems* 14.6, e2021MS002930.

Wyant, M. C., Bretherton, C. S., Rand, H. A., and Stevens, D. E. (1997). "Numerical simulations and a conceptual model of the stratocumulus to trade cumulus transition". In: *Journal of the Atmospheric Sciences* 54.1, pp. 168–192.

Xiao, H., Wu, C. M., and Mechoso, C. R. (2011). "Buoyancy reversal, decoupling and the transition from stratocumulus to shallow cumulus topped marine boundary layers". In: *Climate Dynamics* 37.5, pp. 971–984.

Xu, X. and Xue, H. (2015). "Impacts of Free-Tropospheric Temperature and Humidity on Nocturnal Nonprecipitating Marine Stratocumulus". In: *Journal of the Atmospheric Sciences* 72.8, pp. 2853–2864.

Yamaguchi, T. and Feingold, G. (2015). "On the relationship between open cellular convective cloud patterns and the spatial distribution of precipitation". In: *Atmospheric Chemistry and Physics* 15.3, pp. 1237–1251.

Yamaguchi, T., Feingold, G., and Kazil, J. (2017). "Stratocumulus to Cumulus Transition by Drizzle". In: *Journal of Advances in Modeling Earth Systems* 9.6, pp. 2333–2349.

Yamaguchi, T., Feingold, G., Kazil, J., and McComiskey, A. (2015). "Stratocumulus to cumulus transition in the presence of elevated smoke layers". In: *Geophysical Research Letters* 42.23, pp. 10478–10485.

Yamaguchi, T. and Randall, D. A. (2008). "Large-eddy simulation of evaporatively driven entrainment in cloud-topped mixed layers". In: *Journal of the Atmospheric Sciences* 65.5, pp. 1481–1504.

Zelinka, M. D., Myers, T. A., McCoy, D. T., Po-Chedley, S., Caldwell, P. M., Ceppi, P., Klein, S. A., and Taylor, K. E. (2020). "Causes of Higher Climate Sensitivity in CMIP6 Models". In: *Geophysical Research Letters* 47.1, e2019GL085782.

Zhang, M., Bretherton, C. S., Blossey, P. N., Austin, P. H., Bacmeister, J. T., Bony, S., Brient, F., Cheedela, S. K., Cheng, A., Del Genio, A. D., de Roode, S. R., Endo, S., Franklin, C. N., Golaz, J. C., Hannay, C., Heus, T., Isotta, F. A., Dufresne, J. L., Kang, I. S., Kawai, H., Köhler, M., Larson, V. E., Liu, Y., Lock, A. P., Lohmann, U., Khairoutdinov, M. F., Molod, A. M., Neggers, R. A., Rasch, P., Sandu, I., Senkbeil, R., Siebesma, A. P., Siegenthaler-Le Drian, C., Stevens, B., Suarez, M. J., Xu, K. M., von Salzen, K., Webb, M. J., Wolf, A., and Zhao, M. (2013). "CGILS: Results from the first phase of an international project to understand the physical mechanisms of low cloud feedbacks in single column models". In: *Journal of Advances in Modeling Earth Systems* 5.4, pp. 826–842.

Zhang, M., Bretherton, C. S., Blossey, P. N., Bony, S., Brient, F., and Golaz, J.-C. (2012). "The CGILS experimental design to investigate low cloud feedbacks in general circulation models by using single-column and large-eddy simulation models". In: *Journal of Advances in Modeling Earth Systems* 4.4, n/a–n/a.

Zheng, Y., Zhang, H., and Li, Z. (2021). "Role of Surface Latent Heat Flux in Shallow Cloud Transitions: A Mechanism-Denial LES Study". English. In: *Journal of the Atmospheric Sciences* 78.9, pp. 2709–2723.

Zhou, X., Ackerman, A. S., Fridlind, A. M., Wood, R., and Kollias, P. (2017). "Impacts of solar-absorbing aerosol layers on the transition of stratocumulus to trade cumulus clouds". In: *Atmospheric Chemistry and Physics* 17.20, pp. 12725–12742.

Zhou, X. and Bretherton, C. S. (2019). "The Correlation of Mesoscale Humidity Anomalies With Mesoscale Organization of Marine Stratocumulus From Observations Over the ARM Eastern North Atlantic Site". In: *Journal of Geophysical Research: Atmospheres* 124.24, pp. 14059–14071.

Zhou, X., Heus, T., and Kollias, P. (2017). "Influences of drizzle on stratocumulus cloudiness and organization". In: *Journal of Geophysical Research* 122.13, pp. 6989–7003.

Zhou, X., Kollias, P., and Lewis, E. R. (2015). "Clouds, precipitation, and marine boundary layer structure during the MAGIC field campaign". In: *Journal of Climate* 28.6, pp. 2420–2442.

Appendix A

A.1 Increased droplet number

The perturbed parameter ensemble (PPE) was repeated for a higher fixed droplet number of 150 cm^{-3} (ND150) and the results show a pattern in parameter space (Figure A.1) that is similar to the pattern for droplet number = 50 cm^{-3} (ND50). The simulations from region A in ND150 are very similar to region A in ND50. All spin up to a liquid water path of 50 g m^{-2} or less and show little growth throughout the simulation. However, most of the region A simulations have a higher cloud fraction for ND150, with all but two spinning up to at least 0.8 and rather than decreasing, as in ND50, all cloud fractions in the ND150 case increase through the simulation. In region B, the simulations spin up to higher liquid water paths than in ND50 and cloud fractions very close to 1.

Gaussian process emulation was used to densely sample the parameter space and create response surfaces for the four cloud properties: liquid water path, liquid water path tendency, cloud fraction and cloud fraction tendency. The validation plots in Figure A.2 show that the emulator is a reasonable approximation of the model. The response surfaces in Figure A.3 show that the behaviour in the liquid water path and the liquid water path tendency are very similar to the ND50 case, but with larger values. The curvature round into region A is present in this case too showing that these interactions are not limited to the ND50 case. The cloud fraction is much more saturated at cloud fraction = 1. Since most of these simulations had cloud fraction remaining near 1 for the whole simulation the change over the simulation (tendency) is very small. These emulators were produced without a nugget term, but the addition of one would most likely smooth most of the cloud fraction tendency to 0 hr^{-1}.

A.2 Precipitation

There was very little precipitation for the ND50 PPE, which is to be expected since this was a non-drizzling case in Stevens et al. (2005a). However, there is a further difference in behaviours across the regimes here since the simulations in regime A have rain water

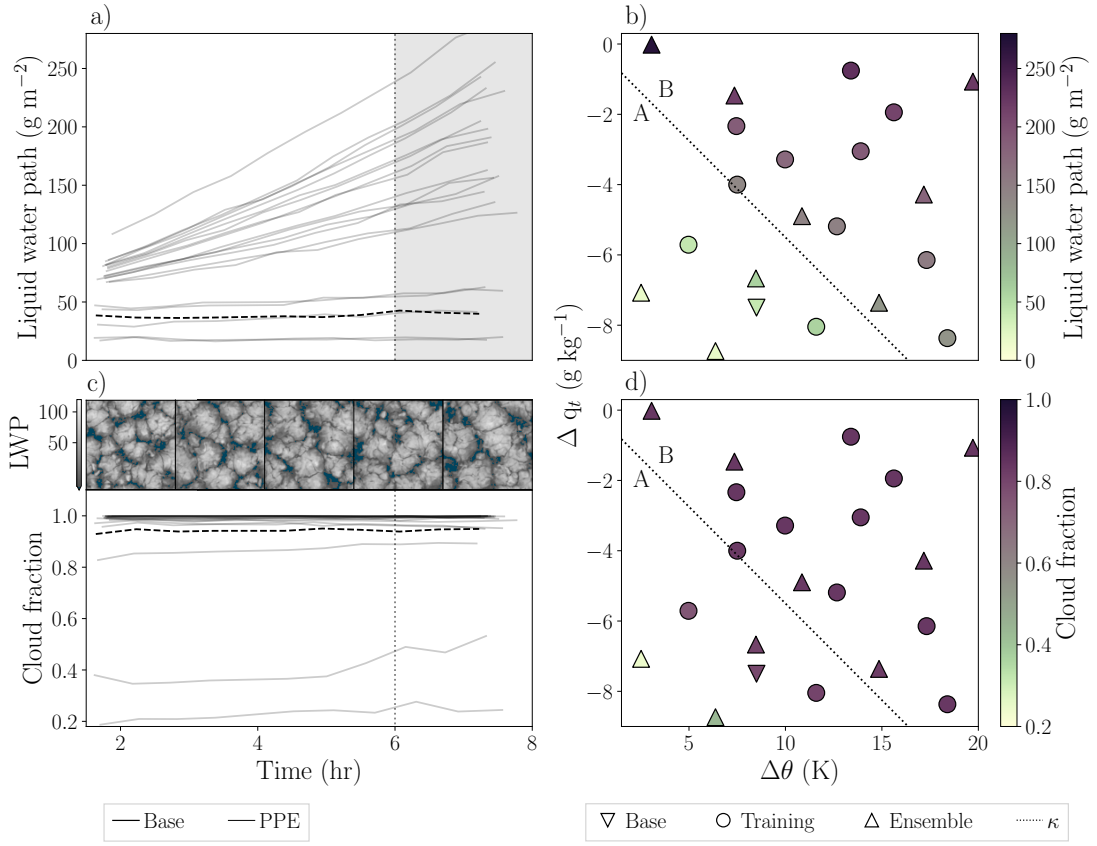

Figure A.1: Liquid water path and cloud fraction model output for the whole ensemble. a) Liquid water path and c) cloud fraction timeseries post-spinup to the end of the simulation. The last two hours (shaded area) are taken as an average for the training data. The base simulation is shown by the darker line and the point-ensemble simulations show the range of the ensemble as an envelope. The inset in c shows top-down snapshots of the liquid water path for the base simulation. b) Liquid water path and d) cloud fraction training data values plotted in parameter space, $\Delta\theta$ vs Δq_t. The κ line is the theoretical threshold for the κ parameter described in section 3.3, which splits the regions into A and B (see section 3.5.3).

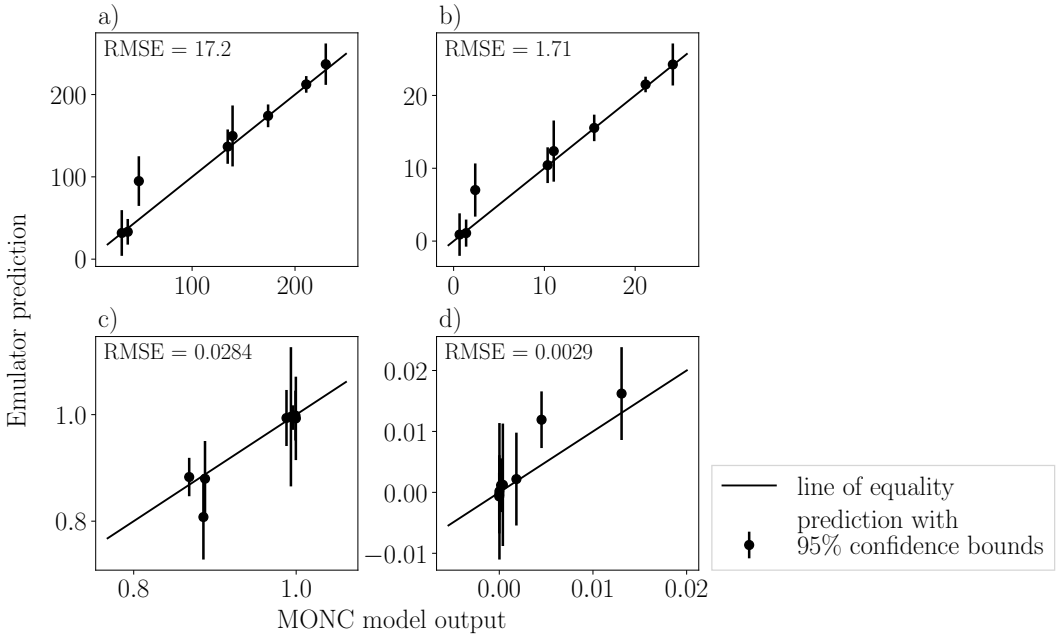

Figure A.2: Validation plots for the four cloud property emulators for ND150. a) liquid water path (g m^{-2}), b) liquid water path tendency (g m^{-2} hr^{-1}), c) cloud fraction and d) cloud fraction tendency (hr^{-1}). The MONC output values for each point are on the x axis and the emulator predicted values are on the y axis. The black line shows the line of equality and the error bars indicate the 95% confidence bounds on the emulator mean predictions.

path $\approx$ 0 g m^{-2} and surface precipitation $\approx$ 0 mm hr^{-1}, whereas the simulations in regime B have very small amount of precipitation.

A.3 Emulation with 20-point PPE

The addition of 6 extra points in Figure 3.7 does not have a large effect on the behaviour seen in the response surfaces compared with the original 20-point emulators (validation: Figure A.5, and response surfaces: Figure A.6). This affirms that the standard method of using 10 times the number of parameters in the PPE is sufficient training data for Gaussian process emulation (Loeppky, Sacks, and Welch, 2009), even when the points may be sparse around regions of interest.

A.4 Combining residuals without normalisation for the nugget term

Figure A.8 shows the result of trying to combine the residuals without normalisation, and although some of the histograms have large overlaps (e.g., [048] comb) none pass the KS test. ($p > 0.05$).

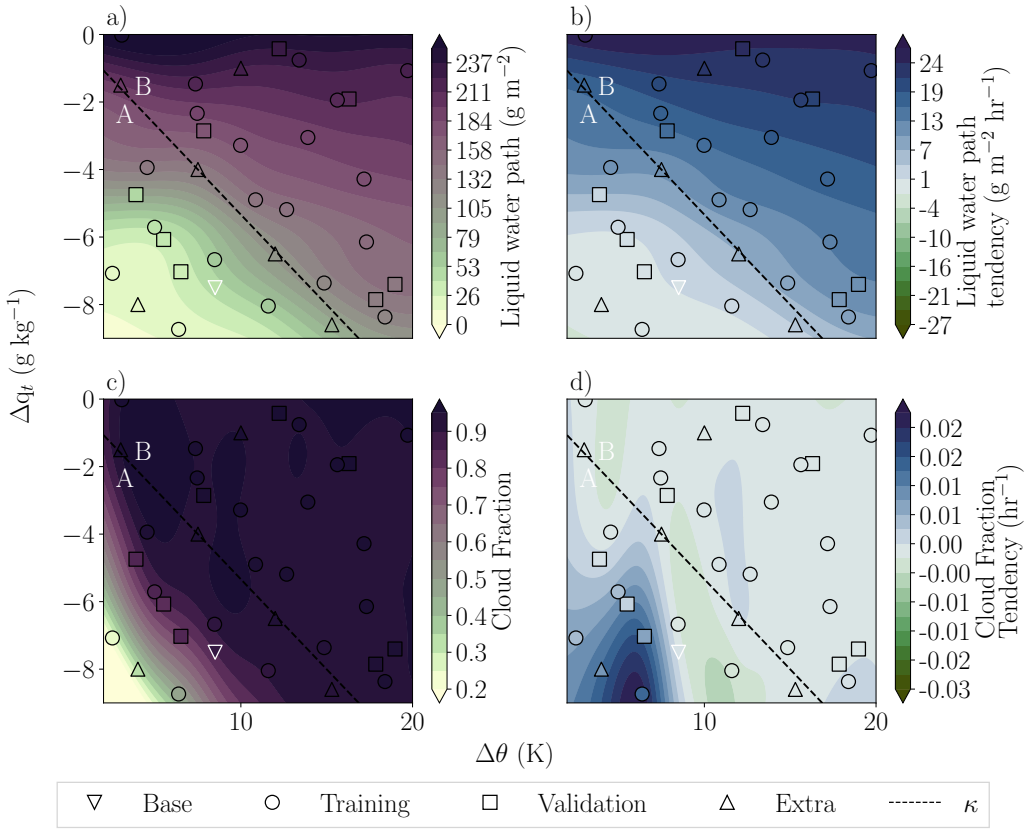

Figure A.3: Response surfaces produced from emulator mean predictions for ND150. a) liquid water path, b) liquid water path tendency, c) cloud fraction and d) cloud fraction tendency. The base simulation is shown by the inverse white triangle, the training data by the black circles, the validation data by the black squares, and the extra simulation points by the black triangles. The dashed black line is the κ threshold, where equation (3.1) = 0.23, and divides parameter space into region A and B.

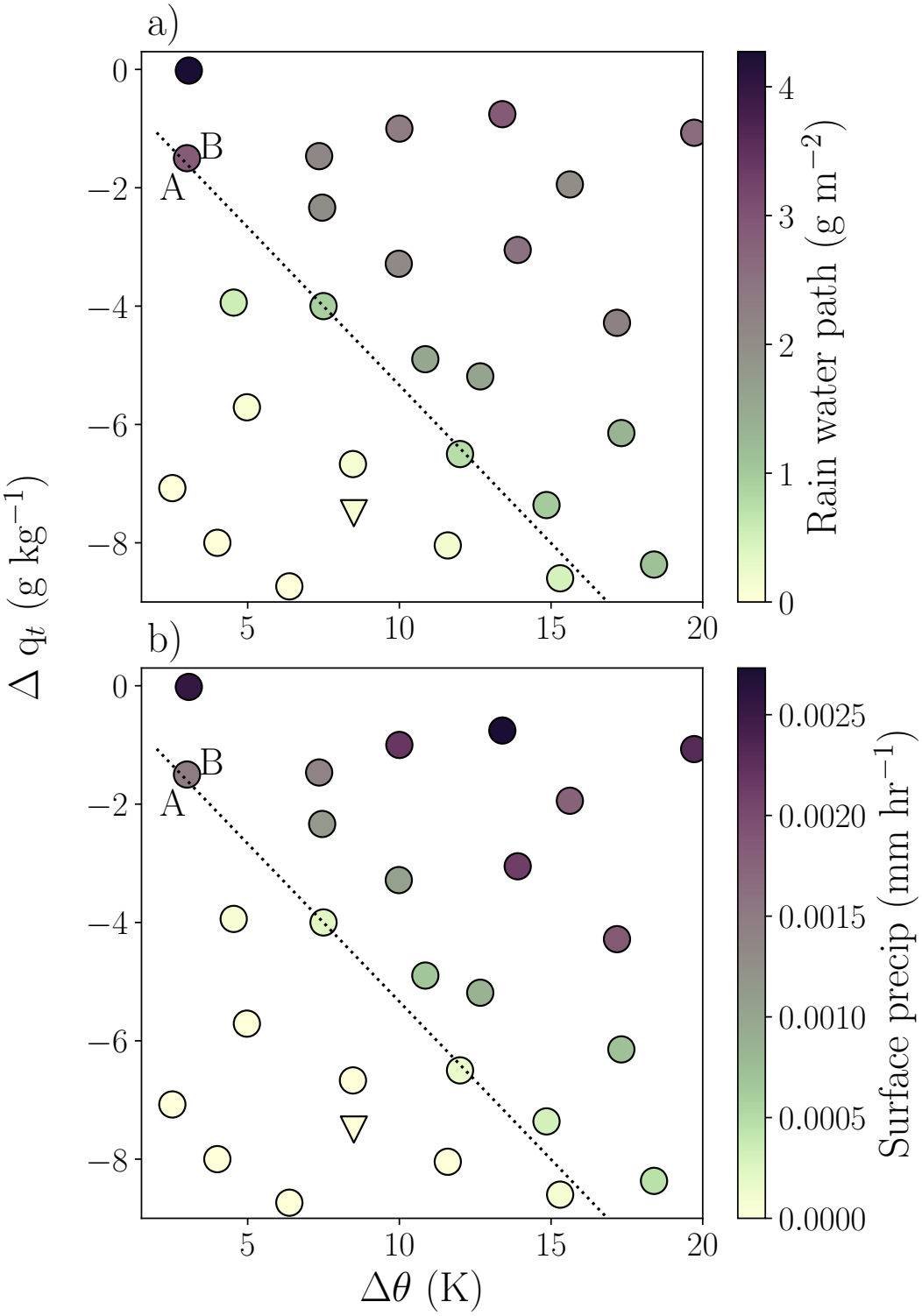

Figure A.4: Average precipitation through the ND50 PPE. a) Average rain water path and b) average hourly surface precipitation from post spinup to simulation end.

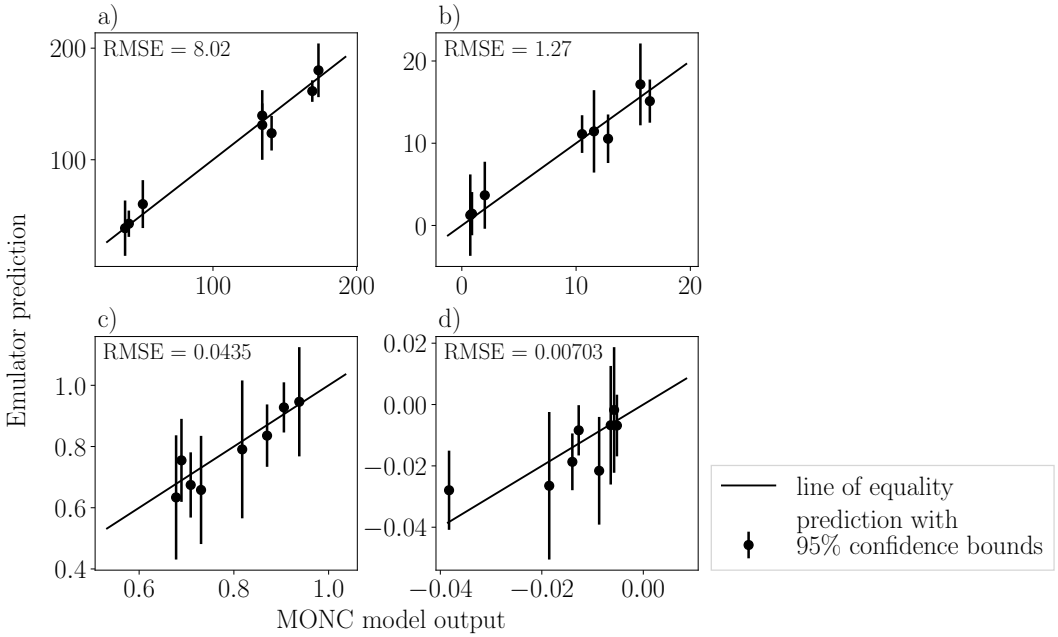

Figure A.5: Validation plots for the four cloud property emulators for ND50 with only the original 20 training data. a) liquid water path (g m^{-2}), b) liquid water path tendency (g m^{-2} hr^{-1}), c) cloud fraction and d) cloud fraction tendency (hr^{-1}). The MONC output values for each point are on the x axis and the emulator predicted values are on the y axis. The black line shows the line of equality and the error bars indicate the 95% confidence bounds on the emulator mean predictions.

A.5 Approximating variance

Because we normalised the residuals by the mean, a multiplying factor is required to make the variance the correct order of magnitude before being used in the emulation process. This is proven by simplifying the variance of the normalised residuals,

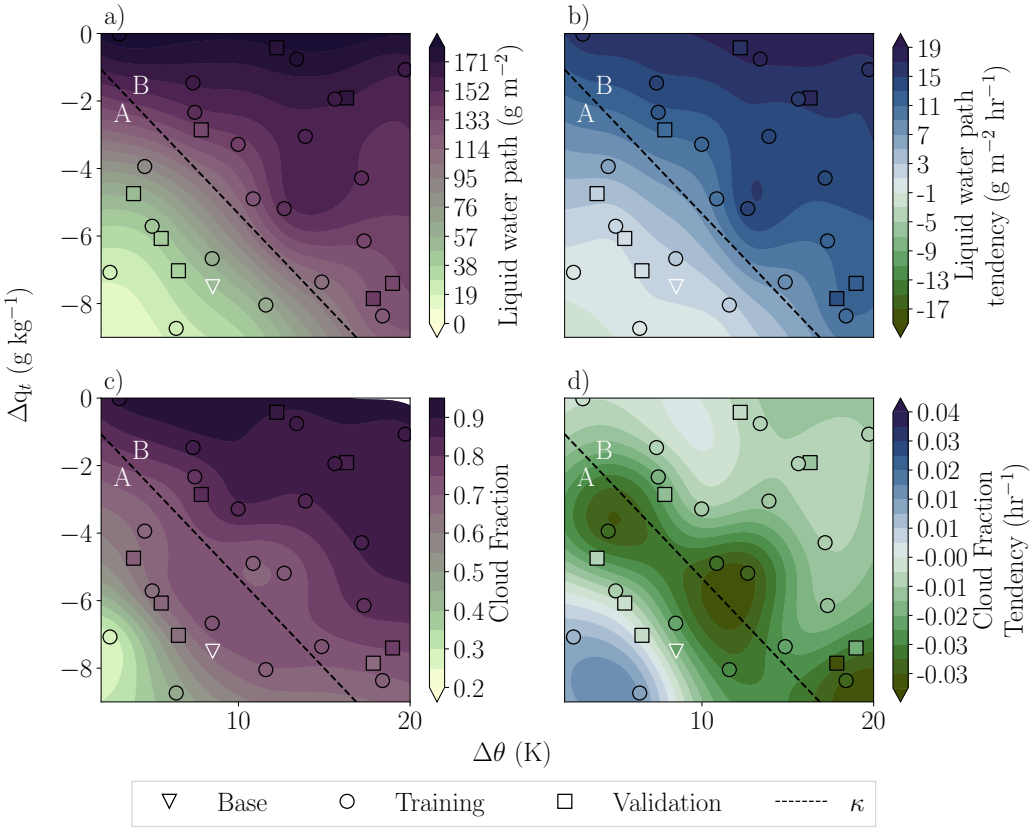

Figure A.6: Response surfaces produced from emulator mean predictions for ND50 with only the original 20 training data. a) liquid water path, b) liquid water path tendency, c) cloud fraction and d) cloud fraction tendency. The base simulation is shown by the inverse white triangle, the training data by the black circles, the validation data by the black squares, and the extra simulation points by the black triangles. The dashed black line is the κ threshold, where equation (3.1) = 0.23, and divides parameter space into region A and B.

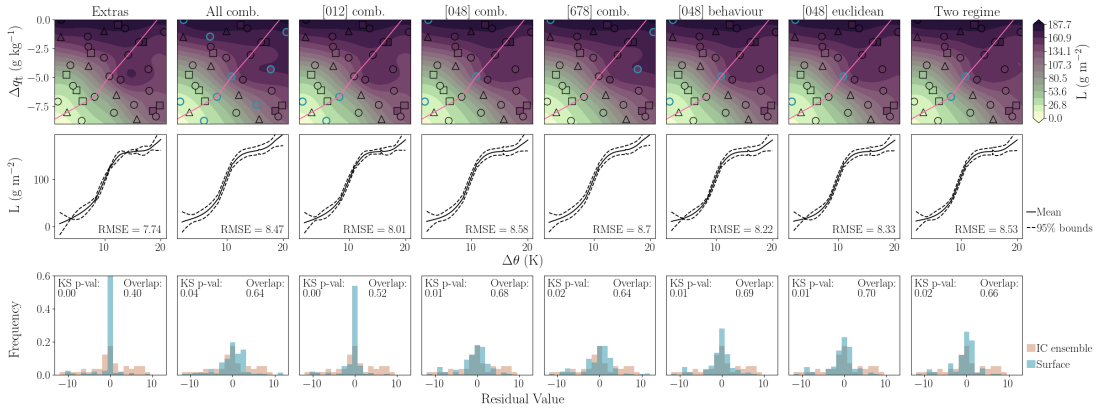

Figure A.7: The mean liquid water path emulator with different nugget term calculations from the model residuals without normalisation. Extras: No nugget term applied, nugget terms applied using the residuals from 1) All comb: all 9 ensembles, 2) [012] comb the smallest 3 liquid water path (L) points, 3) [048] comb: 3 well-spaced L points, 4) [678] comb: the 3 largest L points, 5-6) [048] behaviour and [048] Euclidean: 3 well-spaced L points 7) Two regime: only two points, one from each regimes. 1-4) "comb" plots combine all the residuals from the included points to calculate the variance and applied to all training data. 5-7) does not combine residuals but takes the variance from each ensemble and applies it to groups of training data 5) with similar L, 6) that are nearest neighbours and 7) in the same regime. Top row: emulator predicted response surfaces. Middle row: a transect through the pink line shown in top row showing mean emulator function and upper and lower 95% confidence bounds. Bottom row: comparison of the histograms of model residuals and emulator residuals (Figure 3.9). The RMSE, Kolmogorov-Smirnov p-values, and overlap values are given for each nugget term. The overlap value is computed as the fraction of histogram bars that overlap between the datasets.

$$\sigma_R^2 = \frac{\sum_{i=1}^{l}\sum_{j=1}^{k}[(\frac{Z_i^{(j)}-\bar{Z}_i}{\bar{Z}_i}) - \mu]^2}{N_R}, \mu = 0 \quad (A.1)$$

$$= \frac{\sum_{i=1}^{l}\sum_{j=1}^{k}[(\frac{Z_i^{(j)}-\bar{Z}_i}{\bar{Z}_i})]^2}{N_R}, \quad (A.2)$$

$$= \frac{\sum_{i=1}^{l}\frac{1}{\bar{Z}_i^2}\sum_{j=1}^{k}[(Z_i^{(j)}-\bar{Z}_i)]^2}{N_R}, N_R = \sum_{i=1}^{l} N_i \quad (A.3)$$

$$= \frac{\sum_{i=1}^{l}\frac{1}{\bar{Z}_i^2}\sum_{j=1}^{k}[(Z_i^{(j)}-\bar{Z}_i)]^2}{\sum_{i=1}^{l} N_i}, \quad (A.4)$$

$$= \sum_{i=1}^{l}\frac{1}{\bar{Z}_i^2}\frac{\sum_{j=1}^{k}[(Z_i^{(j)}-\bar{Z}_i)]^2}{N_i}, \quad (A.5)$$

$$= \sum_{i=1}^{l}\frac{1}{\bar{Z}_i^2}\sigma_i^2, \quad (A.6)$$

where σ_i^2 is the variance of each ensemble, Z_i, and N_i is the number of members in each ensemble. Thus, from this normalisation process, the variance of the residuals needs to be multiplied by a factor on the same order of magnitude as $\bar{Z_i^2}$ to be used in the emulation process. Note that we are not using a summation of the ensemble variances, as equation A6 indicates, because we are simply estimating from a small sample. The variance we are estimating is the lower bound, since any distribution is likely to be wider than what we have sampled.

A.6 Trialling different multiplier types

The "proportional" multiplier, where the variance for each point is multiplied by the L value at that point, does not pass the KS test for any tried combination of points (Figure A.8). The "mean" multiplier, where the variance for each point is multiplied by the PPE mean L, only passes the test for the All comb. nugget, which uses all the points (Figure A.8). The "maximum" multiplier, where the variance for each point is multiplied by the PPE maximum L passes for All comb., [048] comb., [678] comb., and Two regime. Thus, the combination of only three points gives an emulator build that is sufficient. Additionally, since only the larger nugget terms pass the KS test, these results suggest that for the liquid water path the calculated variances are underestimating the variance required.

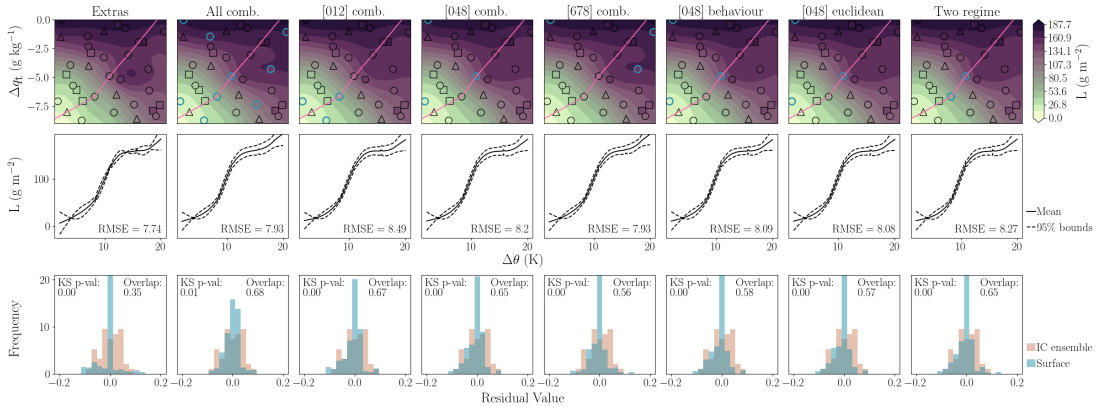

Figure A.8: The mean liquid water path emulator with different nugget term calculations from the model residuals with normalisation and multiplied by a proportional multiplier.

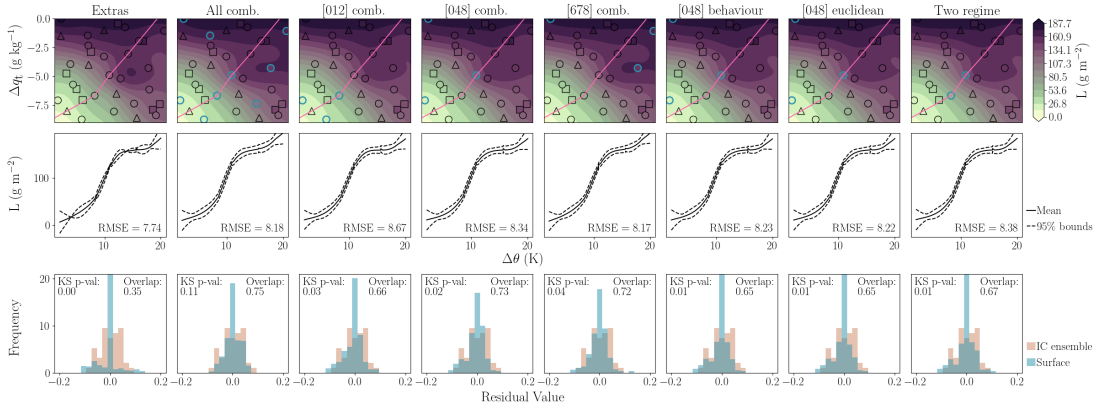

Figure A.9: The mean liquid water path emulator with different nugget term calculations from the model residuals with normalisation and multiplied by a mean multiplier.

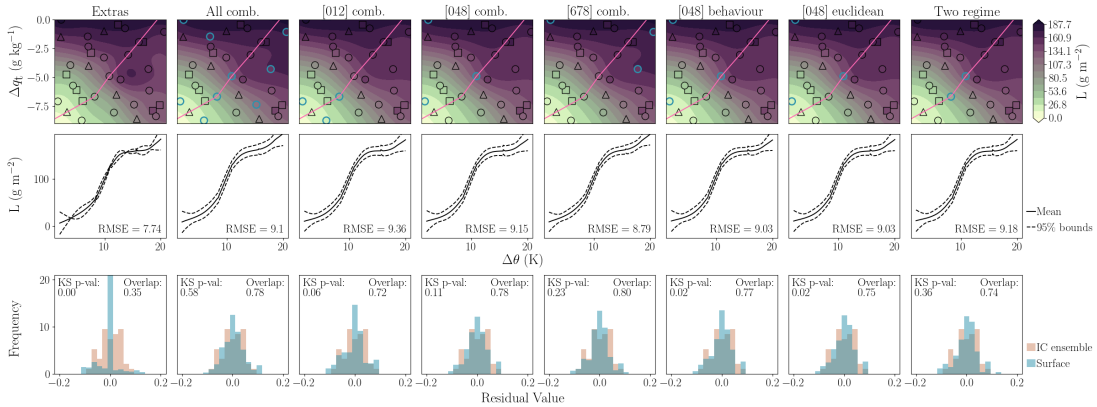

Figure A.10: The mean liquid water path emulator with different nugget term calculations from the model residuals with normalisation and multiplied by a maximum multiplier.

Appendix B

B.1 Evolution of parameter values through spin up

Figure B.1 shows that even though some of the parameter values evolved during spin up, the post spinup values were still well-spaced along the dimensions. The post-spinup values were appropriate to use for emulation so we chose to use these as they represent the initial conditions of the cloud better than the pre-spinup values.

B.2 Sea surface temperature for start of stratocumulus

Figure B.2 shows that the stage at which stratocumulus was formed (along the increasing SST gradient) was solely determined by the combined effects of the boundary layer humidity and the boundary layer depth. This is likely because the humidity determines how much vapour is available in the boundary layer for condensation and where the boundary layer is too shallow, the condensation level may not be reached by updrafts.

B.3 12-hour criteria for transition

The PPE analysis was repeated but with the subset of 13 simulations that transitioned more than 12 hours before the end of the simulation, we could be confident that they remained in a cumulus state. These results have the same conclusions as for the main PPE analysis, which shows the main analysis is robust even with the possibility that

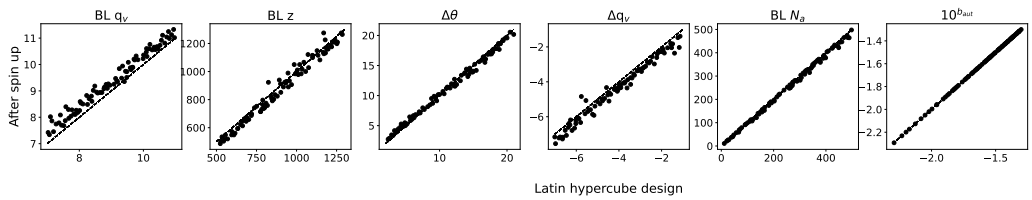

Figure B.1: Evolution of parameter values during spinup. Plots show the original Latin hypercube design values against the parameter values calculated after the model has spun up after 2 hours for each of the 6 perturbed parameters.

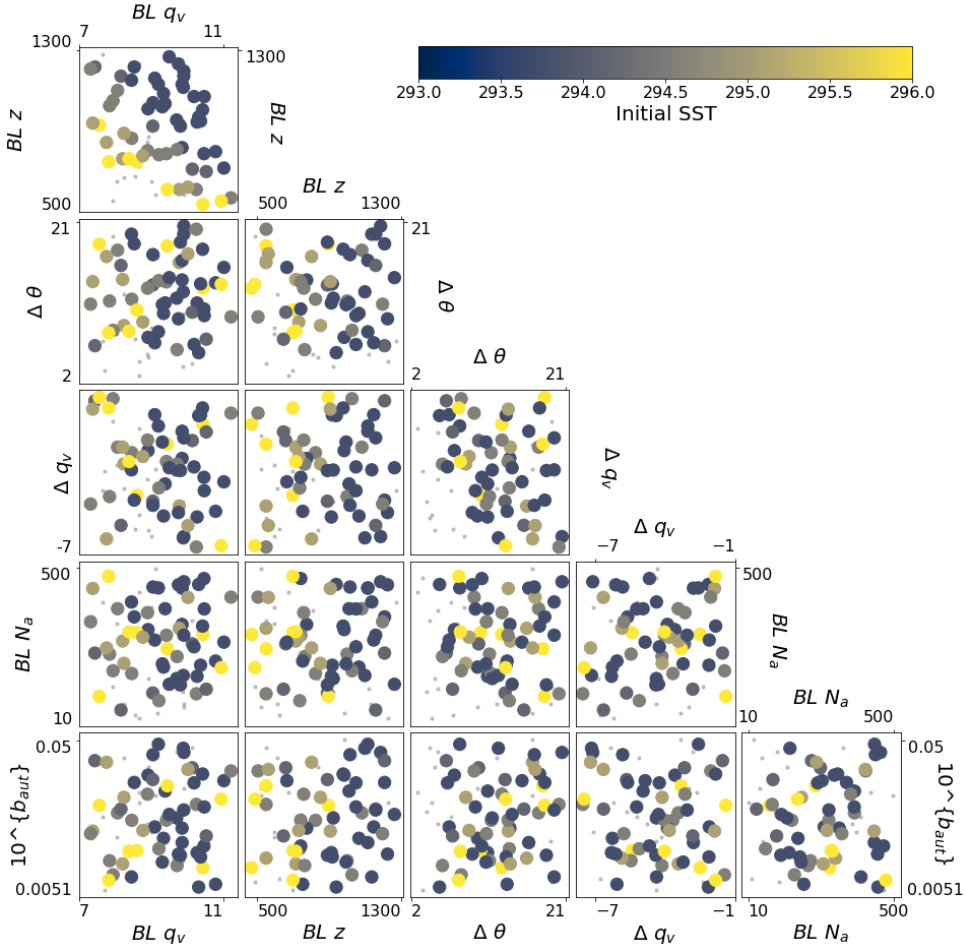

Figure B.2: Pairwise plot showing a scatter plot of each parameter combination, coloured by the sea surface temperature when stratocumulus was initially formed. Small, grey markers show the locations of the simulations which did not form stratocumulus.

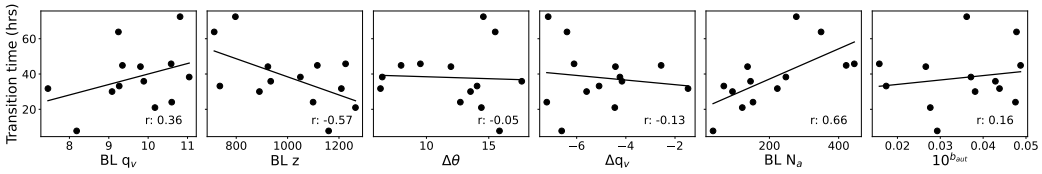

Figure B.3: One-dimensional scatter plots against transition time for each parameter with 12 hour criteria (see text). The scatter points show the 34 simulations that transitioned within the simulation time. A line of best fit is drawn and the correlation coefficient is given in each case.

the stratocumulus clouds recover after the simulations end.

B.4 Entrainment at start of stratocumulus

The entrainment at the start of stratocumulus is strongly determined by the inversion strength with a correlation coefficient of -0.80, which is much higher than for the other parameters (Figure B.7). Additionally, Figure B.8 shows that when the PPE is split by the mean rain water path, the entrainment rate correlates much more strongly with the transition time for low-drizzle environments than for the whole PPE data. We found that the inversion strength also only had a clear correlation with the transition time when the PPE was split by the mean rain water path. The high correlation of entrainment rate with inversion strength and their relationships with transition time in low-drizzle environments shows that the inversion strength is a strong control of the transition time in low-drizzle environments.

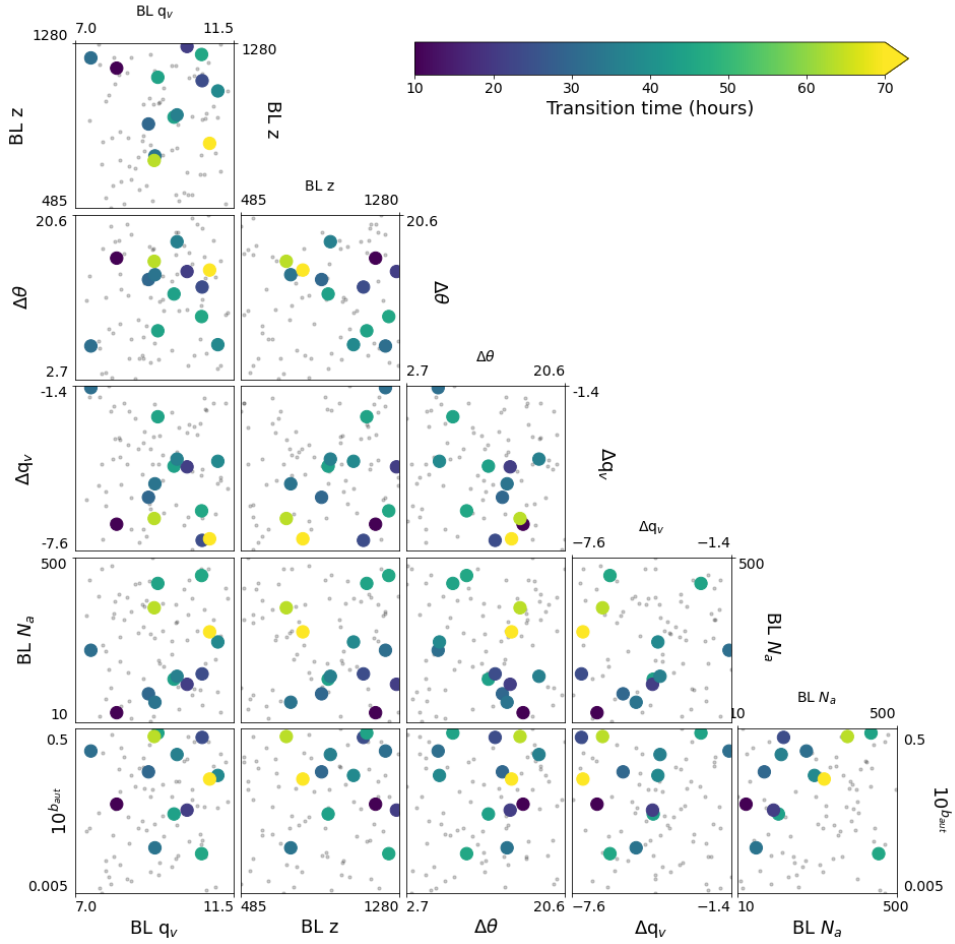

Figure B.4: Pairwise plot showing a scatter plot of each parameter combination, coloured by transition time with 12 hour criteria. Small, grey markers show the locations of the simulations which did not form stratocumulus and transition.

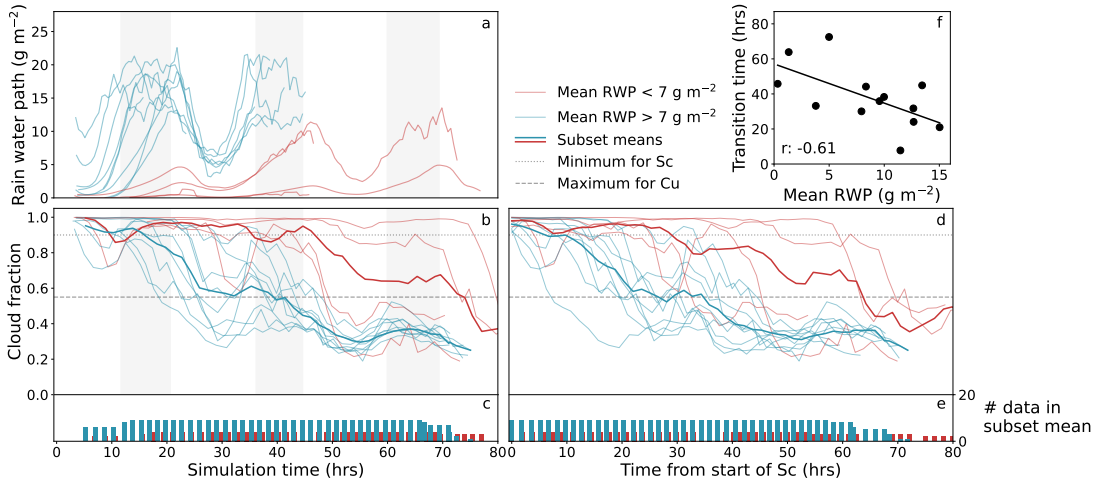

Figure B.5: The rain water path across the ensemble with 12 hour criteria. a) The domain-averaged rain water path timeseries for each member split by temporal mean rain water path greater than 7 g m^2 (blue) or less than (red). b) The cloud fraction timeseries as in figure 4.6c but coloured by mean RWP. The means over each subset (high or low mean RWP) are shown in bold. c) The number of data points used in calculating the mean of each subset at each timestep in b). d) As in b) but aligned to the start of stratocumulus. e) As in c) but for d). f) A scatter of the mean RWP for each member against the transition time, with a line of best fit.

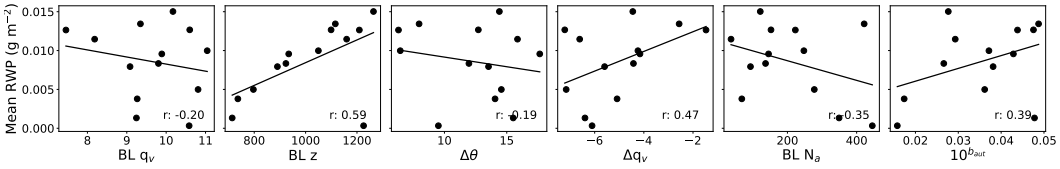

Figure B.6: One-dimensional scatter plots against mean rain water path for each parameter. The scatter points show the 34 simulations that transitioned within the simulation time. A line of best fit is drawn and the correlation coefficient is given in each case.

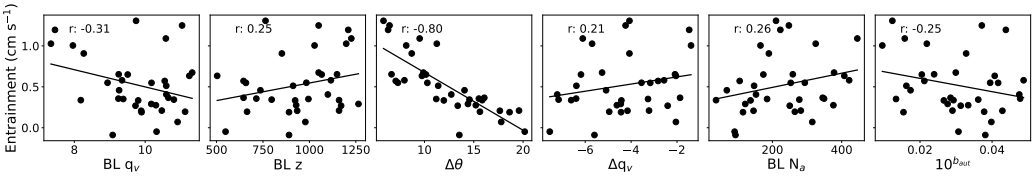

Figure B.7: One-dimensional scatter plots against the entrainment rate at the start of stratocumulus time. The scatter points show the 34 simulations that transitioned within the simulation time. A line of best fit is drawn and the correlation coefficient is given in each case.

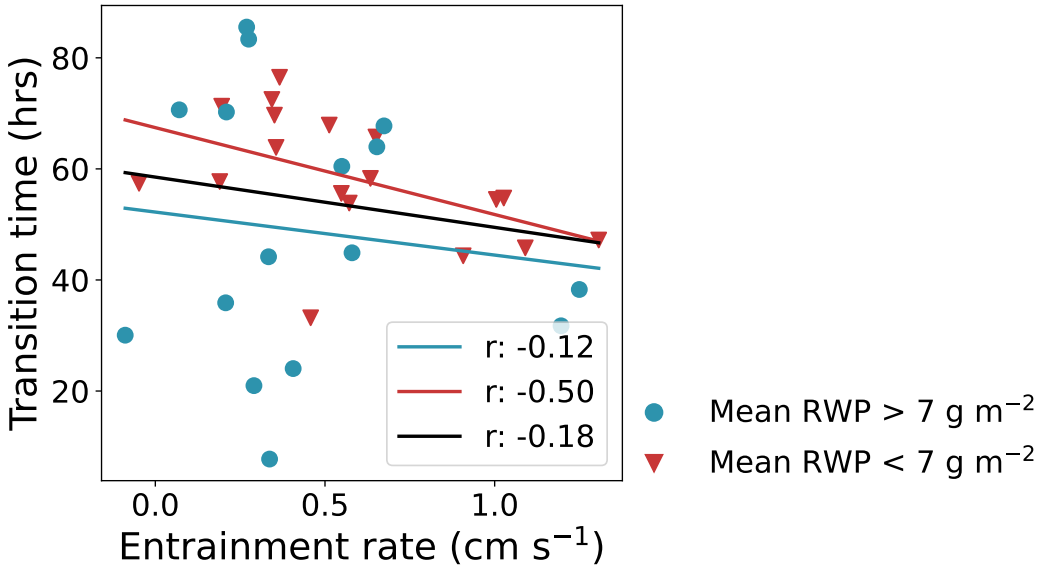

Figure B.8: Entrainment at the start of stratocumulus against transition time for PPE members. The PPE is split by high (blue) and low (red) mean rain water path.

Appendix C

C.1 Nugget effect on averaged response surfaces

The effect of adding a nugget term to the transition time is very small. There are very slight gradient changes for the transition time, but the only discernible difference in Figure C.1 is the reduction of the maximum in panel o, around BL N_a=400, $10^{b_{aut}}$=0.03. A larger nugget term would most likely smooth some of the bumpiness in this panel.

For the rain water path, there is a clear improvement from adding the nugget term. The jump in specific humidity panels in the no nugget term response surface (Figure C.2, panels d, e, f, j, and n) have an undulation in them, which is a result of the emulator interpolating the data exactly. With the nugget term, this undulation is removed to show a surface that is much closer to the model's deterministic behaviour. The nugget term does incur a slight undulation for the autoconversion parameter (panels k-o), so again this nugget could probably be improved upon with a slightly larger value as the surface is still being forced too much by the data (in another part of parameter space).

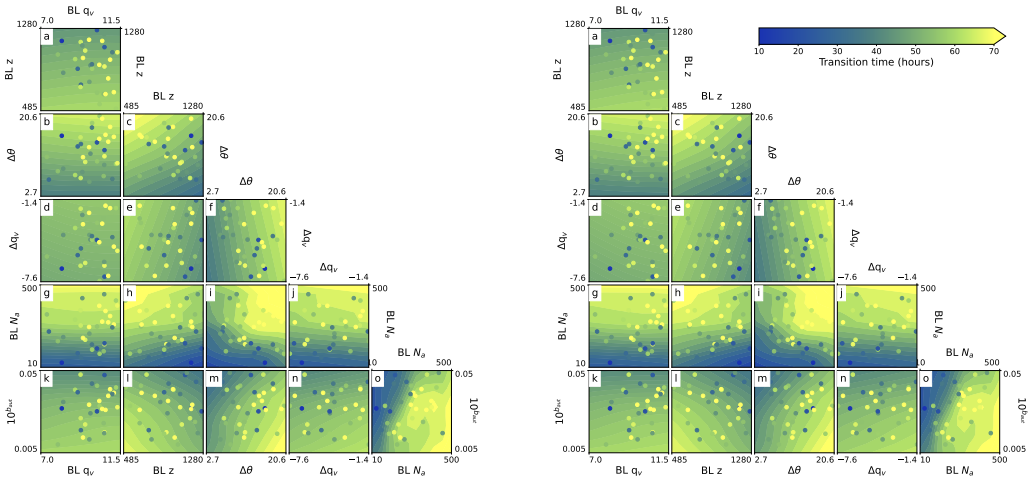

Figure C.1: Transition time response surfaces without a nugget term (left) and with a nugget term (right). a-o) shows each 2-dimensional combination of the six perturbed factors averaged in the four dimensions not shown. Coloured points show the training data distribution and values.

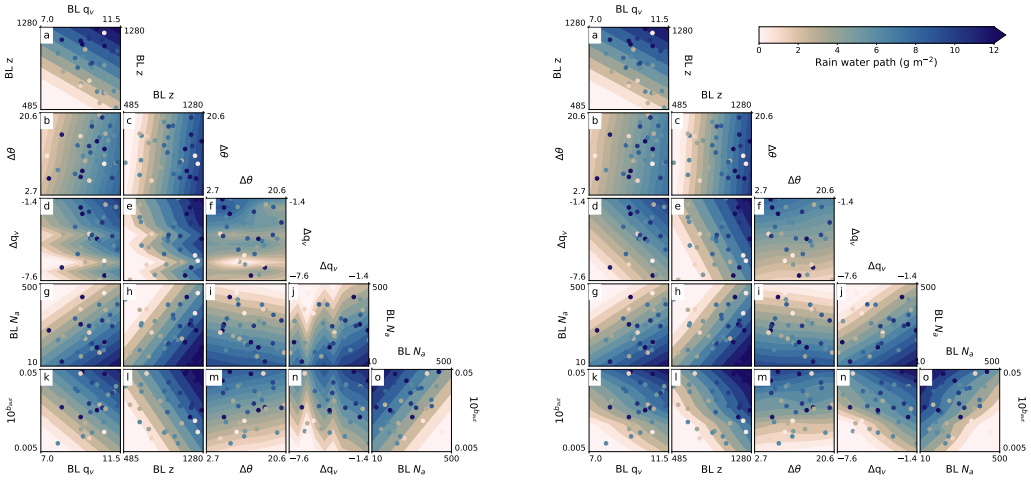

Figure C.2: Average rain water path response surfaces without a nugget term (left) and with a nugget term (right). a-o) shows each 2-dimensional combination of the six perturbed factors averaged in the four dimensions not shown. Coloured points show the training data distribution and values.